SCANNING HALL PROBE MICROSCOPY OF SUPERCURRENTS IN YBCO FILMS

A DISSERTATION
SUBMITTED TO THE DEPARTMENT OF APPLIED PHYSICS
AND THE COMMITTEE ON GRADUATE STUDIES
OF STANFORD UNIVERSITY
IN PARTIAL FULFILLMENT OF THE REQUIREMENTS
FOR THE DEGREE OF
DOCTOR OF PHILOSOPHY

Rafael Baruch Dinner
December 2006

I certify that I have read this dissertation and that, in my opinion, it is fully adequate in scope and quality as a dissertation for the degree of Doctor of Philosophy.

(M. R. Beasley) Principal Adviser

I certify that I have read this dissertation and that, in my opinion, it is fully adequate in scope and quality as a dissertation for the degree of Doctor of Philosophy.

(Kathryn A. Moler)

I certify that I have read this dissertation and that, in my opinion, it is fully adequate in scope and quality as a dissertation for the degree of Doctor of Philosophy.

(Ian R. Fisher)

Approved for the University Committee on Graduate Studies.

Abstract

High-temperature superconductors were discovered 20 years ago, inspiring dreams of levitating trains fed by superconducting power lines. The cuprates, particularly $YBa_2Cu_3O_{7-\delta}$ (YBCO), still promise to fulfill such applications, but must be made to carry higher current density, J_c, which is limited by the rapid onset of dissipation. The dissipation arises from the movement of magnetic vortices in the material, driven by the magnetic field of the current. It is therefore natural to use magnetic imaging to understand these limits on the current.

Initially, I fix a mesoscopic ring of YBCO to a micro-Hall sensor and demonstrate that the sensor is capable of detecting small numbers of vortices. I then proceed with magnetic imaging, constructing a cryogenic scanning Hall probe microscope that combines a 1×4 cm scan range with 200 nm positioning resolution by coupling stepper motors to high-resolution drivers and reducing gears. It enables me to image an entire sample, then zoom in on regions of interest, down to the level of an individual quantized vortex.

Applying this capability to current-carrying YBCO strips, I generate magnetic movies of the materials' periodic response to applied ac currents. From the movies, I reconstruct current density by inverting the Biot-Savart law, and electric field by approximating dB/dt and using Faraday's law. I thereby obtain complete, space- and time-resolved characterizations of the materials, including maps of ac power losses.

After demonstrating this analysis on a single-crystal film, I image two "coated conductors"—YBCO grown on metal tape. I find relatively homogeneous flux penetration in a film grown by pulsed laser deposition (PLD) on an ion

beam assisted deposition (IBAD) substrate, which contrasts with the weak-link behavior of grain boundaries in a film grown by metalorganic deposition (MOD) on rolling assisted biaxially textured substrate (RABiTS). Nonetheless, the in-plane meandering of the MOD film's boundaries allows them to sustain high currents. This observation leads me to image individual boundaries with various in-plane tilts, where I conclude that control of grain boundary orientation offers a route to higher critical current density.

Acknowledgments

Many people contributed directly to this work, and many more to my happiness at Stanford over the last six years. Know that your generosity is not forgotten![*]

Kam Moler has been an excellent guide, taking me under her wing despite my other allegiances. She dreamed up my microscope, and all along identified obstacles it might stumble over, as well as ways around them. She also embodies a conscientious citizen of the lab community; I strive to emulate her.

Mac Beasley lent vision to my efforts, making them coherent in the end (after some editing). I've had access to his deep understanding of superconductivity, electromagnetism, and how experimental physics proceeds in practice. Mac's generosity has characterized our personal interactions. It was also a privilege to encounter, fleetingly, Jo Anne Beasley, and her art.

Janice Guikema laid the experimental foundation for my scanning efforts, and helped me from the beginning, donating Hall probes and experimental advice. Myles Steiner was always happy to take time to share his knowledge of lock-ins, knot-tying, and Yosemite. Eric Hung helped with initial construction of the scanner. Mike Rozler contributed in various ways, many of them positive.

Clifford Hicks donated many Hall probes and grilled meats to the greater good. Yu-Ju Lin also took up the Hall probe fabrication effort. Ophir Auslaender was always ready with answers, most of which proved correct, covering topics from the nanometer scale to the international scale. Hendrik Bluhm lent many an hour to discussing my physics quandaries, from experiment to theory. His dead reckoning was quite accurate. Nick Koshnick was also happy to chew on my problems, all

[*]...except for those I've forgotten.

the while tolerating my political obstinacy.

Matt Feldmann is the source of many of my ideas about coated conductors and how to characterize them. He performed some of the experiments that led to my work, then gave me samples and computer code, complete with training in its use. Similarly, Marty Rupich, Brady Gibbons and, particularly, Vlad Mattias were generous with samples and know-how about the elaborate world of coated conductors. I've also had some good conversations with Paul Barnes and his collaborators. Harold Weinstock and the Air Force Office of Scientific Research were always supportive and, in addition to funding, provided opportunities to meet some of the interesting people above.

Mark Topinka was very insightful, dipping into his broad knowledge of low-temperature condensed matter physics. Per Björnsson, Jenny Hoffman, Brian Gardner, and Eric Straver each helped me out on numerous occasions, whether with samples or their detailed knowledge of scanning probe microscopy. Lan Luan is a fount of enthusiasm; I fully expect nanomagnets to yield up their secrets to her. Erhan Yenmilez was an enjoyable and tolerant apartment mate with a good sense of perspective on the world of science.

Jeong-uk Huh was extremely generous with time and samples. Dave Weld was always willing to lend me a hand, revealing his deep-seated tendency toward niceness. For example, he provided the code on which my `average_cycles.m` routine is based. Yana's (unwarranted) lack of self-confidence was always entertaining. Craig Howald, with some prompting, doled out solid experimental guidance. Alan Fang required less prompting. Paul SanGiorgio made a valiant attempt to build community within the KGB lab. Our memories live on . . . with some Elban punk. Serge Reymond gave me some MoGe and a bird's eye view of life.

Gertjan Koster has been a great resource on the materials science side of things, and a diving buddy. Joseph Sulpizio and Hung-Tao Chou helped me with atomic layer deposition. I inherited my first dipping probe from Leonid Litvak, and a lithography mask from Connie Wang. Ann Erickson kept the PPMS working for everyone. William Jo handed me my first piece of YBCO. Bob Hammond has been helpful all around, since he knows how everything works.

Ted Geballe is clearly the nicest person I've met, lending me his house for my wedding and his encyclopedic knowledge of electronic materials on other occasions. Aharon Kapitulnik scores points for mellowing with age. John Kirtley donated his scanning expertise at various times during my stay in Kam's lab, but especially this quarter, where he, along with Eli Zeldov, Beth Nowadnick and Hovnatan Karapetyan, have started a new experiment with my scanner. I thank all of them for working with its flaws and breathing new life into it. Aaron Streets also extended the instrument, demonstrating its use for scanning potentiometry.

Ian Fisher has been friendly and helpful all along, dutifully enlisting for my committees. I particularly enjoyed his course on magnetism in condensed matter. I thank Bob Sinclair for taking time to chair my defense. I hope I (belatedly) answered his question satisfactorily. David Goldhaber-Gordon has also shown an interest in my work, and shared various tricks of the trade. I've enjoyed corresponding with Christian Jooß, Ernst Helmut Brandt, and John Clem.

I haven't completely forgotten the great group that welcomed me to Stanford, including Jesse Wodin, David Altman, Marco Rolandi, Phil Romenesko, John Paul Strachan, Lindsay Moore, T.J. Bay, Arito Nishimori, Paulina Kuo, Jen Burney, Sam Waldman, Ke Wang, Mike Filler, I-Chant Chiang, Joy Portlock, Helen Fields, Polly Fordyce, and Caolionn O'Connell. Over time, I enjoyed mingling with an equally entertaining cast of characters such as Andrei Garcia, Charis Quay, Ileana Rau, Kathryn Todd, Sylvia Smullin, Andy Geraci, John Chiaverini, Nadya Mason, Wolter Siemons, Jing Xia, Nik Ingle, Jim Reiner, Nancy Ru, Mike Jura, Adam Sciambi, Zhifeng Deng, Nick Breznay, Elizabeth Schemm, Kookrin Char, Alex de Lozanne, Yoshi Maeno, Doug Bonn, Inna Vishik, Andrew Whitehead, James Willet, and Shuichi Kusaba. In addition, the Solomon lab (Marina, Dey, Caleb, Jen...) provided a good second hangout.

Working away in the background to make life easy for me were Mark Gibson, Judy Clark, Cyndi Barnett, Paula Perron, Claire Nicholas, Angela Edwards, Laraine Lietz-Lucas, Kyle Cole, Carol Han, Larry Candido, and Droni Chiu. Early in my Stanford career, Marty Fejer and Ueyn Block provided a glimpse into a beautiful experiment. In the machine shop, Mehmet, Matt, Karlheinz, and

John were immensely helpful and tolerant of my mistakes. Tom Carver made the Ginzton Microfab a great place to work.

Of course, my family, which has broadened to Simin, Arnold, Shira, Jon, Aaron, Dora, Hannah, Joy, Scott, and Shou-Mei, has provided a background of support for all of my endeavors. Finally, my wife, Pin-pin Wei, has made my stay at Stanford beautiful; I look forward to a lifetime of adventure with her.

—Rafael

`rdinner@stanfordalumni.org`

Contents

List of Tables

List of Figures

Chapter 1

Introduction

1.1 Superconductors for power applications

This thesis examines the current-carrying capacity of films of the high-temperature superconductor $YBa_2Cu_3O_{7-\delta}$ (YBCO). High-temperature superconductors (HTS) show great promise for high power applications such as motors, generators, power cables, fault current limiters, energy storage, and magnets [Larbalestier et al., 2001]. These materials operate at higher temperatures than conventional superconductors, but also at higher magnetic fields, H, and current densities, J. In these last two respects, YBCO excels. While its 93 K transition temperature (T_c) is not exceptional—the current record 153 K, held by $(Hg_{0.8}Tl_{0.2})Ba_2Ca_2Cu_3O_{8.33}$ under pressure—it supports the highest current densities over a wide range of temperature and field.

Several other superconductors used for power applications are compared to YBCO in Table 1.1. The second row lists irreversibility field, H^*—the magnetic field above which a superconductor cannot carry current without resistance.* YBCO's H^* rises rapidly with decreasing temperature, and at present cannot be directly measured below 60 K, but an extrapolation to 4 K yields ∼100 T.

*For the low-T_c materials, H^* is almost equal to the upper critical field, H_{c2}, where superconductivity is extinguished altogether. In contrast, for the high-T_c superconductors, H^* is considerably less than H_{c2}, limited instead by the transition to a vortex liquid phase. Nonetheless, H_{c2} in the high-T_c materials is so high (hundreds of Tesla) that H^* remains large.

	low-T_c		high-T_c	
	Nb-Ti	Nb_3Sn	$(Bi,Pb)_2Sr_2Ca_2Cu_3O_\delta$	$YBa_2Cu_3O_{7-\delta}$
T_c (K)	9	18	110	93
H^* (T) @ 4 K	10	24	$\gg 20$	$\gg 20$
J_c (MA/cm^2) @ 4 K, 0 T	1	1	1	50

Table 1.1: Transition temperatures, irreversibility fields, and critical current densities for several materials used in superconducting power applications [Larbalestier et al., 2001; Poole, 2000].

Such a high field immediately suggests that YBCO might yield revolutionary new electromagnets, just as Nb-Ti and then Nb_3Sn have done in the past.

$(Bi,Pb)_2Sr_2Ca_2Cu_3O_\delta$ (Bi-2223) offers a lower, but still immeasurably high, H^* at low temperatures. However, it cannot carry high J, as indicated by the last row of Table 1.1. All superconductors exhibit a critical current density, J_c, above which dissipative processes quickly arise, as portrayed by the E–J curve in Figure 1.1 and elaborated on below. J_c is defined as the current density, J, at which the electric field reaches a chosen criterion, E_c, typically 1 μV/cm. J_c drops with increasing H until it falls to zero at H^*.

Bi-2223 adds the complication of anisotropy—H^* and J_c drop by a factor of 100 as H is rotated from parallel to perpendicular to the material's copper-oxygen planes [Larbalestier et al., 2001]. This severely limits applications of Bi-2223, particularly in magnetic fields. With lower anisotropy ($\sim$6), YBCO films can realize an exceptionally high J_c, making them the best candidate for the next generation of superconducting wire.

As a brittle, crystalline material, however, YBCO is not easily drawn into wires like Nb-Ti. Instead, a "coated conductor" architecture has been developed,

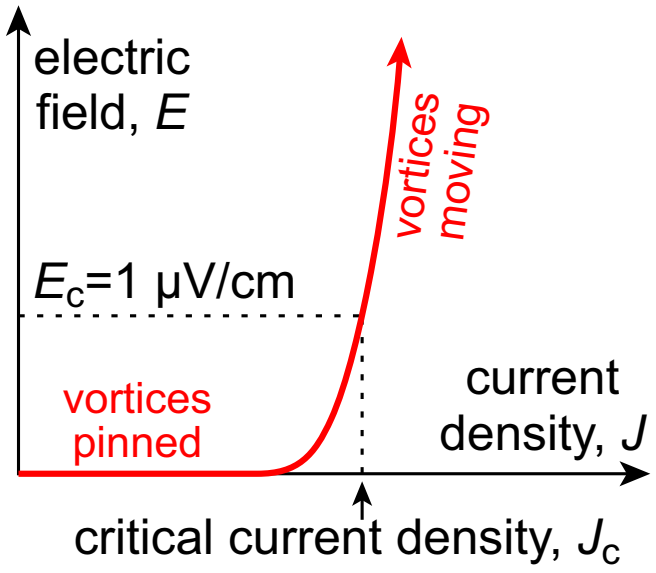

Figure 1.1: Superconductors exhibit a critical current density, J_c, above which the flow of vortices dissipates energy and generates an electric field.

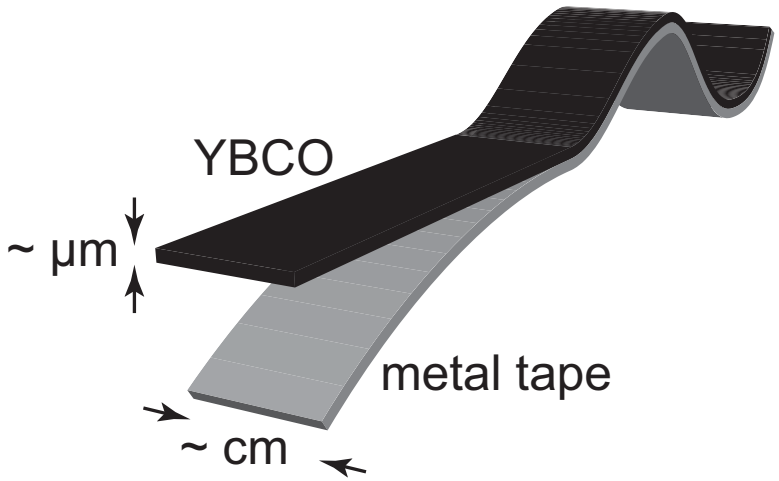

Figure 1.2: Illustration of a coated conductor, in which a YBCO film is coated on a metal tape that provides mechanical stability.

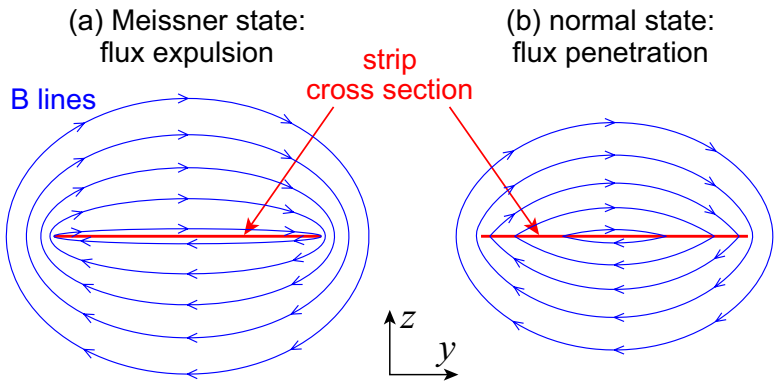

Figure 1.3: Magnetic field lines, in blue, wrap around a superconducting strip that carries current. (a) The strip exhibits the Meissner effect, expelling magnetic flux. (b) As the current and magnetic field increase, flux is forced into the strip, destroying superconductivity. The field lines shown are for the uniform current present for full flux penetration ($I = I_c$).

as illustrated in Figure 1.2, in which a YBCO film is coated on a metal tape that provides mechanical stability [Larbalestier et al., 2001]. After developing techniques to characterize superconducting films in Chapters 4–7, I examine current flow through two coated conductor samples in Chapter 8.

1.2 Magnetic characterization of critical current

J_c is traditionally determined by macroscopic "transport" measurements of current and voltage on a sample of known dimensions, yielding an E–J curve as in Figure 1.1. Magnetic measurements provide another, and in some ways complementary, means of measuring J_c. Resistanceless flow arises from the phase stiffness of the superconducting order parameter; this phase stiffness is destroyed by movement of magnetic flux through the material.

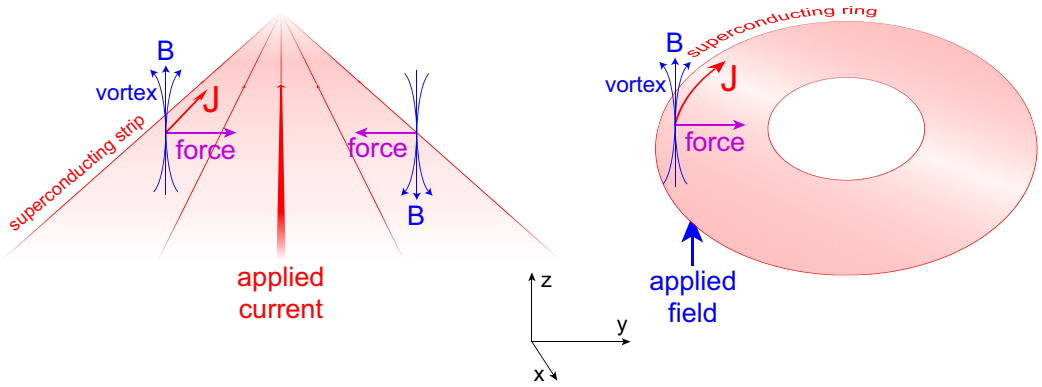

Figure 1.4: The critical current of high-T_c superconductors is limited by the movement of magnetic vortices. This movement can be studied by applying a current to a superconducting strip, or a field to a superconducting ring.

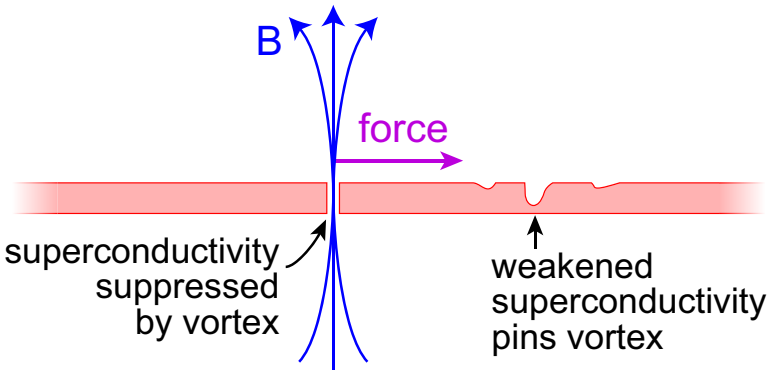

Figure 1.5: Vortices must suppress superconductivity, which costs energy, thus points of weakened superconductivity form energy minima that pin vortices in place.

Figure 1.3 depicts this process for a strip. The current generates a magnetic field that is expelled by the superconductor (the Meissner effect). However, such expulsion costs free energy, and at sufficiently high current the superconductor lowers its energy by admitting flux in the form of vortices, as illustrated in Figure 1.4(a). Each vortex admits one quantum of magnetic flux, $\Phi_0 = h/2e = 2.07 \cdot 10^{-15}$ Wb. Vortices suppress superconductivity over a small core region (the size of the coherence length, $\xi \approx 2$ nm for YBCO), which costs some energy, but reduces the system's magnetic energy.

In accordance with the direction of the magnetic field lines, vortices of opposite sign form at the edges of the strip. They interact with the current density, $\vec{J}$, each vortex feeling a Lorentz force per length of the vortex [Tinkham, 1996b],

$$\vec{F} = \vec{J} \times (\Phi_0 \hat{z}), \tag{1.1}$$

This force pushes them toward the center where they annihilate, dissipating energy as they move. Because vortices must suppress superconductivity, points of weakened superconductivity, such as defects, form energy minima that pin vortices in place. However, some current density, J_c, will be sufficient to depin them. J_c is therefore proportional to the pinning force, F_p. With magnetic imaging, I can watch vortices depin, and reconstruct the current that depinned them.

My initial experiment, however, is greatly simplified compared to magnetic microscopy. As described in Chapter 3, I fix a YBCO ring to a magnetic sensor in order to measure its magnetization as a function of applied field and temperature. From changes in this magnetization I infer the movement of vortices and the current flowing around the ring. The ring and sensor's micron-scale sizes make the experiment sensitive to the movement of even a few vortices. Without spatial resolution, however, the details of vortex movement remain ambiguous.

In Chapter 4, I resolve this ambiguity by constructing a scanning Hall probe microscope to image vortex movement directly. Single vortex images in Chapter 5 provide a test of the instrument's resolution. I then apply the microscope to imaging YBCO strips carrying current.

Chapter 6 examines a strip of YBCO on a single-crystal $LaAlO_3$ substrate that exhibits homogeneous vortex penetration, reflecting a homogeneous pinning force, adequately described by the critical state model [Bean, 1964]. Chapter 7 introduces another "single-crystal" film, but the magnetic images suggest inhomogeneous vortex pinning. Because the data does not conform to any simple analytic model, I turn to numerical transformations to extract quantitative information.

The film's two-dimensional geometry allows me to transform its magnetic image into the underlying current distribution, inverting the Biot-Savart law. Furthermore, by taking time series of images and approximating dB/dt, I can reconstruct the electric field using Faraday's law. I thereby demonstrate that time-resolved magnetic imaging, accessible via scanning Hall probe microscopy, offers a complete, time- and space-resolved electromagnetic characterization of superconducting thin films.

Finally, in Chapter 8, I bring these tools to bear on modern samples of YBCO wire consisting of YBCO grown on metal tape—coated conductors. In these polycrystalline materials, grain boundaries play an important role, which I investigate further with several model samples, fabricated on bicrystal substrates. I conclude that the current-limiting effects of grain boundaries can be mitigated, and offer hope that properly controlled grain boundaries can be used to enhance flux pinning.

Chapter 2

Micro-Hall sensors

2.1 Introduction

Almost all of the experiments described in this thesis rely on micro-Hall sensors for the measurement of magnetic induction. The fabrication of these sensors takes advantage of the technological infrastructure built by the semiconductor industry, using molecular beam epitaxy (MBE) to grow nearly perfect crystals, and electron beam lithography to pattern them into useful structures. The result is a useful combination of submicron spatial resolution and milligauss field resolution over a wide temperature range, as described below.

I inherited the sensors used for these experiments from other students' microfabrication efforts, as specified in Section 2.3. However, Hendrik Bluhm and I did contribute to the fabrication of a succeeding generation of sensors ultimately completed by Clifford Hicks [Hicks et al., 2006].

2.2 Design

The magnetic sensors used exploit the Hall effect, illustrated in Figure 2.1(a). Applying current between two opposing leads of a conducting cross and measuring voltage across the other pair of opposing leads yields a Hall resistance that is

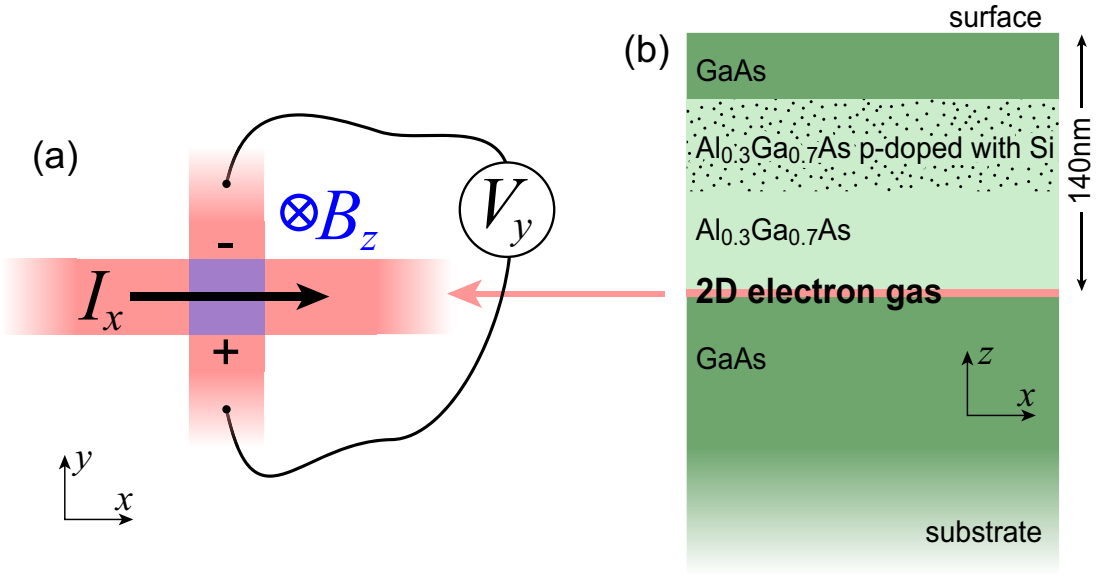

Figure 2.1: (a) An illustration of a Hall cross. Pink and purple areas are conducting 2DEG; white areas are etched barriers. The cross generates a transverse voltage proportional, ideally, to the perpendicular component of magnetic field, B_z, averaged over the cross intersection, i.e. sensitive area (the purple area). (b) The vertical structure of the two-dimensional electron gas (2DEG) wafer from which the Hall cross is etched.

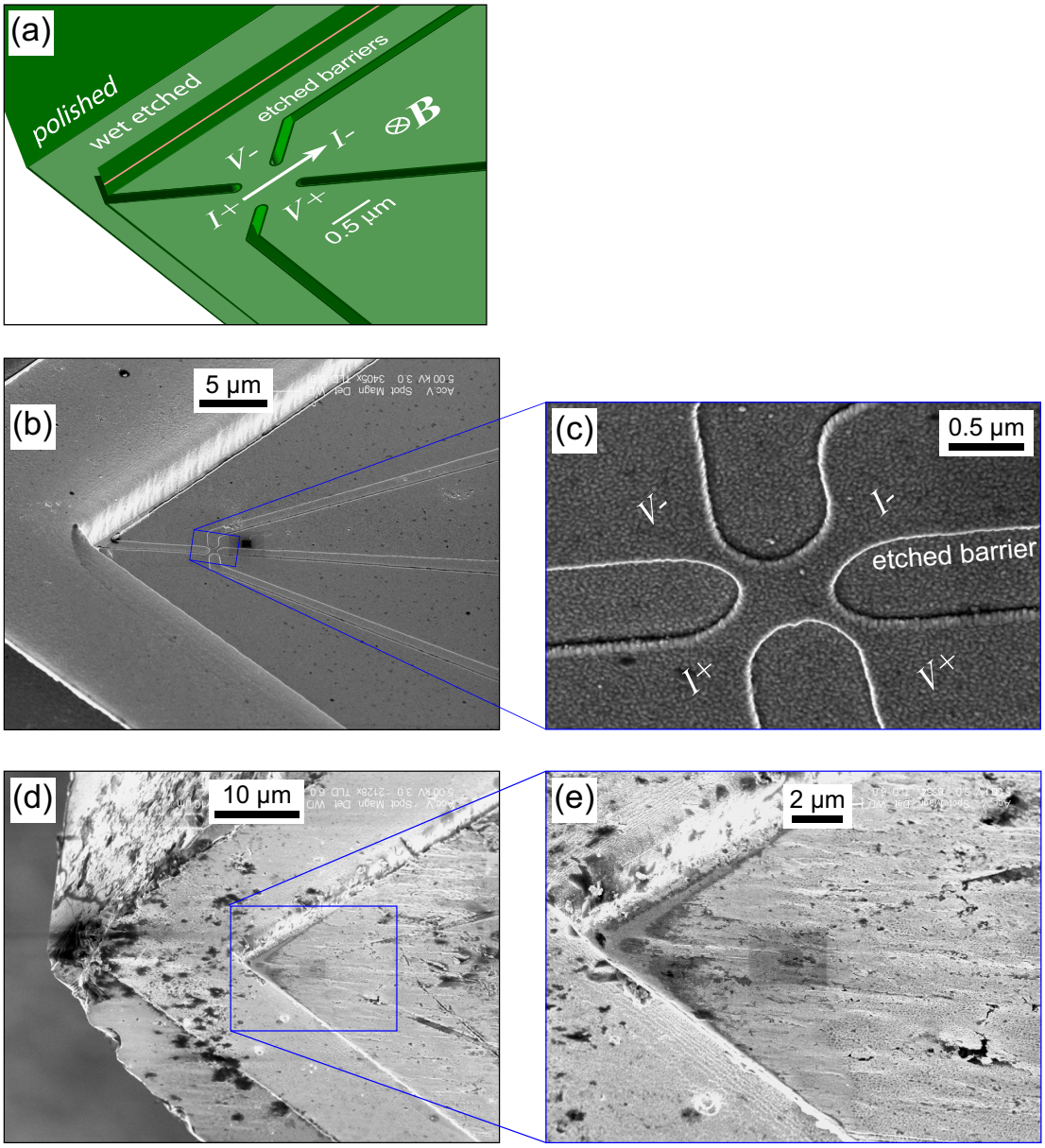

Figure 2.2: (a) An illustration looking upward at a scanning Hall sensor. A Hall cross is fabricated close to a microfabricated corner that is brought into contact with the sample. Material outside the corner is manually polished away. (b) Scanning electron micrograph (SEM) of the corner of sensor 28. (c) Zooming in on the sensitive area. (d) SEM of sensor 45 after many scans (several linear meters of scanning). (e) Zooming in. The dark rectangular patches in (b), (d), and (e) arise from other SEM scans. SEMs taken by Ophir Auslaender.

proportional to the component of magnetic field perpendicular to the leads, averaged over the "sensitive area"—the intersection of the leads [Geim et al., 1997]. This transverse resistance measurement can be performed with dc or ac current and various data acquisition methods, which are specified in each experiment's Chapter.

2.3 Fabrication

The sensors are fabricated from a high-mobility two-dimensional electron gas (2DEG) in a GaAs-$Al_{0.3}Ga_{0.7}As$ heterostructure with low carrier density for a large Hall resistance. The layers of the material are shown in Figure 2.1(b). Each sensor's Hall cross is patterned with electron-beam lithography and ion milling through the 2DEG donor layer, creating four trenches to separate four leads [Guikema, 2004]. A corner that serves as a tip for scanning is etched near the Hall cross, shown in Figure 2.2(a). When scanning, I tilt the sensor to ensure that this corner stays in contact with the sample surface. I manually polish away material outside the corner that might interfere with the corner touching the sample.

The sensor used in Chapter 3 (described in Section 3.3) was fabricated by Yu-Ju Lin. All of the other sensors were from Janice Guikema's "2001 b" batch using a 2DEG wafer grown by David Kisker at IBM, and will be referred to by Janice's numbering within that set. Sensor 26 is used in Chapter 5, sensor 45 in Chapter 6, and sensor 28 in Chapters 7–8. They are nominally identical, with each one's sensitive area lithographically defined to be a square 500 nm on each side. A metal gate (90 nm of gold on 10 nm of titanium) is deposited over the entire tip, extending back 260 μm. This gate is grounded to screen the sensor from electric fields. For sensor 53, used in Chapter 9, the sensitive area is 700 nm on each side, and there is no gate.

In addition, sensor 28 (Chapters 7–8) is coated with an insulating layer to isolate the gate from sample voltages: 50 nm of Al_2O_3 is grown via atomic layer deposition using a Cambridge NanoTech Inc. Savannah 200. The growth occurred

by depositing trimethylaluminum, oxidizing it with water, and iterating 500 times. The oxide is also intended to provide protection against mechanical wear.

Figure 2.2(d)–(e) show direct evidence of this mechanical wear for sensor 45, which was not oxide coated. Note that these images were taken well after the data in Chapter 6. The corner that contacts the sample shows a region that appears to be polished smooth, and the barriers between leads appear less prominent, either worn away or filled in. There are also scratches along the scanning direction (the direction in which the tip points).

However, even without the oxide, mechanical wear was gradual, with sensors lasting for meters of linear scan movement (i.e. the sum of the lengths of scan lines) before showing electrical changes, typically increased two-point resistance accompanied by decreased Hall response (see Section 2.5.1).

2.4 High-field magnetic response

For all sensors, I verified that the Hall resistance is a linear function of applied magnetic field for fields up to 0.5 T. Above about 1 T, the Hall voltage oscillates as a function of field, as seen in Figure 2.3. Several different probes show coincident dips. The 50 μm probe was measured by Mike Rozler in his Janis cryostat. All others were measured by me in LAM's shared PPMS (Quantum Design Physical Properties Measurement System).

These probes differ in lithographic dimensions, with sensitive areas ranging from 50 μm to 0.5 μm. They are, however, all fabricated from the same 2DEG wafer, grown by David Kisker at IBM, giving them the same carrier density and therefore the same applied field locations for quantum Hall plateaus. Furthermore, the oscillations are prominent at 4.2 K, but wiped out at 77 K, consistent with quantum Hall. Note that one would not expect the resistance to adhere strictly to the quantum Hall prediction, made for the low voltage limit. For these measurements, the voltage across the sensor ($\sim$70 mV at the applied current of 10 μA), will excite many modes of transport.

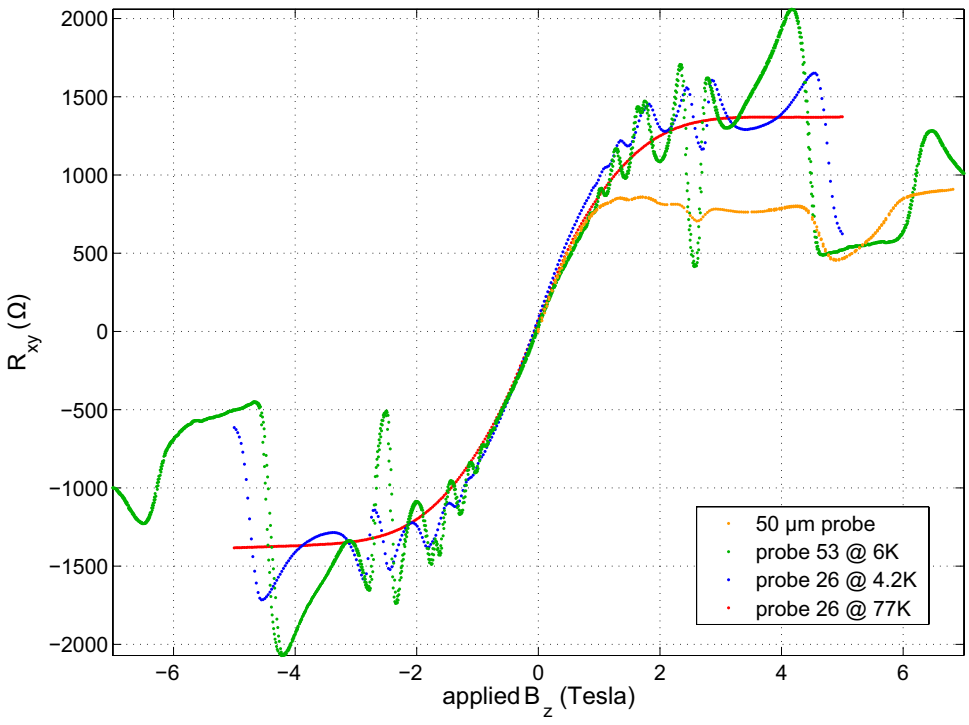

Figure 2.3: The Hall (transverse) voltage of several sensors as a function of applied field with a 10 μA applied current. The response is approximately linear for field magnitudes below 0.5 T. Above that, oscillations appear that probably arise from the quantum Hall effect. The 50 μm probe was measured by Mike Rozler in his Janis cryostat. All others were measured by me in the LAM PPMS (Quantum Design Physical Properties Measurement System).

2.5 Low-field magnetic sensitivity

2.5.1 Hall coefficient

For the sensors used in Chapters 4–9, I calibrated, as a function of temperature from 2.5 to 320 K, the linear slope (Hall coefficient) and offset relating transverse resistance to applied field around zero field. One such calibration is shown in Figure 2.4. The Hall coefficient is about 0.1 Ω/G below 100 K, and ∼ 10 times smaller at room temperature.

Even controlling for factors like temperature, the Hall coefficient of a sensor could change over time. For example, after many scans, sensor 53 was recalibrated and showed 10 times lower Hall coefficient. The two-point resistances had also changed (from ∼10 kΩ to ∼20 kΩ). A probable cause is the gradual mechanical wear of scanning, described in Section 2.3. sensor 45 likely suffered similar changes, though this was not verified through recalibration.

As described in Chapter 9, fits to the images taken with sensor 53 suggest a lower Hall coefficient than the calibrated value, which leads me to abandon the calibrated value in favor of the fitted values. Thus calibrated Hall coefficients, used in Chapters 3, 5, 6, and 8, may be inaccurate, typically higher than the real Hall coefficients.

2.5.2 Noise

The field resolution of these probes is limited by noise from several sources. Figure 2.5 shows a zero-field power spectrum of the transverse (Hall) voltage of sensor 26 with various dc currents applied to the Hall cross. These measurements were taken in the scanning Hall probe system described in Chapter 4. The voltage is amplified (by a Stanford Research Systems SR560), then digitized and Fourier transformed (by a Stanford Research Systems SR760), then divided by the amplification. At zero current (the blue spectrum), the sensor should be at thermal equilibrium, exhibiting only Johnson noise (whose level is indicated in by the black line). The additional noise must arise from other parts of the system, such as the

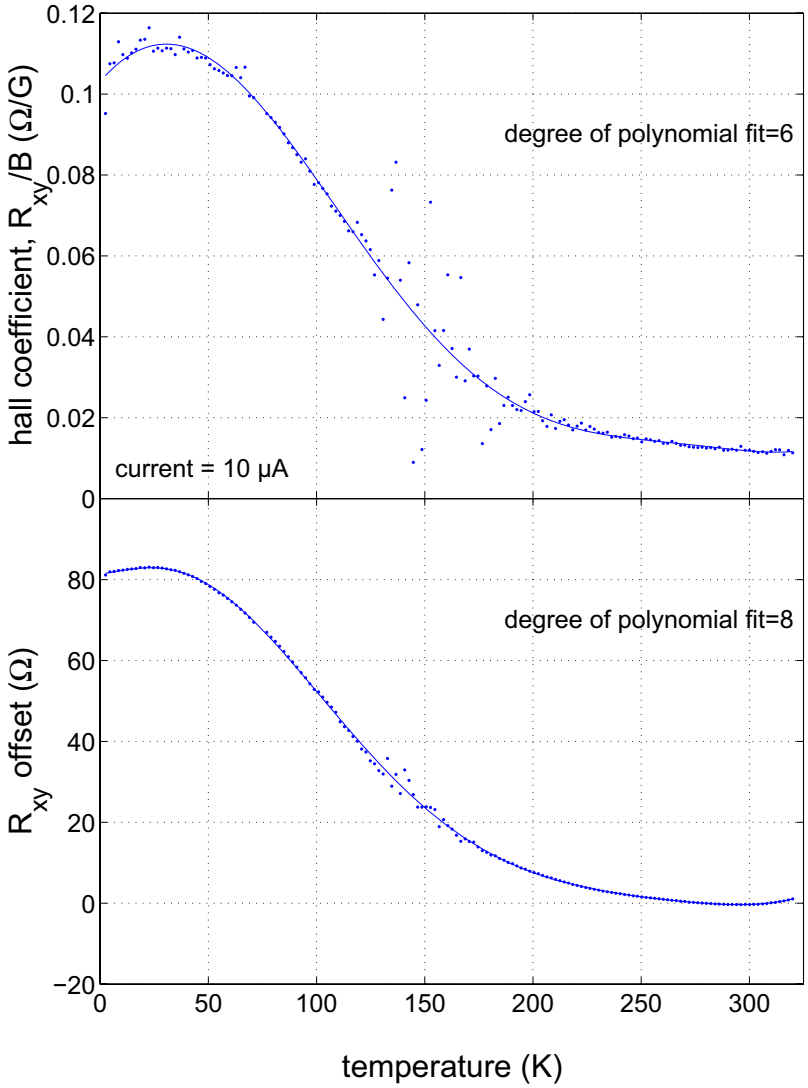

Figure 2.4: Measurements of the transverse resistance of Hall sensor 26 around zero applied field. The slope and intercept of the linear response yield the Hall coefficient and offset resistance, respectively. The points are measured; the solid curves are polynomial fits that serve as calibrations for succeeding measurements.

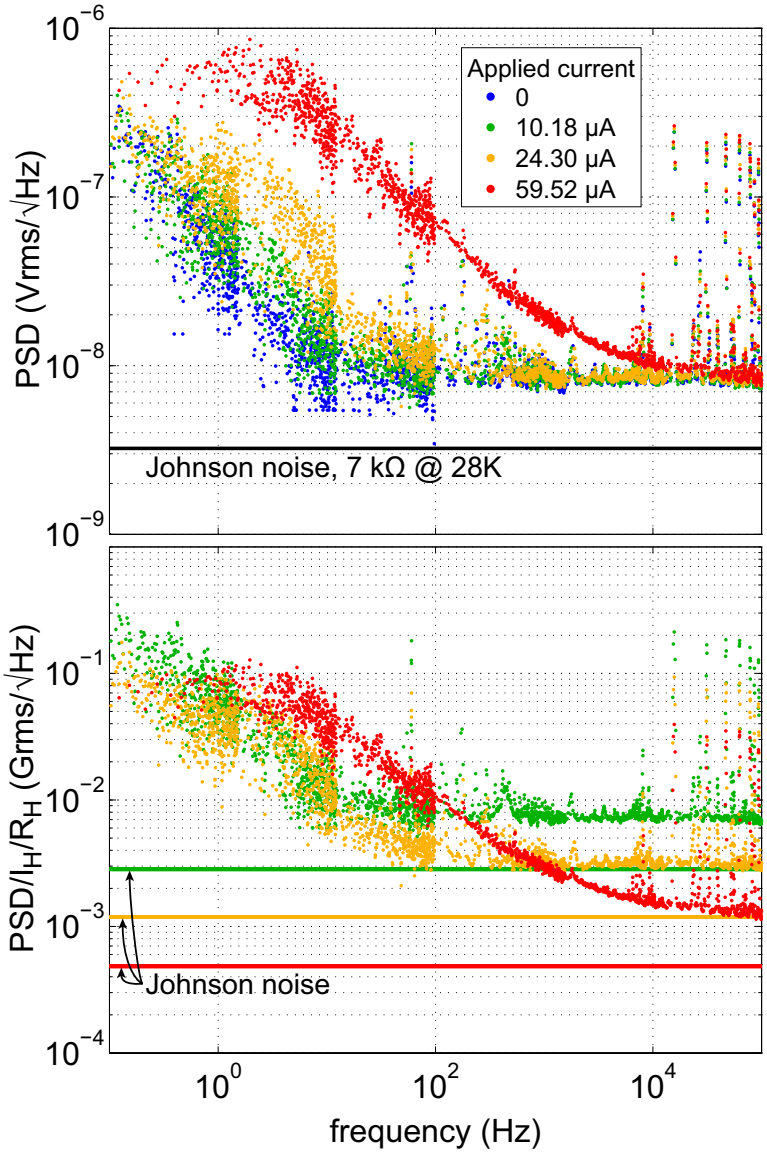

Figure 2.5: Noise spectrum (power spectral density) of Hall sensor 26 at 28 K with no applied field and various dc applied currents. In (a), the transverse voltage is amplified (by a Stanford Research Systems SR560), then digitized and Fourier transformed (by a Stanford Research Systems SR760), then divided by the amplification. Measurements from several frequency ranges are concatenated to form each spectrum, accounting for their segmented appearance. In (b), the voltage spectrum is calibrated (by dividing by the Hall current, I_{H}, and the Hall coefficient, R_{H}) and plotted as magnetic field noise.

amplifier. This additional noise exhibits both white and $1/f$-like components.

The $1/f$ noise grows with applied current, now presumably arising from the sensor. Switching processes at a range of frequencies can combine to yield a $1/f$ spectrum, and indeed two-level switching is evident in some voltage time traces (not shown), translating into B noise of up to 5 G. The zero field offset can vary even more between cooldowns, so when it is necessary to measure a dc field (as in Chapters 5–6), the offset is taken as a free, rather than calibrated, parameter.

The $1/f$ noise in the offset intersects the white noise floor near 100 Hz, thus it can be avoided by measuring only fast changes in B, e.g. those produced by a 400 Hz ac sample current, as in Chapters 7–9. In the ac configuration at 400 Hz, with the sensor at 28 K, the measured field noise is 4×10^{-3} G/$\sqrt{\text{Hz}}$, due to comparable contributions from sensor Johnson noise and amplifier noise.

Chapter 3

Flux entry into a YBCO ring

3.1 Introduction

This experiment consists of measuring the magnetization of a micron-scale ring of the superconductor YBCO. As depicted in Figure 1.4, the ring generates a shielding current in response to an applied magnetic field. This current then acts to push vortices into the ring just as an applied current pushes vortices across a strip. By matching the size of the ring to a Hall sensor with sub-flux quantum flux sensitivity, though, I detect movements of individual vortices that would not generate sufficient voltage to be seen in the equivalent transport measurement of a strip.

3.2 Ring fabrication

An array of YBCO rings is fabricated by photolithographic patterning and wet etching of a YBCO film. The YBCO was grown by Luke Peng at Superconductor Technologies, Inc. using pulsed laser deposition (PLD). The full architecture consists of a 300 nm YBCO layer on top of a 30 nm CeO_2 buffer layer on a 400 μm thick "single-crystal" LAO substrate. The substrate does have twin boundaries, but (nominally) no grain boundaries. Another piece of the same film superconducts below 88 K (as determined by the maximum slope in resistance versus

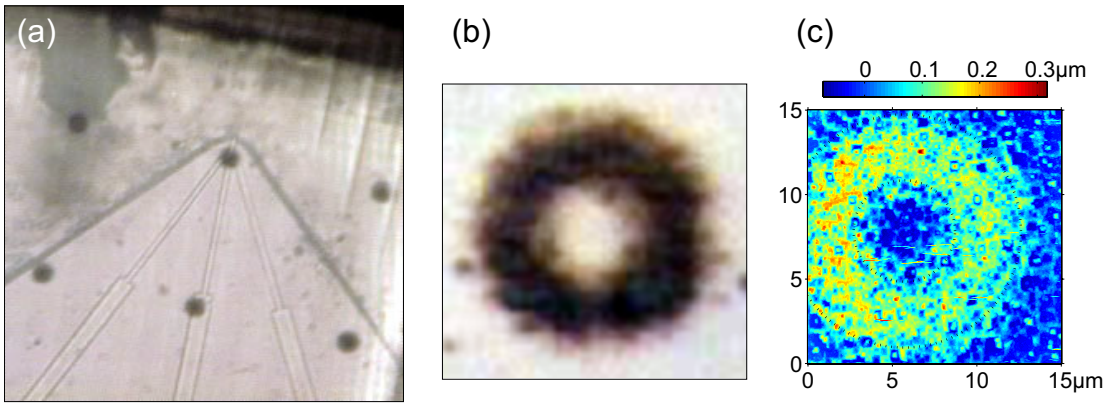

Figure 3.1: (a) Optical micrograph of the array of rings placed on the Hall sensor with one ring aligned to the sensitive area. The rings and sensor are visible through the rings' transparent substrate. (b) Optical micrograph by Janice Guikema of a single ring with the same nominal dimensions as the ring studied. (c) AFM (topographic) image of the ring studied.

temperature, with a transition width of 1 K).

Shipley 1813 positive photoresist is spun on the film, exposed, and developed to leave rings of resist protecting the YBCO underneath. The film is then submerged in citric acid through which nitrogen is bubbled (to reduce the activity of the water, which can degrade the YBCO). This procedure was inherited from Doug Bonn.

After 1.5 minutes, the transparency of the black YBCO increases rapidly, leaving islands of YBCO visible under an optical microscope. The sample is resubmerged to bring the total etching time to 2.1 minutes, after which no YBCO is visible outside of the resist rings. Finally, the resist is dissolved in acetone, and the sample is rinsed with methanol and isopropanol which is blown off with nitrogen.

The change in magnetic field associated with a change in flux is inversely proportional to ring area, thus it is desirable to reduce the ring size to that of the Hall probe's sensitive area, $\approx 1.5 \times 1.5$ μm. However, this size is at the lower limit of what can be fabricated reliably with this method, so I patterned a range of

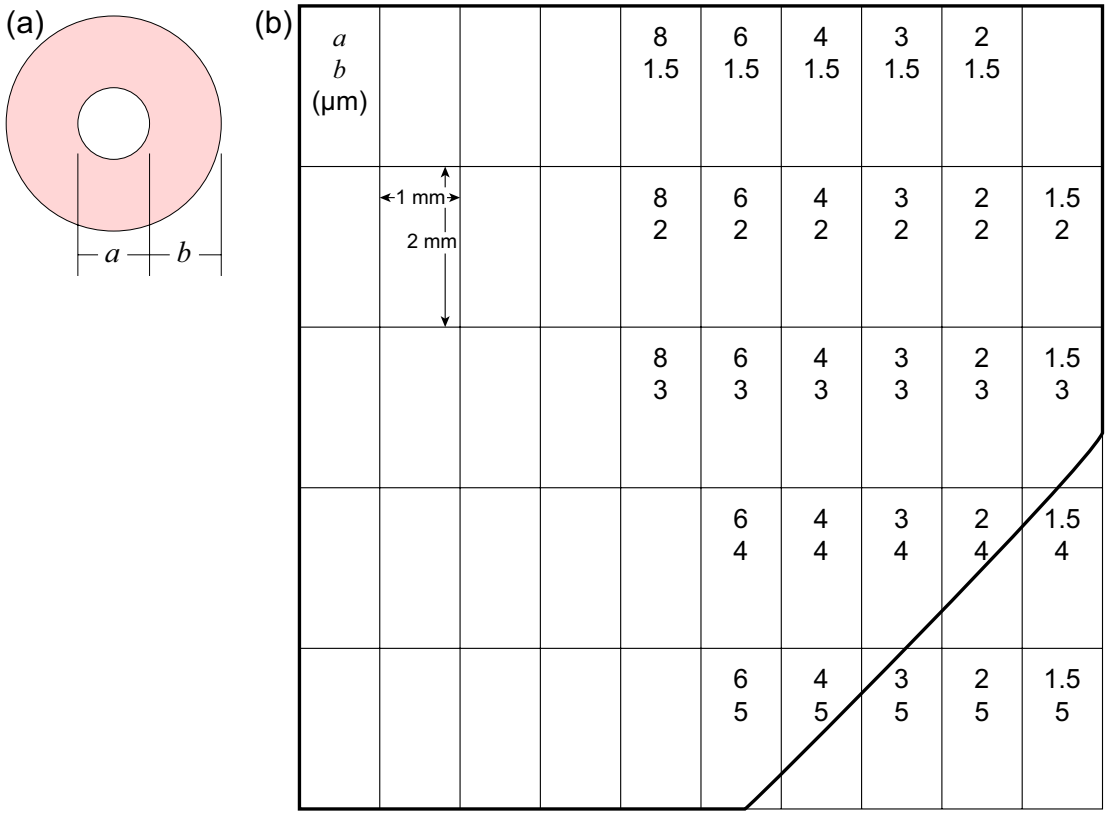

Figure 3.2: (a) The ring sizes are defined in terms of the inner diameter, a, and thickness, b. (b) Nominal ring sizes (in μm) within sections of the photolithographic mask. The outline of the patterned sample is superposed in bold.

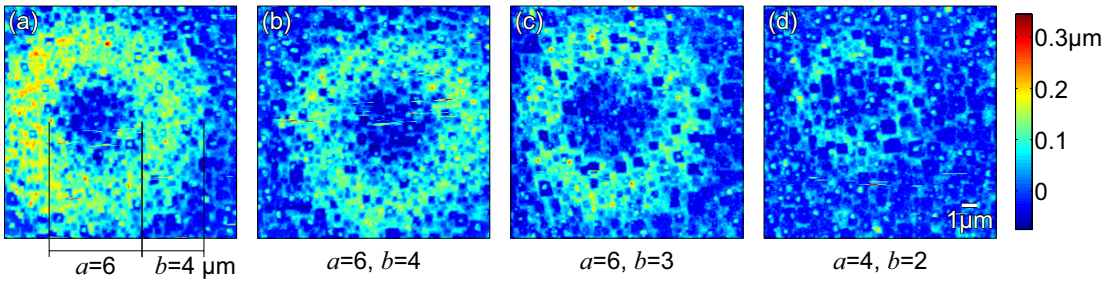

Figure 3.3: AFM (topographic) images of (a) the ring studied and (b–d) other rings with various nominal inner diameters, a, and thicknesses, b, as shown. For each image, a plane fit to the areas outside the ring is subtracted.

larger sizes, shown in Figure 3.2. The 10×10 mm pattern is divided into 1×2 mm areas, each containing rings with a different combination of inner diameter, a, and thickness, b. The rings in each area are spaced by $10 \cdot (a + b)$.

Two factors prevent use of the smaller rings. The portion of the mask with rings of the smallest dimensions, $a = b = 1.5$ μm, is blank, suggesting an error in the mask writing. More importantly in the end, the smaller rings were damaged by the etch. Figure 3.3 shows the topography of several rings after processing.

The tops of all of the rings show pits, many of which are square-shaped, suggestive of directional etching relating to the approximately four-fold symmetry of the crystal domains. Examination of the rings after partial etching (1.5 minutes) indicated that the resist was not significantly degraded by the etch. Rather than etching through the resist, the acid most likely etched horizontally at least 2 μm—six times farther than the 300 nm film thickness—to entirely undercut the 4 μm wide resist of the ring in Figure 3.3(a). The areas outside the rings also show structured topography with remnants of square pits, suggesting that the exposed YBCO is not completely removed even though the resist is already so undercut. To remedy this undercutting in later experiments, I use ion milling ("dry etching") in place of acid ("wet etching"), described in Chapter 6.

Soldiering on, however, I chose to measure the ring shown in Figure 3.3(a),

which was the most intact after lithography. Individual rings are identifiable optically by their position in the ring array, and the same ring shown in Figure 3.3(a) is aligned to the sensor.

3.3 Hall sensor details

General properties of the Hall sensors are described in Chapter 2. I initially use several 2 μm sensors from Janice Guikema's 1998 batch. However, the sensor in Section 3.9, which yields the most important measurements, was fabricated by Yu-Ju Lin with a sensitive area that is nominally a square, 2.5 μm on a side. It is excited with an ac current at various frequencies around 1 kHz, and the in-phase component of transverse voltage is measured with a lock-in amplifier (a PAR 124 with a PAR 116 preamp). The phase is adjusted by zeroing the response to an ac ($\sim$10 Hz) applied field at 90 degrees.

3.4 Sensor-sample alignment

The geometry is depicted in Figure 3.4. First the Hall sensor (see Chapter 2 for details), with its sensitive area facing up, is varnished to a chip carrier, which provides electrical connections for the four sensor leads and thermal contact to the cold finger. I apply a small dab of heatsink paste (zinc oxide in polydimethylsiloxane) to the sensor and place the ring substrate on top of it, with the rings facing down. The ring substrate is transparent, allowing me to see both the rings and the Hall sensor structure by looking down through the substrate with the optical microscope of a probe station, as shown in Figure 3.1(a). I can then push the ring array with the probe station's micromanipulators in order to align the desired ring to the Hall cross.

The heat sink compound is sufficiently fluid to allow the substrate to slide when pushed, but otherwise holds it in place (and freezes at low temperature): The ring did not move visibly between micrographs taken before and after placing the sample chip in the dipping probe and cooling it down.

3.5 Temperature and field control

As shown in Figure 3.4, the sensor-sample assembly is mounted inside a vacuum can on a dipping probe which is inserted into a dewar of liquid nitrogen. The sample cools radiatively to the bath temperature of 77 K. A calibrated platinum RTD thermistor heatsunk to the copper sample block allows temperature measurement and control via feedback to a resistive heater.

A vertical magnetic field is applied with a hand-wound solenoid whose resistance and inductance at 77 K are 48 Ω and 0.24 H. From its geometry and number of turns of wire (3609), I calculate that it produces 0.47 Oe/mA at its center. I assume the turns are distributed uniformly through the measured cross section.

The first sensor's Hall coefficient is then calibrated in situ by applying known dc fields with this solenoid. The results for several temperatures are plotted in Figure 3.5. All the ingredients are now in place to measure the magnetic response of the ring as a function of applied field and temperature.

3.6 The search for the ring

Upon cooling down the ring I found. . .nothing. Flux decay versus time (see Section 3.8) appeared consistent with a bare Hall sensor, as did susceptibility versus temperature (see Section 3.7.

I backtracked, replacing the ring with an unetched piece of the same film of YBCO. The piece was a square 5 mm on a side with its center placed against the Hall sensor. This setup yielded a superconducting transition in susceptibility (χ) versus temperature (T) at 83.9 K (the temperature of the extremum in $d\chi/dT$). The measured response to a 10 Oe rms applied field dropped 95% over 1 K. So the film from which the rings are etched superconducts, albeit at a slightly lower temperature than the optimal YBCO T_c of 93 K.

Two differences between the ring and the square could explain the different results. The ring could have been damaged during patterning and etching of the film such that the ring does not superconduct, even though the unetched

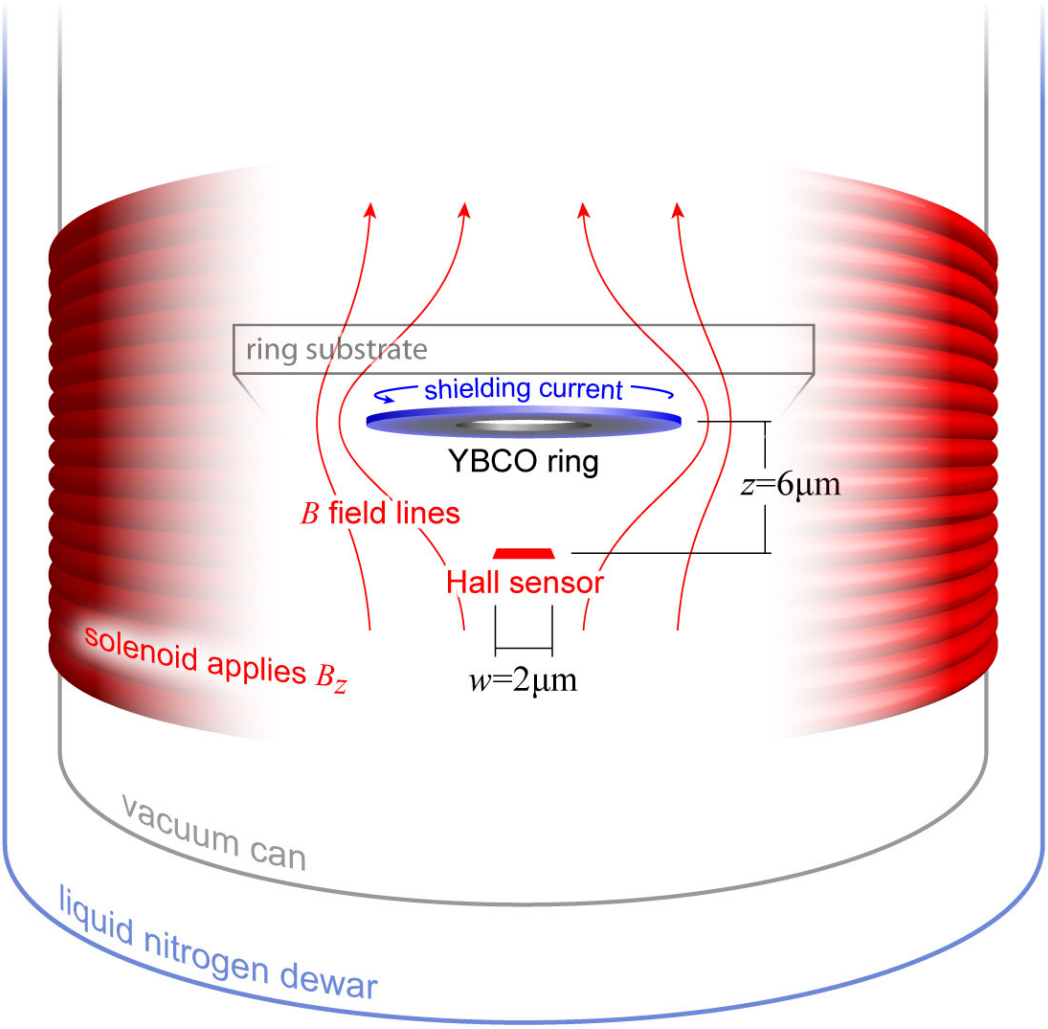

Figure 3.4: Sketch of the apparatus for measuring the magnetization of a mesoscopic ring of YBCO. The ring and the sensor's sensitive area are micron-sized, as labeled, and drawn approximately to scale. The vacuum can is 1 inch in outer diameter, and the dewar is 1 meter in outer diameter.

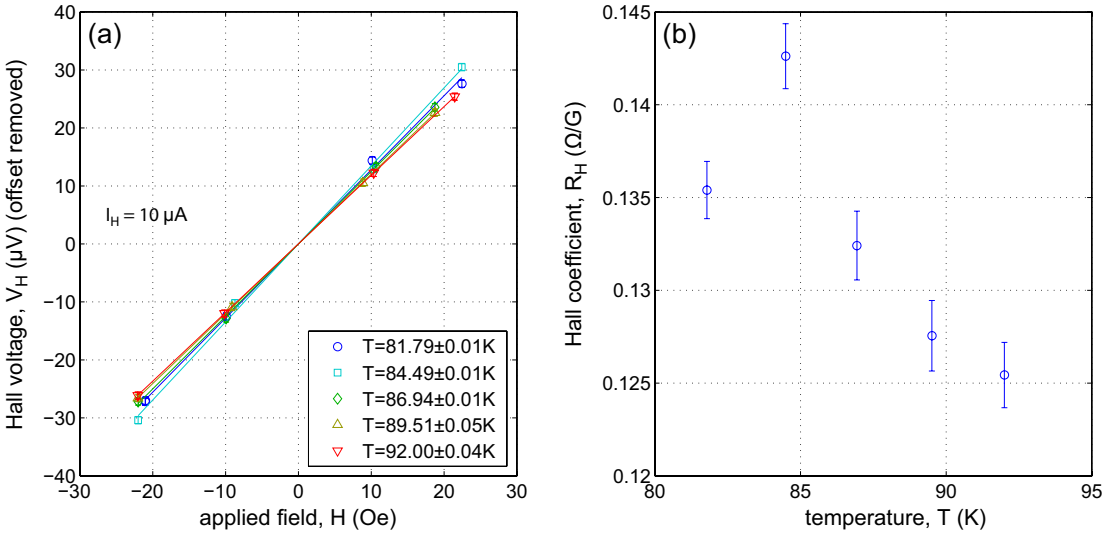

Figure 3.5: (a) Using the solenoid (with calculated field strength), I calibrate the Hall sensor response in the absence of the ring. (b) The slopes in (a) are plotted as Hall coefficients again temperature.

film does. Even if the ring superconducts, though, because of its smaller size, it requires much better alignment (either in the plane or vertically) to the sensor to preserve its diamagnetic signal, while the square could be separated from the sensor by millimeters before its signal dies off.

3.6.1 Imaging the ring

To test the first possibility, that the ring does not superconduct, I enlisted the help of Janice Guikema, who imaged another ring in the same section of the substrate with a scanning Hall probe microscope (the Moler lab SXM). She measured $B_z(x, y)$ by applying an ac current to the Hall sensor and locking in on the in-phase component of Hall voltage. After cooling to 68 K in zero field, she took three scans of the ring, Figure 3.7(a)–(c), at different dc applied fields.

The ring's presence is evident in the images, but it does not appear as a simple Meissner response, i.e. no response for zero applied field and shielding over the entire ring area for finite applied field. Subtracting the zero-field features

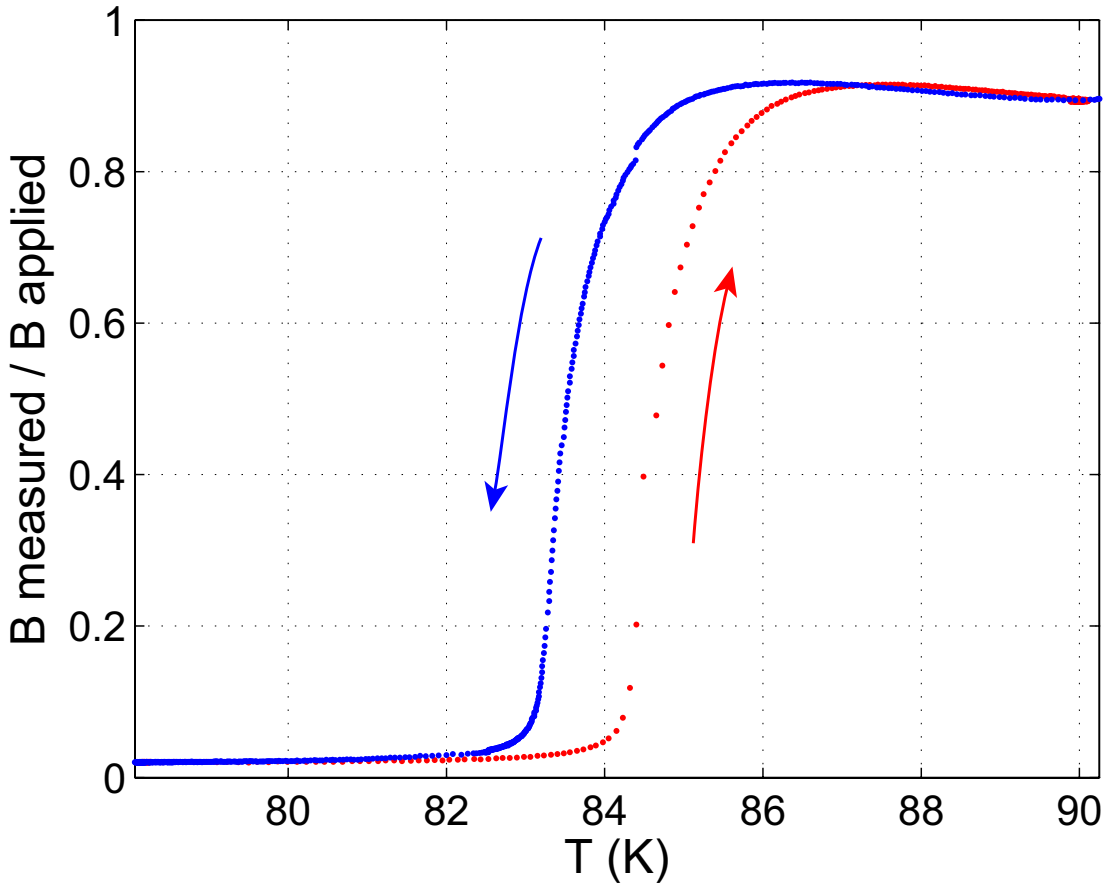

Figure 3.6: Meissner shielding by an *unetched* piece of YBCO. The 5 mm square piece was taken from the same film as that used to make the rings. The plot shows the ac magnetic response to an ac applied field measured by a Hall probe under the piece. The rapid onset of diamagnetism below about 84 K demonstrates that the film superconducts. The hysteresis suggests that the thermometer temperature leads the sample temperature due to imperfect thermal connections. That the response above T_c is not equal to the applied field is likely due to inaccuracy in the Hall coefficient used to convert Hall voltage to field. Below T_c, the shielding is not expected to be complete because of some separation between the sensor and sample surface, but this separation is small (microns) relative to the size of the sample (millimeters). This is not the case for the micron-size ring.

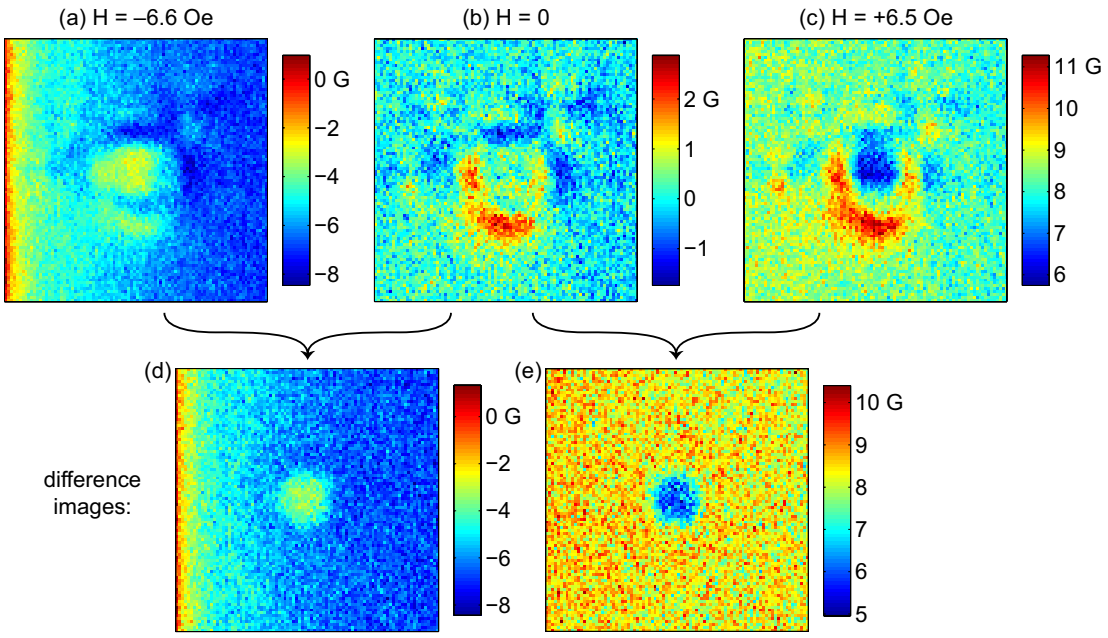

Figure 3.7: Scanning Hall probe images of a YBCO ring at 68 K with various applied fields. Images (d) and (e) are the differences between (a) and (b), and (c) and (b). The difference images reveal Meissner shielding, the expected magnetic response, demonstrating that the ring superconducts. The features in (b) (where one would expect no magnetic response) are probably due to an electric effect.

from the other scans, however, does yield the expected response, as seen in Figures 3.7(d) and (e), aside from a uniform gradient in Figure 3.7(a). This suggests that Figures 3.7(d) and (e) represent the magnetic response, and the other features (approximately the features in Figure 3.7(b)) arise from electric interactions between sensor and sample that are independent of applied field, but dependent on sensor position. An example is charge trapped on the sample surface depleting an area of the sensor's 2DEG, or a piezoresistive effect on the sensor due to the topography of the ring.

3.6.2 Realignment

Seeing the superconducting magnetic response in the scans gave me confidence that the ring was detectable with my setup. The main difference between my static sensor and the scanning sensor was alignment of sensor and sample. Alignment in x and y direction is known to be adequate (i.e. better than the size of the ring) from optical images as described in Section 3.4. The vertical distance (height) between sample and sensor, though, is unknown and, in retrospect, was probably the most important hurdle to measuring a response from the ring.

Suspecting height to be the problem, I tried remounting the sample, pressing it firmly onto the Hall sensor by hand with tweezers. If the gap between the two is primarily due to the heatsink paste, as opposed to some hard contaminant, pressing should spread out the paste and decrease the gap.

The immediate result was a broken Hall sensor. A second, more gentle try, however, met with some success.

3.7 Superconducting transition in susceptibility

My first measurement of superconductivity is only that in retrospect; it takes the form of a dubious kink in the magnetic response a function of temperature, shown in blue in Figure 3.8(a). Here, I apply an ac magnetic field and run a dc current through the Hall sensor, locking in on the ac component of its tranverse voltage.

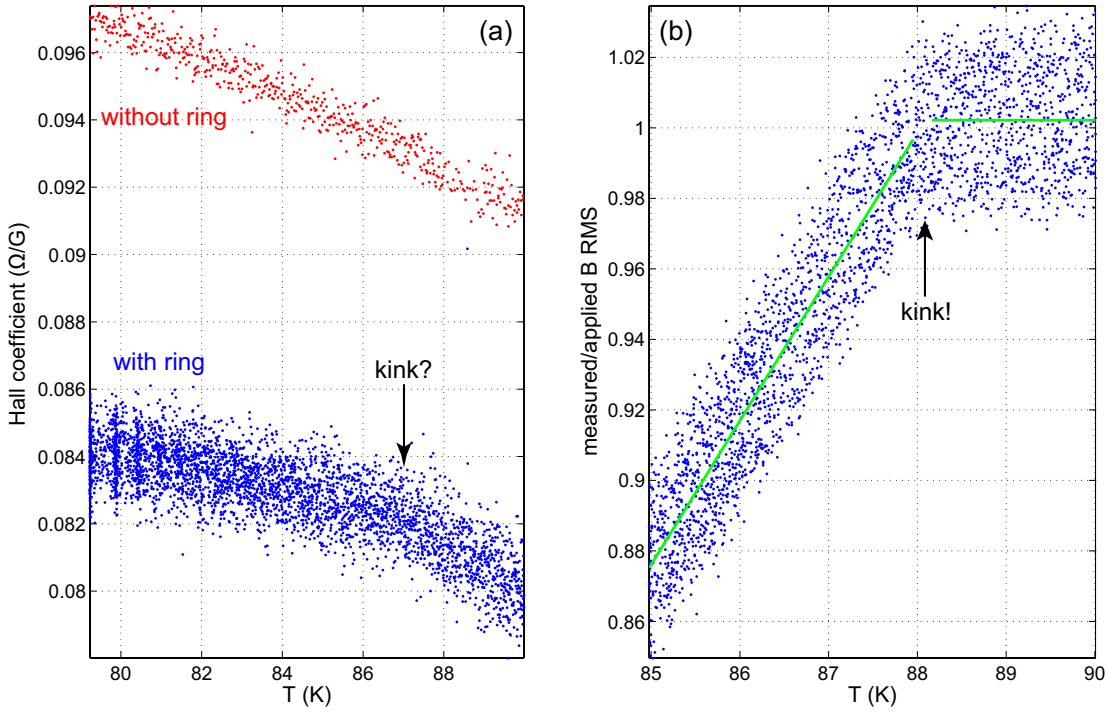

Figure 3.8: (a) First evidence of superconductivity: The temperature dependence of the Hall sensor response to an ac applied field with the superconducting ring (blue dots) exhibits a downward kink, which is absent for the bare probe (red dots) and suggestive of Meissner shielding below T_c. The signal-to-noise ratio, however, could use improvement. (b) In the final sample mounting, the kink at the onset of Meissner shielding is clear. The Hall coefficient of the bare sensor is already divided out from the response measured with the ring in place.

The plot shows the voltage amplitude divided by current and field amplitude to obtain a Hall coefficient.

Smooth variations in the response with temperature can be explained as genuine changes in Hall coefficient, plotted in Figure 3.8(a) in red. The kink, on the other hand, suggests that the ring shields the field at the sensor, with the shielding strength growing from zero as the temperature drops below a T_c of 87.2 K. For comparison, the sensor is measured in a separate cooldown without any sample, and the kink is absent. The overall magnitude also changes, possibly due to different alignment of the sensor in the solenoid or a change in the Hall coefficient between cooldowns.

I remounted the sample one last time with much better results, shown in Figure 3.8(b). In this plot, the actual Hall coefficient, calculated from another data set, is divided out from the measured response. Above T_c, I measure only the applied field, as expected, and the shielding current turns on below T_c, increasing as the temperature decreases several degrees. This is Meissner shielding, turning on as the sample transitions to the superconducting state.

3.8 Flux decay

Given that I could measure shielding currents in the ring, my first approach to measuring the pinning force of an individual vortex was to consider the time necessary for that vortex to hop via thermal activation. This process underlies flux creep, detrimental to persistent currents in superconducting magnets [Tinkham, 1996a].

Vortex hopping can be induced by a change in applied field. Analogous to the strip in Section 1.2, the ring lowers its magnetic energy by admitting or expelling vortices to match the applied field, with an energy barrier arising from the suppression of superconductivity at the vortex core.

In Figure 3.9, I plot time traces from the Hall sensor starting 1 s after I change the field from ±48 G to zero. This is accomplished by applying a 101 mA dc current to the solenoid (with a Keithley 220 current source), and turning off

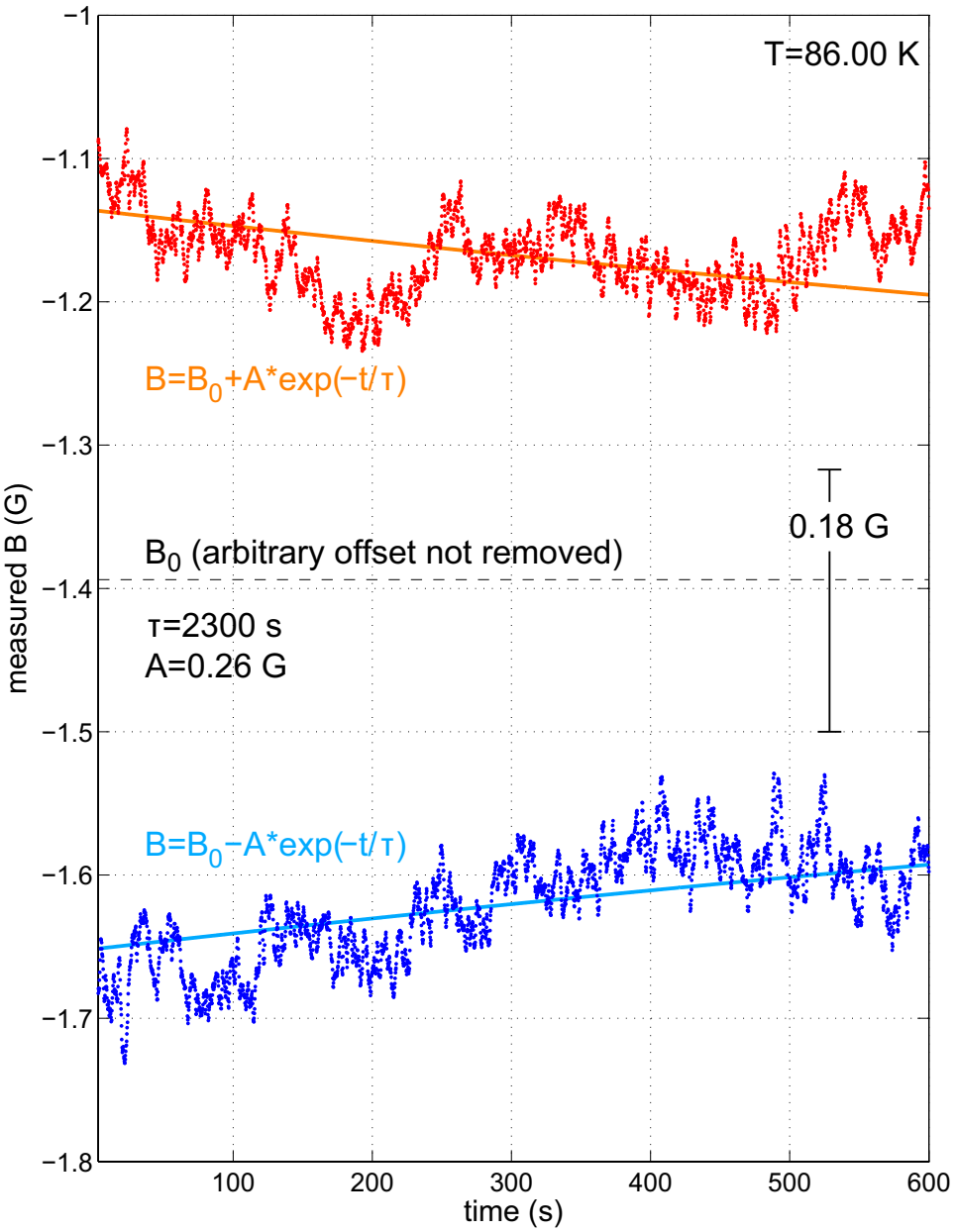

Figure 3.9: The magnetic field from the ring 1 s after ±48 G applied fields are extinguished. A constant offset (arbitrary) is not removed. The time traces (red and blue dots) are the average of 10 iterations. Exponential fits (orange and light blue lines) suggest that the ring's magnetization is decaying, but Hall sensor noise obscures any features such as single vortex steps. The estimated size for such steps is 0.18 G, based on the ring's area and visibility (see Section 3.9.2).

(setting to standby) the Keithley's output while recording the Hall voltage. I confirmed with an oscilloscope that any current oscillations due to the solenoid's inductance are damped out within 1 s.

After the applied field is extinguished, the ring's field remains. It appears from exponential fits to the time traces that this field does decay toward zero with a time constant of 2300 s. I observed such a decay in tens of measurements over temperatures from 85.5 to 87.8 K, thus it is not a fluke, and points to vortex hopping.

However, these results are unsatisfying for two reasons. First, the time traces are dominated by low-frequency noise that prevents observation of features such as individual flux jumps. Second, the time scale for thermal activation depends exponentially on on the energy barrier, and with this setup I am limited to measuring over approximately three orders of magnitude in time.

3.9 Magnetization loops

Instead of waiting for a combination of applied field and thermal activation to induce vortex movement, I can force vortices into the ring by overcoming the barrier with the applied field. Thermal activation is still present, but is less important because of the changing applied field, and the shorter dwell time at a given applied field (9 s, with a lock-in time constant of 1 s).

In Figure 3.10(a), the Hall response ("measured B," converted to Gauss as described below) is recorded while the field (H or "applied B") is ramped from -200 to +200 Oe. The response is dominated by the applied field itself, but the ring adds a small amount of hysteresis. In Figure 3.10(b), the ring's contribution is isolated by subtracting the applied field. This difference is proportional to the ring's magnetization, with the constant of proportionality determined by the geometry of the ring and location of the sensor.

The ring starts at the origin with zero magnetization after cooling in zero field. It follows the green curve, shielding the positive applied field. At +24 Oe, however, its response falls short of linear, indicating that a vortex has started to

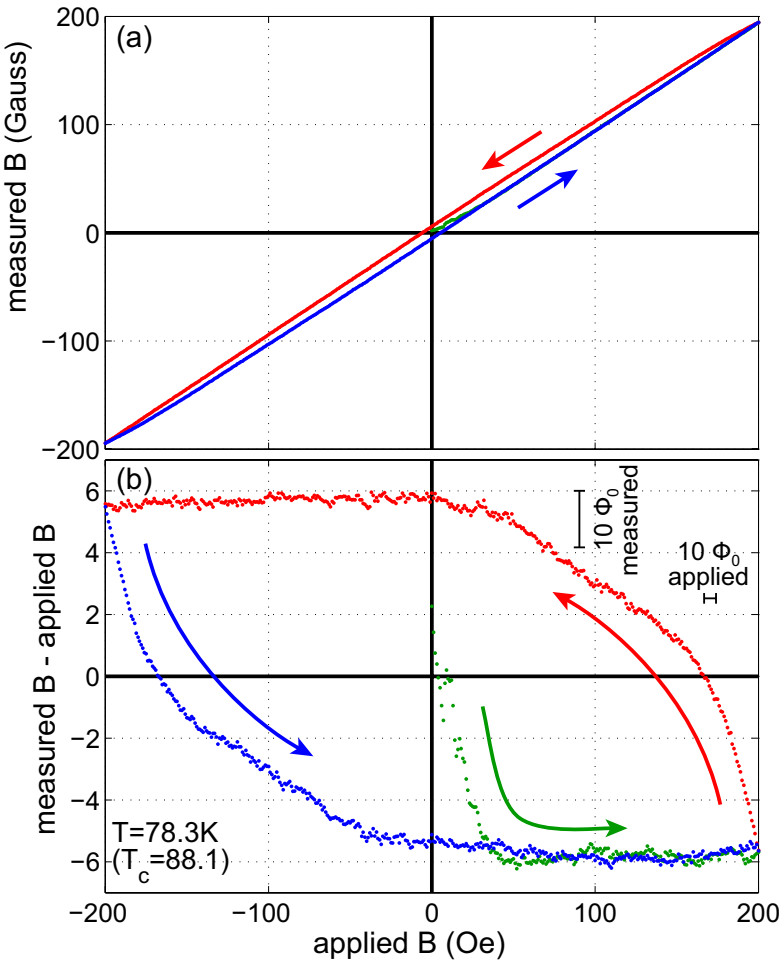

Figure 3.10: (a) The response of the Hall sensor with the ring to an applied field. The main contribution is from the applied field itself, but subtracting the applied field in (b) isolates the ring's response. Hysteresis in this response arises from about 30 vortices that are forced into the ring and remain there until erased by vortices of the opposite sign.

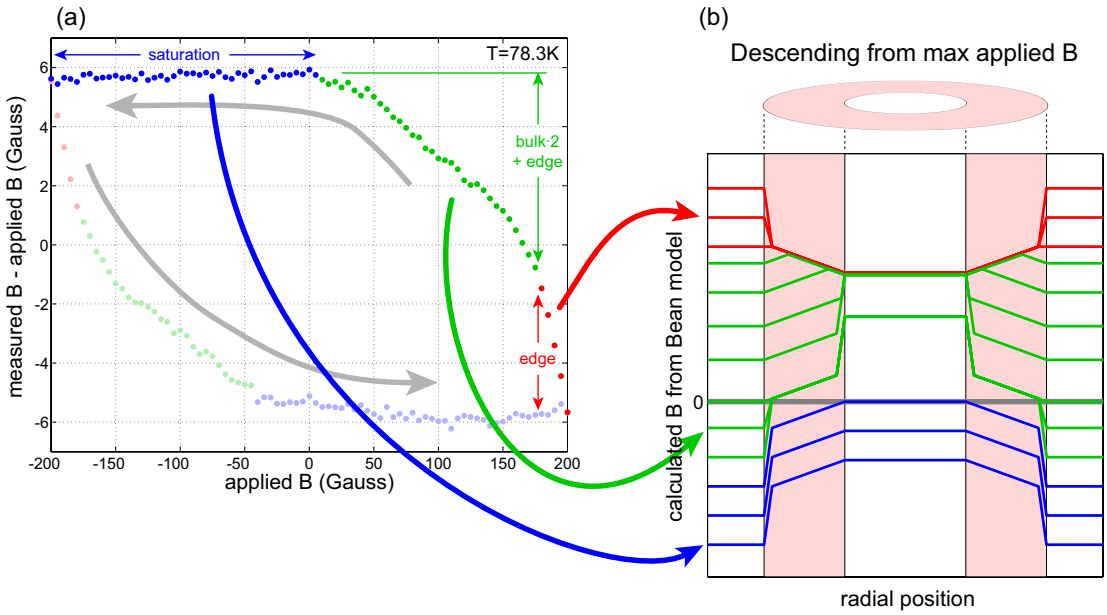

Figure 3.11: (a) The ring's response to an applied field is broken down into contributions from bulk and edge currents based on the Bean-Livingston model with a surface barrier.

move into the ring. Vortices may get pinned within the bulk of the ring, rather than moving into the hole in one jump. As H increases further, the shielding levels off—the ring has reached its critical current density, J_c, beyond which vortices depin and enter the ring, reducing the current back to J_c. These sections of the magnetization loop are identified in Figure 3.11(a). From the different sections I extract several parameters which combine to yield the critical current density, J_c, or equivalently the vortex depinning force, $F_p = \Phi_0 J_c$.

3.9.1 Hall coefficient

To extract this quantitative information, I first need to translate Hall voltage to field via the Hall coefficient, R_H. The Hall coefficient of this sensor is not calibrated from a separate cooldown without the ring, as was done for an earlier sensor in Section 3.5. I can, however, extract R_H from the magnetization

loops using the slope of measured voltage versus applied field on the portions of the curve in which the ring magnetization is "saturated" (see Figure 3.11(a)). The magnetization stays approximately constant, oscillating around a maximum magnitude, thus the change in B seen by the sensor is only due to the change in applied field. I fit the two regions (increasing and decreasing H) separately and average the two slopes to obtain R_{H}. I am, in effect, assuming a field-independent critical current over these regions (∼0–200 G), which is justified by macroscopic transport measurements of YBCO [Daniels et al., 2000].

R_{H} calculated in this manner is already applied to the data in Figures 3.10–3.11, effectively forcing the saturated regions in the magnetization loops to be horizontal.

3.9.2 Visibility

In addition to the Hall coefficient, the placement of the sensor relative to the ring factors into the ratio between the current flowing in the ring and the Hall response measured. This factor is determined by the "Meissner" regions in Figure 3.10(b), where I assume there is no vortex movement; the current at the outer edge of the ring changes to shield the change in applied flux over the ring area. The shielding seen by the sensor, which I call the "visibility" of the ring, dies off as the ring moves away from the sensor, with the characteristic length set by the 14 μm diameter of the ring, as shown in Figure 3.12. The visibility is the dimensionless ratio between the measured magnetization and the magnetization one would measure if the sensor were perfectly matched to the ring area, i.e. perfect diamagnetism yielding a magnetization opposite the applied field.

To quantitatively model the relation between visibility and ring position, I make several idealizations. I assume the sensor is centered below the ring. The sensor signal is taken to be the average of B_z over a square of side length s=2.5 μm. The ring's outer diameter R is 13.8 μm, and its thickness is made infinitesimal; the shielding current becomes a sheet current. The sheet current density is approximated to be constant within a London penetration depth λ=400 nm inward

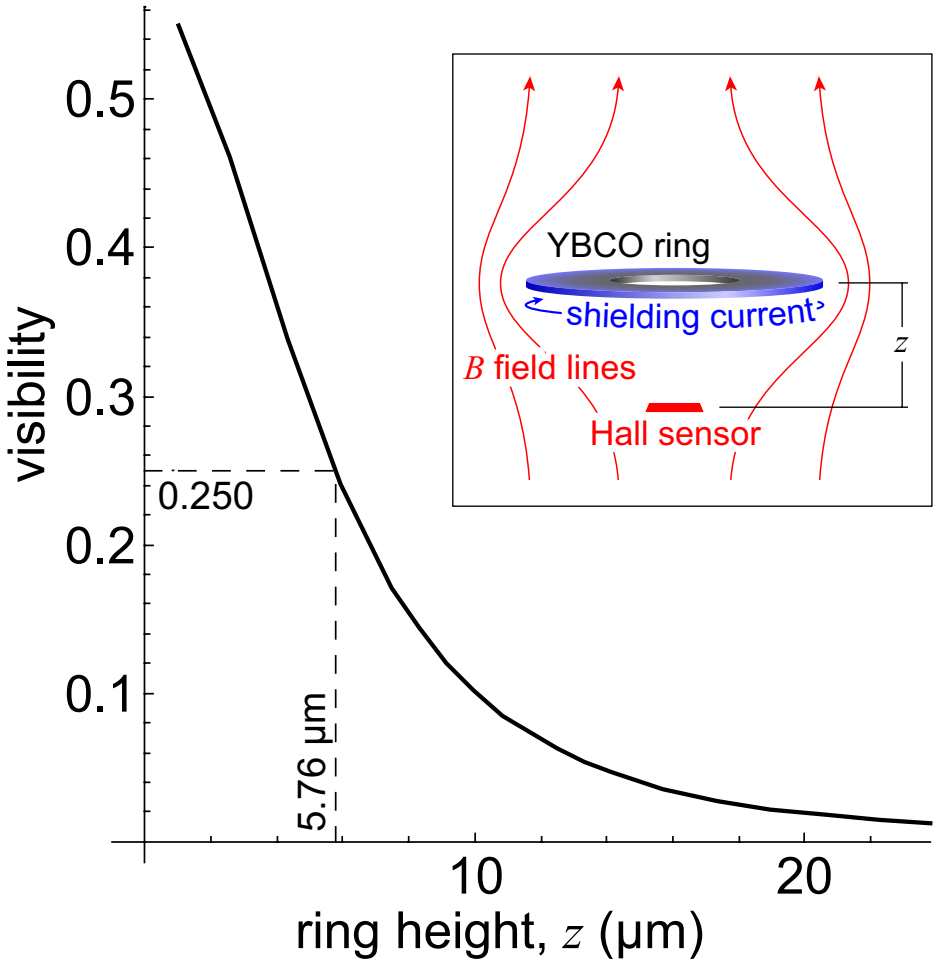

Figure 3.12: The calculated "visibility," or fraction of full Meissner shielding, that the Hall sensor would see as a function of its separation from the ring. The arrangement modeled is depicted in the inset.

from the outer edge of the ring and zero elsewhere; thin film demagnetization currents in the bulk of the ring are ignored. For purposes of this calculation, the ring is equivalent to a superconducting disk; its hole does not matter.

I start with an applied field and calculate the shielding current necessary to cancel the applied flux, i.e. the current such that the integral over the area of the ring of the magnetic field generated by the current is the opposite of the applied field multiplied by the same area. I then calculate the magnetic field at the sensor due to this ring current, and average over the sensor area. Dividing by the applied field yields the visibility. The result is plotted in Figure 3.12. Quite reasonably, the visibility drops off over a characteristic length approximately equal to the size of the ring, 14 μm.

The visibility is measured as the slopes of linear fits to the Meissner regions shown in Figure 3.11(a). The two regions are fit separately and their slopes averaged, yielding 0.25. For this value, the calculated curve in Figure 3.12 suggests that the ring was about 6 μm away from the sensor—a plausible conclusion in retrospect. In my earlier attempts, described in Section 3.6, this separation was likely larger, making the visibility too small, which prevented me from seeing the ring.

3.9.3 Translating into critical current: Bean model with surface barrier

The ring height determined from the visibility allows me to calibrate the actual ring magnetization throughout the magnetization loop. In particular, the maximum magnetization can be translated into a critical current. This translation is similar to the calculation of visibility as a function of ring height. For the known ring height, a current in the ring will produce a calculable contribution to the magnetic field averaged over the sensor area. Inverting this relation, the measured field determines the magnitude of the current. One can make various assumptions, however, about the distribution of the current.

At saturation, I assume a uniform current density over the bulk (as opposed

to the surface) of the ring, in accordance with the Bean model [Bean, 1964]. This produces the constant slope dB/dx shown in the bulk in Figure 3.11(b). However, the Figure also shows that I assume an increased current density at the edges in some regimes. This allows me to account for the red "Meissner" regime identified in Figure 3.11(a), where the magnetization initially varies linearly with the applied field, rather than parabolically as the Bean model would predict. This is the addition of a Bean-Livingston surface barrier (i.e. edge barrier) [Bean and Livingston, 1964].

Physically, the barrier implies that vortices remain pinned in the presence of supercritical current density because of an additional force attracting them to the edge of the superconductor. This force arises because of the asymmetry of the vortex current necessary to accommodate the boundary condition imposed by the edge. The current can be calculated (and London's equations satisfied in the superconductor) by superposing an undisturbed vortex with its image (of opposite sign) reflected over the edge, thus its attraction to the edge is equal to its attraction to such an antivortex.

So there are two currents that contribute to the ring's magnetization in the saturated (blue) region of Figure 3.11(a): uniform critical current density in the bulk, and increased current flowing at the outer edge. The magnitude of the edge current is calculated from the change in magnetization over the red Meissner region, over which this current is reduced from maximum to zero. The remaining change (i.e. the change over the green region) arises from reversing the current in the bulk, and then generating a new edge current. Thus by subtracting the edge current magnetization and dividing by two, I obtain the bulk magnetization. I then translate this into a current density using the known height and geometry of the ring. I expect that this current density is comparable to the classic J_c that one might measure for a macroscopic sample of the same material, where edge effects are insignificant.

It is also interesting to convert the edge current into a current density to understand how much the edge barrier can enhance current density locally. This conversion requires knowing the current's spatial dependence, however, which

cannot be determined directly by this experiment. I therefore model the dependence, using two models that estimate upper and lower bounds, respectively, on the true current density.*

In the first model, I calculate the magnetic field strength just outside the outer edge of the ring, then assume this field is screened over a London penetration depth, λ. The current density is then approximately the peak field divided by λ. The demagnetization factor of the ring's geometry, which yields the enhancement of the applied field at the edge, is calculated analytically as that of a diamagnetic spheroid [Stratton, 1941]. Two radii of the spheroid are set to the outer radius of the ring, while the third is set to half the thickness of the ring.

The second model assumes a uniform current density spread over a distance λ inward from the outer edge of the ring. This yields a lower bound on the maximum current density, as the true current distribution will be nonuniform with a higher maximum than the average value. I also account for the increased penetration depth in a thin film, further decreasing the current density [Chang et al., 1992b].

3.9.4 Temperature dependence

The hysteresis loop measurement is repeated for temperatures from 78.30 to 85.75 K, several of which are shown in Figure 3.13. I perform the same analysis on each loop, extracting bulk and edge currents, then translating into current densities. These values are plotted as a function of temperature in Figure 3.14. I also include the average current density, i.e. the sum of bulk and edge currents (rather than just the bulk) divided by the annulus cross sectional area.

At the lowest temperatures, even the lower bound on the edge current density exceeds the bulk value, demonstrating that the edge barrier can significantly enhance current density locally. At higher temperatures, the bulk current density falls between the edge values, thus I cannot make such a strong statement.

In the inset of Figure 3.14, I compare these values to the depairing current

*Better models of the current density distribution in a superconducting ring have been published since [Brandt and Clem, 2004].

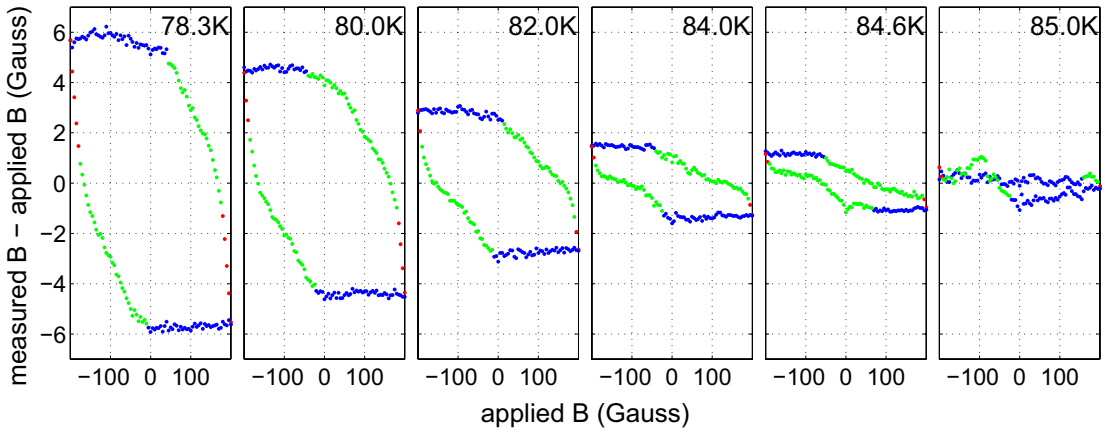

Figure 3.13: Magnetization loops of the ring at several temperatures. The magnitudes of bulk and edge currents are extracted from these data.

density, calculated from the temperature-dependent coherence length, ξ, and penetration depth, λ, as [Gurevich, 2006]

$$J_{\mathrm{d}} = \frac{\phi_0}{3\sqrt{3}\pi\mu_0\lambda^2\xi}. \tag{3.1}$$

This is the current density above which superconductivity becomes thermodynamically unstable, i.e. the current's kinetic energy density exceeds the energy savings of superconductivity, thus the system would lower its energy by going normal. It also translates to the current necessary to depin a vortex from an ideal columnar pinning site [Gurevich, 2006]. The plot shows that J_{c}—and therefore pinning—in this material is about 10 times weaker than this ideal.

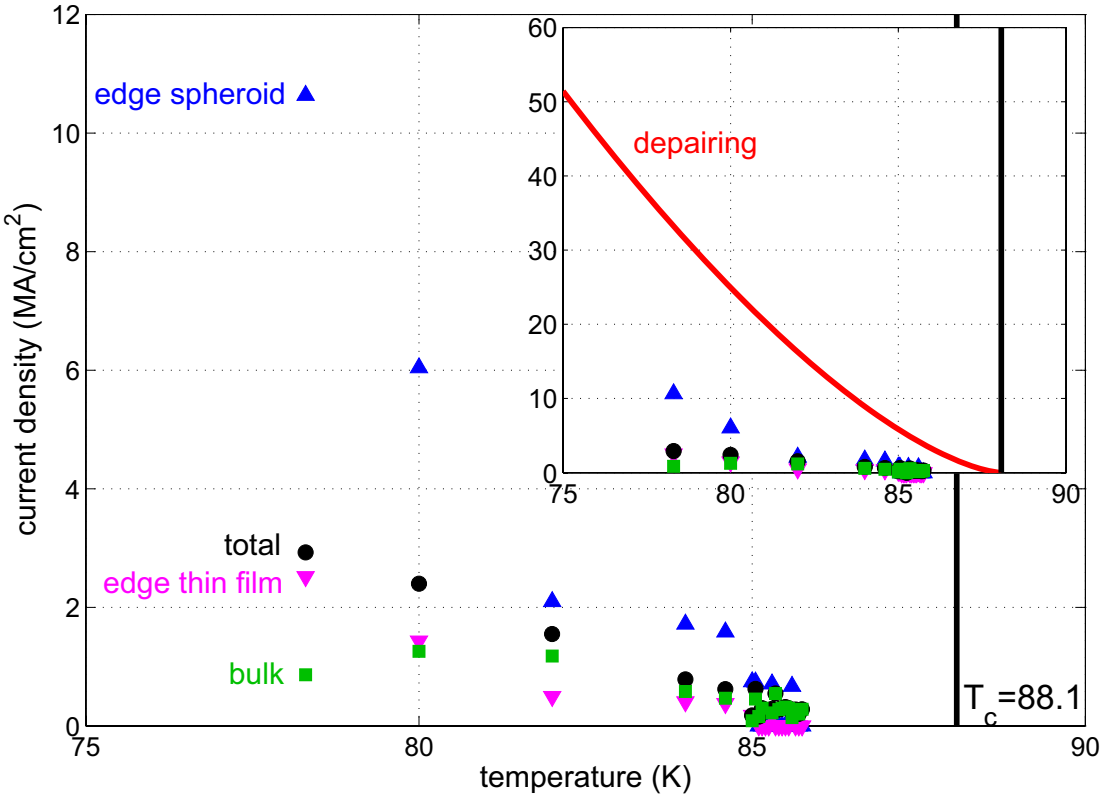

Figure 3.14: The magnitudes of bulk and edge critical current densities as a function of temperature as calculated from magnetization loops. The edge current can be translated into a current density using two models that serve as bounds for the real result.

3.10 Stalking single vortices

Over the non-edge portions (bulk and saturation portions) of the magnetization loop shown in Figure 3.11(a), I claim that vortices are being forced into the ring. One might therefore expect to see steps in the magnetization associated with the entry of individual vortices. Such steps are probably swamped by noise in this data. To pursue these individual vortex steps, I repeated the loop (for a smaller range of applied field) and averaged. The result is plotted in Figure 3.15(a)–(b). If there are periodic values of applied field at which vortices enter the ring, they will remain as the noise is averaged out.

The averaged magnetization loop shows some ripples, but not obvious steps. To examine whether the ripples might arise from single vortex motion, I replot the data as an estimate of the amount of flux in the ring. This is calculated as the magnetization of the ring, plus the applied field, multiplied by the ring's area:

$$\Phi = (B_{\text{measured}}/\text{visibility} + B_{\text{applied}}) \cdot \text{area} \tag{3.2}$$

The result is plotted in Figure 3.15(c), normalized by the flux quantum, with the applied field also multiplied by the ring area and expressed in flux quanta. At the ends of the curve, where the applied flux reverses, I see a Meissner region in which the flux in the ring does not change significantly. On the other portions of the curve, I force approximately 9 vortices into and out of the ring. Arguably, the penetration is not smooth, and contains step-like plateaus, whose smeared out appearance may follow from the averaging. However, the plateaus are not clear or uniform, and their spacing ranges in size rather than being integral multiples of Φ_0.

The data before averaging are shown in Figure 3.16. Here, as before, noise renders any conclusion about steps uncertain. Note that these data were taken in two sets, and only the second set is averaged to obtain Figure 3.15.

I pursue this one step further by averaging an even smaller portion of the magnetization curve over more iterations (275). I acquire data while increasing the applied field, then cycle the field back to zero and repeat. Specifically, I ramp

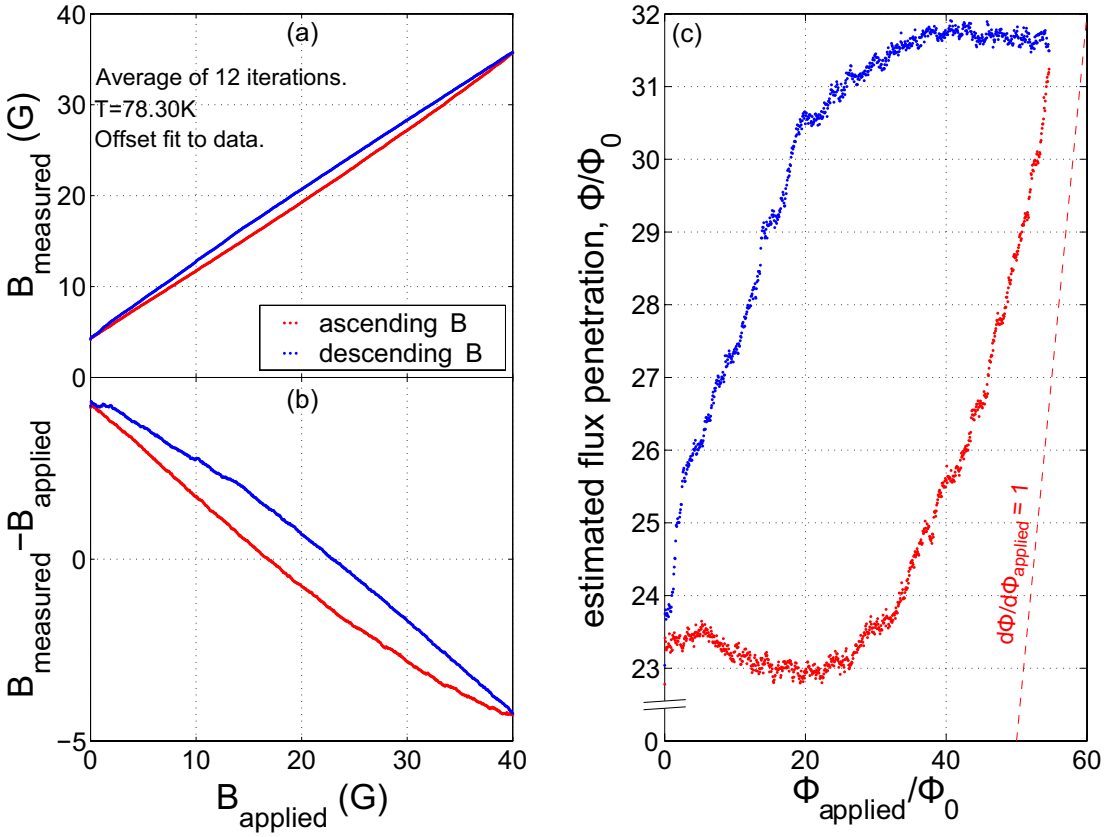

Figure 3.15: Measuring a portion of the magnetization loop repeatedly, I average to look for signatures of single vortex movement. (a)–(b) As in Figure 3.10, I plot B and then subtract off the applied field to obtain a measure of the ring's magnetization. (c) I replot this loop, translating the applied field into applied flux and the magnetization into the estimated flux in the ring, both normalized by the flux quantum. Some step-like plateaus are visible, but not clear, integral steps associated with the appearance of small numbers of vortices.

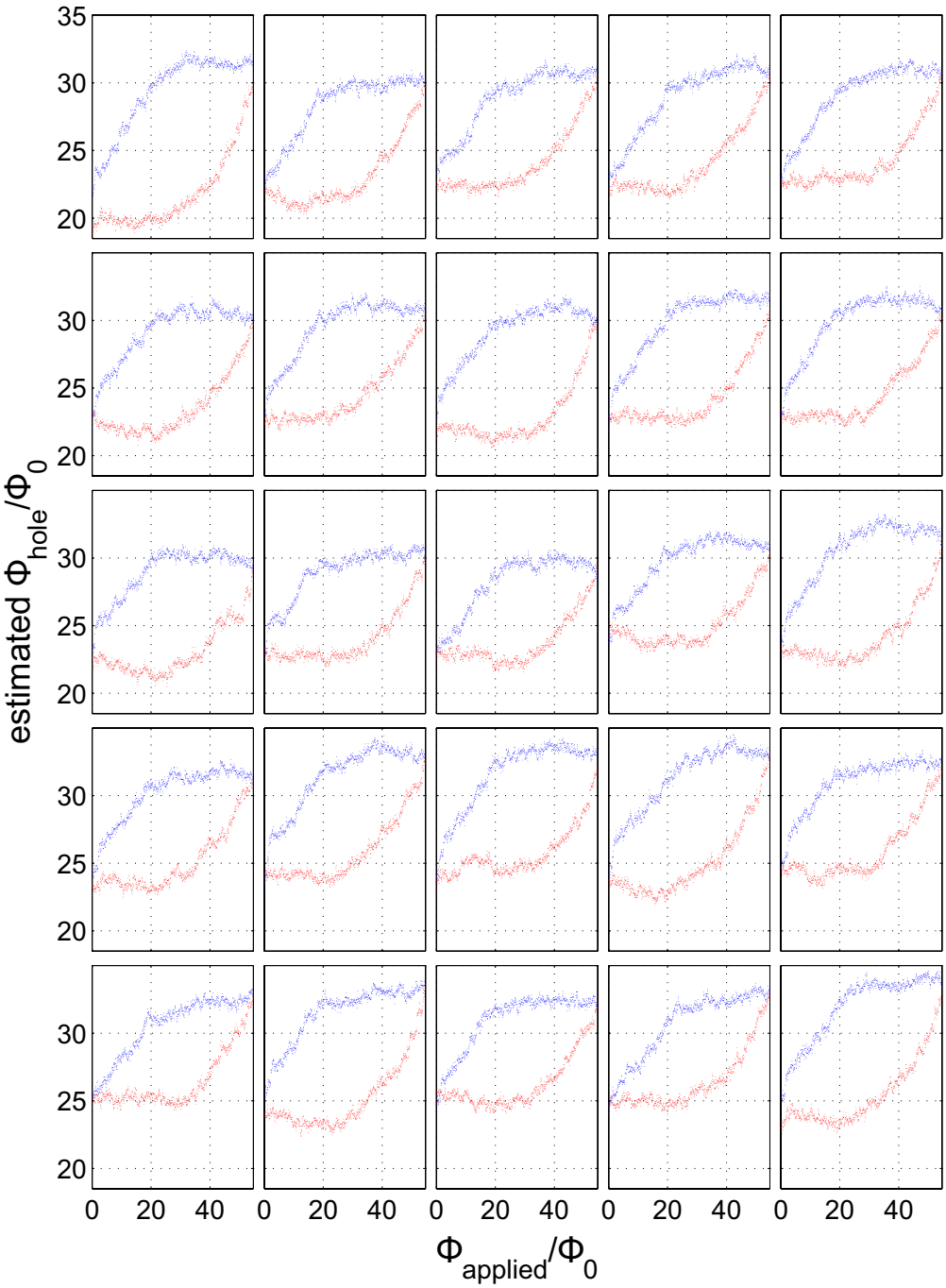

Figure 3.16: Individual loops from two magnetization measurement runs. The second run, consisting of the last 12 plots, is averaged to obtain the previous Figure.

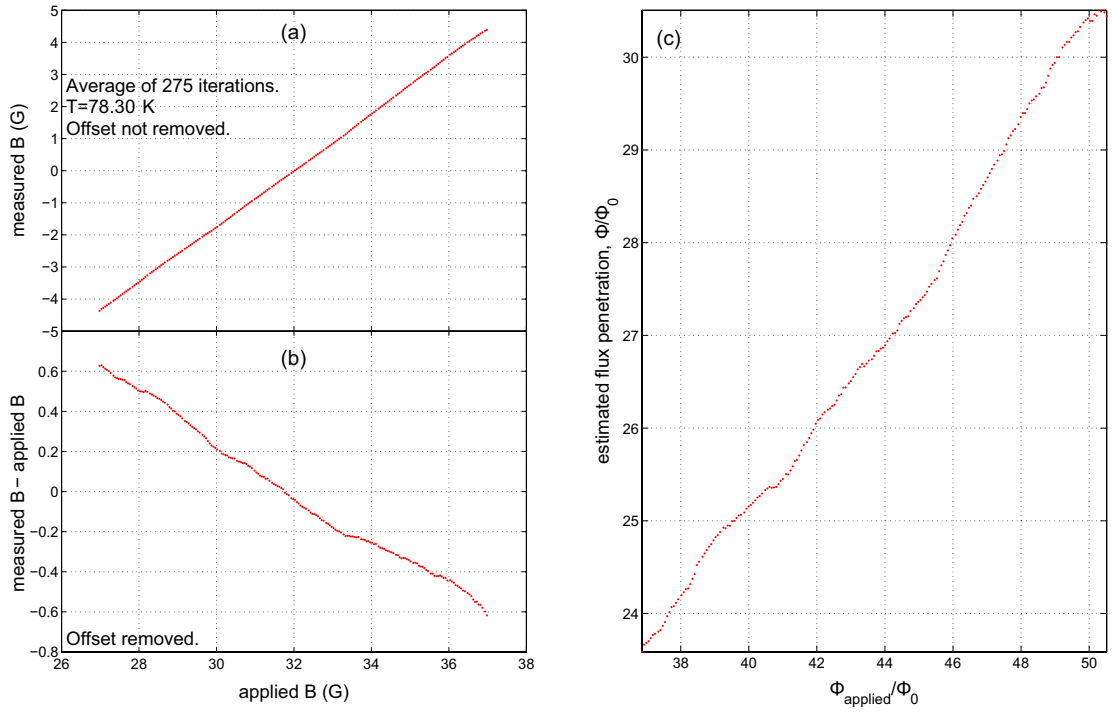

Figure 3.17: A portion of the ascending part of the magnetization curve is measured with more iterations (275), and the same transformations as in Figure 3.15 are applied. Between iterations, the applied field is cycled back to zero.

the field from 0 to 27 Oe in ∼1 s, measure from 27 to 37 Oe in 0.05 Oe steps at 9 s per step, then ramp down to 0 in 1 s, and repeat. Figure 3.17 shows the results, which again show some smeared-out plateaus, but no convincing steps. One could even imagine explanations for these plateaus other than periodic vortex movement, e.g. periodic inaccuracies in instruments such as the magnet power supply.

3.11 Conclusion

The experiments of this Chapter demonstrate that a micro-Hall sensor can detect a few, if not single, vortices in a YBCO ring. The greatest experimental hurdle was reducing the height between the sensor and sample, a lesson which carries over to scanning Hall probe microscopy. Here I reduce that height to 6 μm; in Chapter 5, I achieve 0.6 μm.

I also battled the Hall sensor's low-frequency noise, which rendered the flux decay experiment in Section 3.8 infeasible, and led me to the more successful magnetization loop experiments. However, noise still obscured individual vortex movement. In later experiments, I find better methods of avoiding low frequency noise, such as the time-resolved ac measurement technique described in Section 7.3.

It could also be that that the signature of vortices is not the simple step like structure I have described. As the vortices enter the ring, they likely get pinned at intermediate sites, creating intermediate responses at the Hall sensor. The steps, though still sharp, would be smaller and more easily lost in the noise. Such intermediate steps were observed in a ring of underdoped YBCO by Brian Gardner using a superconducting quantum interference device (SQUID) [Gardner, 2004].

Nonetheless, from the magnetization loops, I was able to extract quantitative information about the ring's critical current, including evidence for a surface barrier. Such information about the spatial distribution of currents is greatly refined by imaging experiments in the succeeding Chapters.

Chapter 4

Stepper motor scanning Hall probe microscope*

4.1 Introduction

The results of Chapter 3 left the details of vortex movement through the sample ambiguous; ambiguities that could be resolved by magnetic imaging. I proceed to construct a magnetic imaging apparatus based on scanning Hall probe microscopy (SHPM).

SHPM has many practical advantages among magnetic imaging techniques [Chang et al., 1992a; Bending, 1999]. It offers submicron spatial resolution and milligauss field resolution. Scanning generally takes at least a second to acquire an image, but the inherent response time of Hall probes is much faster, enabling cyclic phenomena to be imaged with microsecond time resolution as described in this Chapter. For comparison, Lorentz microscopy [Tonomura et al., 1982] offers better than 10 nm spatial resolution and can generate hundreds of images per second, but is limited to samples thin enough (70 nm) to be transparent to electrons. Magneto-optics [Koblischka and Wijngaarden, 1995b] can also image at video rates, but is inferior to SHPM in both spatial and field resolution. Scanning

*Parts of this Chapter are published in Dinner et al. [2005] and are copyright ©2005 American Institute of Physics.

superconducting quantum interference device (SQUID) microscopy [Kirtley et al., 1995] offers excellent field sensitivity, but has not yet achieved submicron spatial resolution, and has a more limited range of sensor operating temperature. Magnetic force microscopy (MFM [Martin and Wickramasinghe, 1987]) offers better spatial resolution than SQUID or SHPM, but at a cost in magnetic sensitivity. MFM also applies a local field large enough to perturb the sample in some cases.

In SHPM, scanning has typically been accomplished with piezos, whose motion is limited and decreases at cryogenic temperatures. Work to amplify the motion of piezos resulted in a scan range of 275 μm at 4 K [Siegel et al., 1995]. A similar range was obtained by maintaining a piezo-based scanning mechanism at room temperature while the sample is cooled [Sandhu et al., 2004]. On the other hand, SHPM has been accomplished with motors and micrometer screws instead of piezos [Gregory et al., 2002], achieving a 5 mm scan range. In that case, however, the minimum pixel spacing was limited by the motors to 1.25 μm.

In the present work, I also use motor-driven micrometers, but couple them to improved electronics and reducing gears to achieve resolution that is comparable to piezo-based Hall probe scanners and limited by the sensor rather than the scanning mechanism. As a result, I can image magnetic fields over centimeters of a sample, identify smaller areas of interest, and zoom in to image those areas with submicron resolution.

Applications of this multiscale characterization include material inhomogeneities or phase segregation, artificially patterned magnetic media, and arrays of mesoscopic devices. Well controlled, long-range motion is convenient whenever alignment to a sample feature is necessary, and to maintain this alignment between room and cryogenic temperatures, compensating for thermal contraction. For instance, one could use the large scan range to align to nanopatterned circuits and image current flow. As a materials example, coated conductors—high-T_c superconducting tapes—require multiscale characterization to sort out weak spots due a variety of phenomena ranging from mechanical defects on a millimeter scale down to the interaction of a few vortices on the submicron scale of the London penetration depth [Larbalestier et al., 2001]. The results presented here

are precursors to such a study.

Fast turnaround time for changing samples is another element of the instrument design that helps, in the example of coated conductors, to secure the microscope's role in the development of practical materials which are still evolving, leading to many variants. Finally, the system exploits the excellent field sensitivity, spatial resolution, and operating temperature range of micro-Hall sensors.

4.2 Design overview

A sketch of the system is shown in Figure 4.1(a) and a photograph in Figure 4.2. I have adapted a Desert Cryogenics table-top cryogenic probe station,* normally used for manually positioning electrical probes on a cooled sample. In my instrument, a computer-controlled positioning stage rasters a Hall sensor over the sample surface. Measurements of the sensor's Hall resistance at a grid of positions on the surface are reconstructed into $B_z(x, y)$, an image of the vertical component of the local magnetic induction. The positioning stage is outside the cryostat; its motion is fed through to the vacuum chamber via flexible bellows. For further discussion of this design choice, see Section 4.7.3.

Figure 4.1(b) is a magnetic image of the sample depicted in Figure 4.1(a). A film of the high-T_c superconductor $YBa_2Cu_3O_{7-\delta}$ (YBCO), grown by Jeong-uk Huh, is patterned into a bridge, approximately 600 μm long by 150 μm wide, and 300 nm thick. The entire structure occupies only a small portion of the instrument's 1×4 cm scan range.

The bridge is imaged at 50 K. At each pixel, DC currents of $+100$ and -100 mA are applied, and the corresponding magnetic fields are measured. Half the difference between the fields is scaled according to the color scale shown and plotted for each point. Retaining only the difference between the two fields measured reduces effects of time variation in the sensor and any background field. A similar technique is described in more detail in Section 7.3.

*Desert Cryogenics is now a division of Lake Shore Cryotronics, Inc., http://www.lakeshore.com.

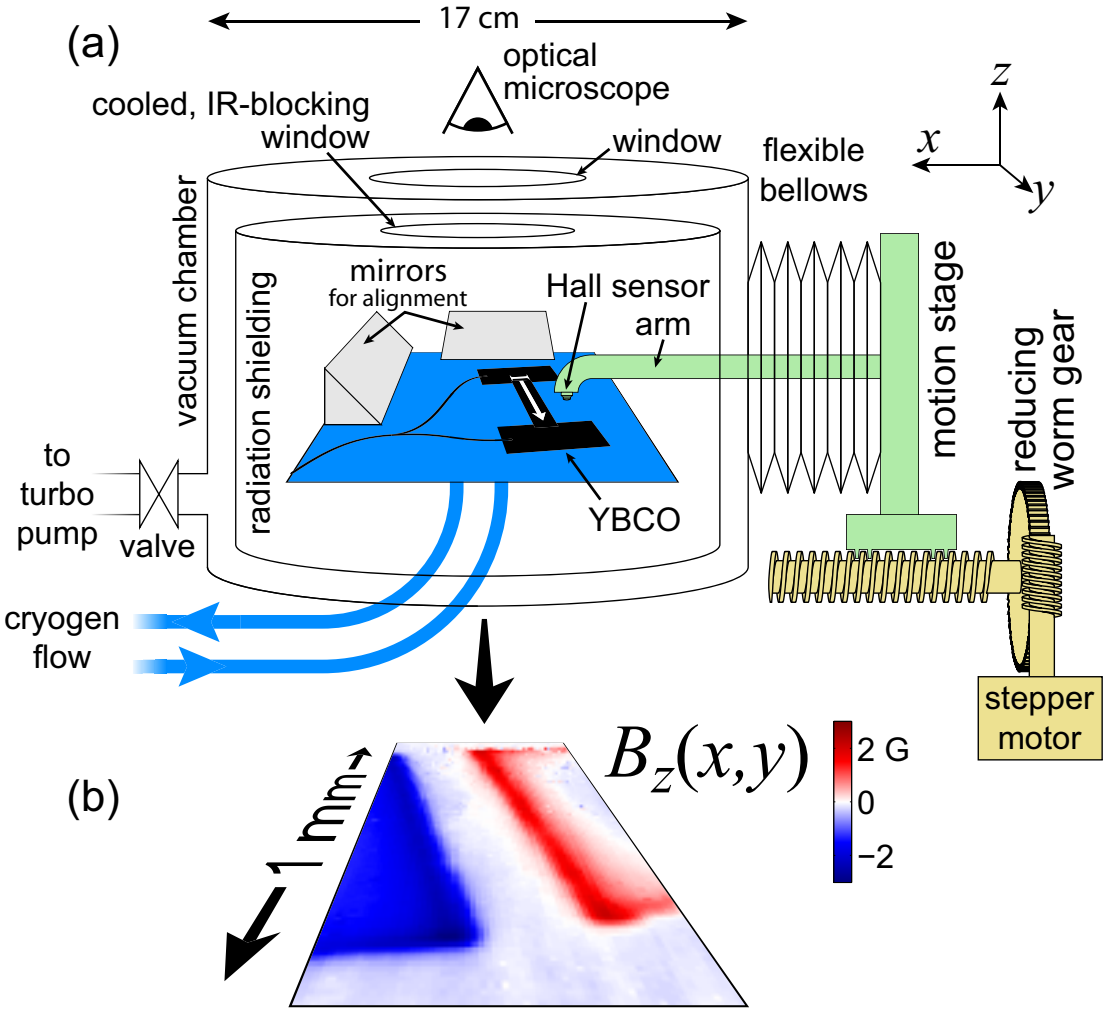

Figure 4.1: (a) Sketch of the large area scanning Hall probe microscope. A flow cryostat cools the sample. A Hall sensor is rastered over the sample surface. The sensor position is controlled by an external, stepper motor-based stage. The cryostat allows optical access from above and, via mirrors, from the sides. (b) Magnetic image of a mm long YBCO strip carrying 100 mA. This image uses only a fraction of the instrument's cm scan range.

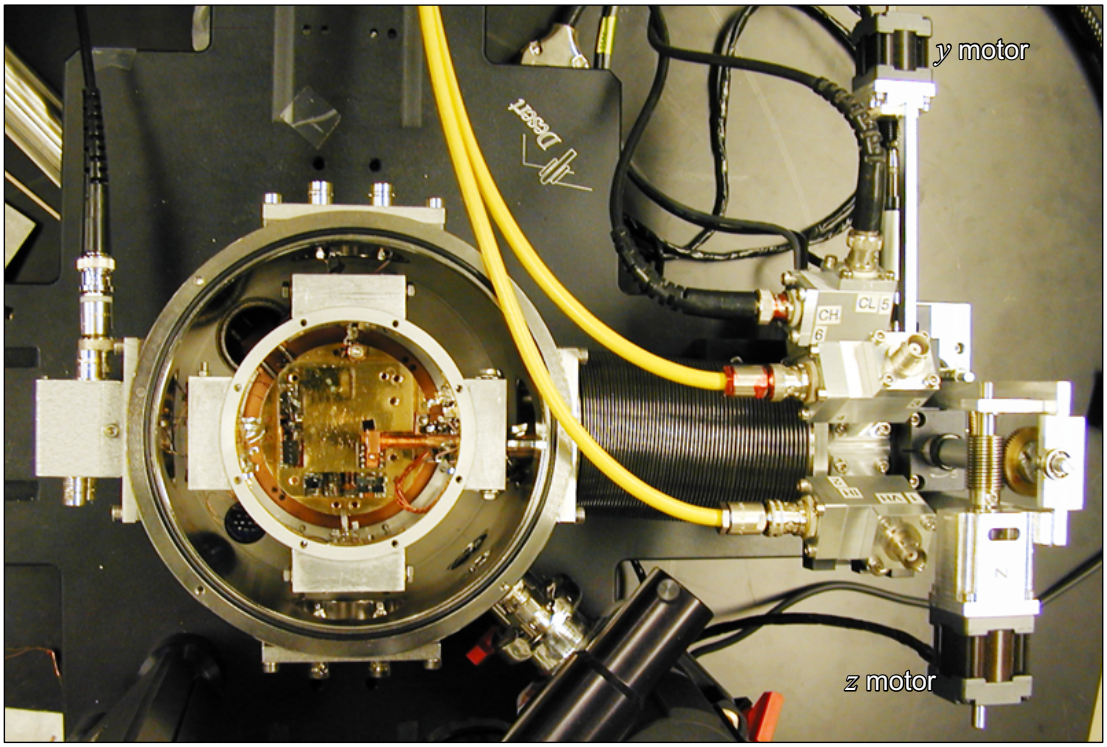

Figure 4.2: Photograph of the scanner from above ($+z$). The covers of the vacuum chamber and radiation shield are removed, revealing the gold-plated copper sample stage with mirrors and a square piece of YBCO below the end of the sensor arm.

The applied currents are well below the expected critical current (3 A), and the superconductor displays the Meissner effect, with most of the current flowing along its edges. A line cut across the strip taken from the magnetic image is well modeled by accounting for thin film demagnetization effects and ignoring the strip's finite length [Zeldov et al., 1994]. The ease of aligning to and acquiring such a cut across the center of the bridge demonstrates this instrument's advantages over previous designs.

4.3 Stepper motor-based linear motion

The instrument's scan range and resolution result from a custom three-axis linear motion stage, shown in Figure 4.3. I modified the manually manipulable stage included with the Desert Cryogenics probe station, coupling its micrometer screws to stepper motors. The pieces slide via rails that ride on crossed roller bearings. The motors are from Oriental Motor Co.'s VEXTA CFK II series, chosen for their high resolution and small size. The z and y axes each use a model PMM33BH2 motor, and the x axis uses a PK543NBWA. Each motor is powered by a model DFC5107T driver and takes 500 full steps per revolution of its shaft. The driver is capable of microstepping (holding the motor at positions between steps) with a nominal minimum increment of 1/250 full steps, though I have not characterized the accuracy of microstepping down to this resolution.

For the x axis, a 2 mm pitch screw is attached to the base of the cryostat by thrust bearings and mates to a Delrin nut on the stage, driving the stage along its rails as the screw turns in place. An 80-tooth worm gear with incorporated anti-backlash springs is clamped to the end of the screw and is turned by a double-thread worm attached to a motor, reducing the motor's movement by a factor of 40. As a result, the stage is expected to move 100 nm per step, with a nominal minimum microstep of 0.4 nm. The full range of the x stage is 5 cm.

The y stage is attached via rails to the x stage and driven by a 0.5 mm pitch screw. A motor shaft is attached directly to one end of this screw via a flexible coupling meant to convey rotations but reduce radial force. The stage moves

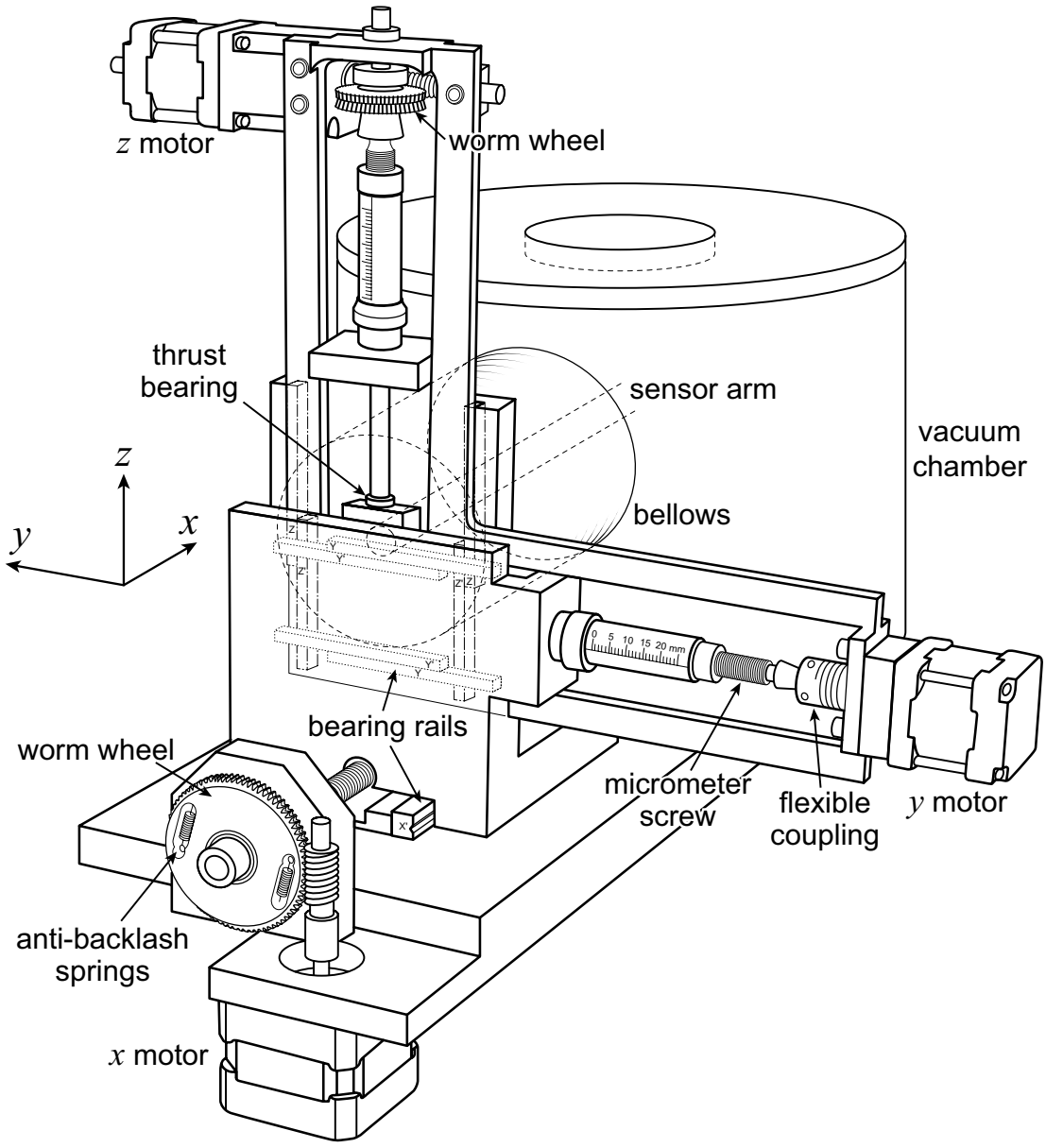

Figure 4.3: Sketch of the three-axis stage that moves the sensor arm. Stepper motors drive micrometer screws to generate linear motion. For the x and z axes, worm gears first reduce the motors' rotation; for the y axis, the motor is coupled directly to the micrometer screw.

1 μm per full step, 4 nm per microstep. The y range is limited to about 1 cm by the large force need to stretch the bellows when the stage moves off center. This force creates friction in the micrometer and the stage that must be overcome by the motor.

All scans are rastered with scan lines in the y direction, from bottom to top, each line followed by retracting to the bottom y position and moving one increment along the x axis, from left to right. Having no gear reduction on the y axis makes it capable of moving at 20 mm/s, though I typically operate at one tenth of that speed. Even for a scan with a large pixel spacing such as 10 μm, the time taken moving between pixels is smaller than the time taken measuring at each pixel, typically 0.1 to 0.5 s. Thus a 200×200 pixel scan would take several hours, and take only slightly longer with increasing pixel spacing.

The z stage couples to the y stage and shares most of its features, but inserts a 60-tooth, double-thread, anti-backlash worm gear between the motor and screw, reducing the step size to 33 nm per full step, 0.13 nm per microstep. The z motion is limited above by the arm hitting the top of the port in the radiation shield and below by the sensor hitting the sample stage, resulting in a range of 7 mm. Finally, the sensor arm bolts to the z stage. The position of each pixel in the images below is calculated from the number of steps input to the x and y stepper motors; I have not attempted to correct for position-dependent tilting of the arm or other factors that might (and probably do, as described below) prevent the sensor from moving exactly as predicted from the step size and gearing.

Combining the high resolution of the stepper motors and the reducing gears, then, the minimum step sizes for all axes are in the nm range. However, the sensor movement shows backlash of several microns, probably reflecting some rotational play in the stage amplified by the length of the sensor arm. I deal with backlash by always approaching from one direction ($-x$, $-y$, and $+z$) and find good unidirectional repeatability, as quantified in Section 5.4.

4.4 Sensor-sample alignment

A CCD camera coupled to a microscope looks directly down at the sample stage. It can zoom out to an area of 6.6 × 5.0 mm, or zoom in for 3 μm resolution. To determine the sensor's height, H, relative to the sample, the two are viewed from the side via mirror wedges with angles slightly greater than 45°, as shown in Figure 4.1(a).

The measurement of H is refined by touching the sensor to the surface at several points and recording the z positions at which the sensor touches down, as measured by a capacitive touchdown cantilever, illustrated in Figure 4.4(a)–(b). The sensor is mounted on a copper foil cantilever (approximately 10 mm long, 4 mm wide, and 20 μm thick), one end of which is attached to a copper plate but electrically isolated by a piece of glass. The cantilever and plate are separated by $\sim$ 100 μm, forming a capacitor that allows one to detect when the Hall sensor is touching the sample: As the stepper motor stage lowers, the sensor corner near the Hall cross touches the surface first. Upon further lowering, the sensor and cantilever are deflected toward the plate, increasing the capacitance, as in Figure 4.4(c). Prior to touching down, the sensor appears to be slightly attracted to the surface, presumably due to an electrostatic interaction, causing the cantilever to deflect downward and the capacitance to decrease as H decreases. Touchdown is presumed to occur at the change in slope of capacitance versus H.

The change in slope can be identified by eye, but I also use an algorithm to automatically detect several points in succession with systematically higher capacitance than predicted by a linear fit to the preceding points. Then, via linear fits to the points before and after touchdown, I determine the touchdown location with a typical uncertainty of 30 nm. In this way, I find the sample surface, using optical alignment followed by capacitive touchdown, in a couple minutes.

By determining the sample height at several locations, I approximate the plane of the surface. For larger scans where micron resolution is not necessary, the sensor is lifted at least several microns away from the surface, and the height is adjusted at each step to maintain this distance from the known sample plane. To

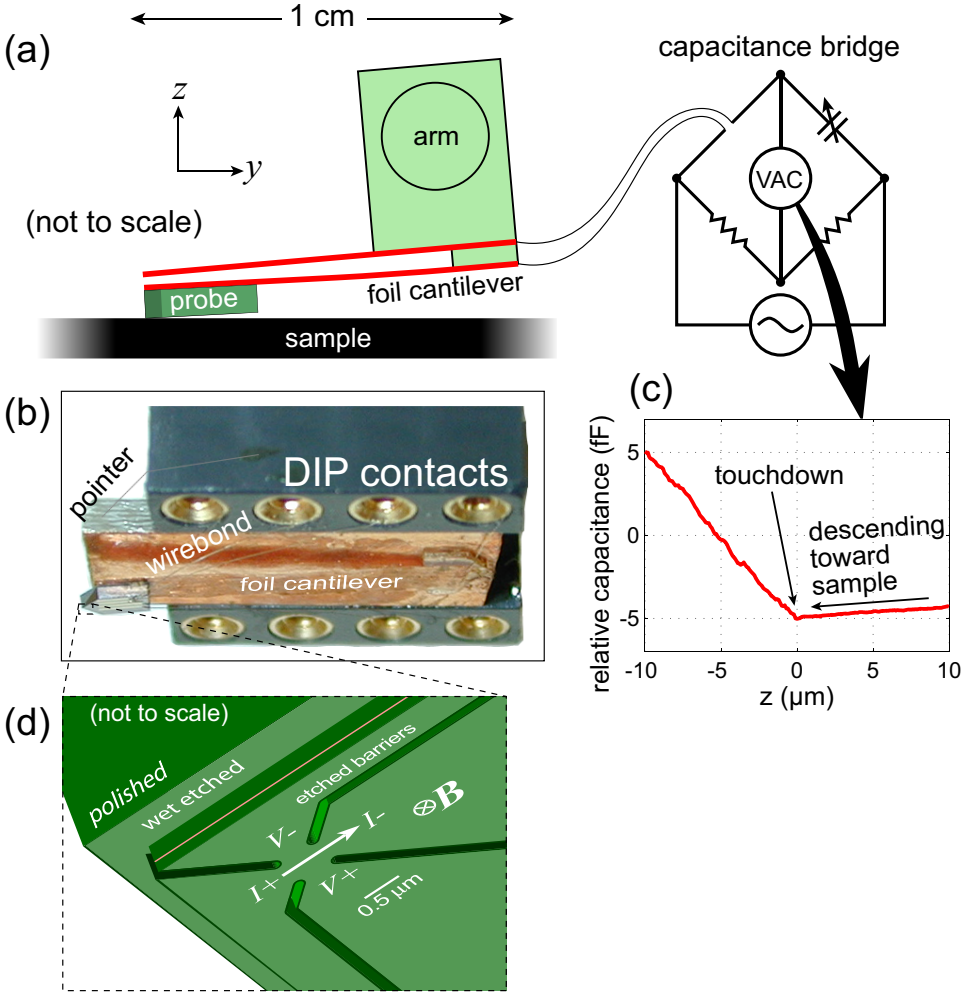

Figure 4.4: (a) Sketch of the Hall sensor mounted on a foil cantilever that, together with a fixed metal plate above it, acts as a capacitor used to sense touchdown of the sensor on the sample. (b) Photo looking up at the assembly, tilted to reveal the bottom of the assembly, which faces the sample. (c) Capacitance vs. sensor height, H, above the sample surface indicates when the sensor has touched down. For $H < 0$, capacitance abruptly starts to increase with decreasing sensor arm height. $H = 0$ is defined by this measurement with 30 nm standard deviation. (d) Sketch looking upward at the sensitive area (Hall cross) and its placement near a corner, seen before in Figure 2.2(a). As in (b) above it, the viewpoint is tilted to reveal the sensor's bottom face.

obtain higher resolution images, however, I must minimize the height of the Hall cross above the sample. To this end, the arm descends 10 μm below the position at which the sensor first touches the sample, then holds the z position fixed for each scan line, lifting above the sample plane between lines and descending again at the start of each line. The extra 10 μm causes the cantilever to apply a small downward force, ensuring that the sensor corner remains in contact with the sample throughout each line. This "contact mode" wears down the sensor (as visible in SEMs, not shown) over several hundred two-dimensional scans (several meters of linear movement), but this rate is sufficiently gradual that I do not take any precautionary measures against it (such as coating the sensor with a protective layer).

In contact mode, the height of the sensitive area above the sample surface increases with the tilt of the sensor and is proportional to the distance from the sensitive area to the corner that touches the sample, as discussed quantitatively in Section 5.4. Photolithographic patterning, followed by wet etching to remove several microns of material, defines the corner closest to the cross as shown in Figure 4.4(d). The part of the substrate that protrudes past the etched edges is then manually polished to within 20 μm of the edges so as not to interfere with the corner touching the sample.

The sensor tilt is measured optically by viewing the sensor via the mirror wedges. Tilt about the x axis is manually adjustable over a 10° range via a rotating connection between the arm and the motion stage even when the cryostat is evacuated and cold. The y tilt is adjustable via the connection between the end of the arm and the sensor dual inline pin (DIP) socket only when the cryostat is open.

Optical access to the sample stage from above is also useful for positioning the Hall sensor near a sample feature in x and y. However, when the sensor is directly over a feature, the feature is obscured. Instead, a small segment of wire (12 μm in diameter and several mm long) attached to the side of the DIP socket on which the sensor is mounted serves as a pointer, labeled in Figure 4.4(b), and the relative x and y distances between the pointer tip and the sensor active area

have been calibrated to within 20 μm. Between optical alignment and capacitive touchdown sensing, I can align to sample features in all three dimensions in a matter of a few minutes.

4.5 Cryogenic design and performance

Liquid helium or liquid nitrogen flows from a transfer dewar into the cryostat and through a high-impedance heat exchanger that cools the 5.4×5.4 cm copper sample stage. The cryogen then flows through a second heat exchanger connected to the surrounding radiation shield with cooled infrared-blocking window. The sample stage and radiation shield are enclosed in a vacuum chamber with a second window. Before cooling, the chamber is evacuated for at least an hour by a turbo pumping system to below 10^{-5} Torr. Within the first minute of cooling, the system cryopumps to the 10^{-7} Torr range, at which point the pump is typically valved off and powered down to reduce vibrational and electrical noise.

Figure 4.5 logs a cooldown using liquid helium. The base temperature of the sample stage, as read by a calibrated silicon diode thermometer heatsunk to one corner, is 4.20 K, or 3.52 K when pumping on the vapor outlet.* The radiation shield temperature, determined by a calibrated Cernox thermometer, reaches a minimum of around 20 K, varying with the helium flow rate. With its small thermal mass, the sample stage cools from room temperature to 4 K in less than 10 minutes, consuming only a couple liters of helium. Operation requires about a liter per hour thereafter. Temperature control of the sample stage from 4 to 300 K with 5 mK stability is achieved with a 50 Ω, 50 watt max resistive heater, and by restricting the cryogen flow with a manual valve integrated into the transfer line.

Warming the cryostat from 4 K to room temperature takes several hours under vacuum with the sample stage heater set (conservatively) to output a few watts. Thus the total turn-around time for switching samples is at least four hours: After warming, unloading and loading samples takes only a few minutes, but the

*The pump was an XDS5 dry scroll pump manufactured by BOC Edwards, http://www.bocedwards.com.

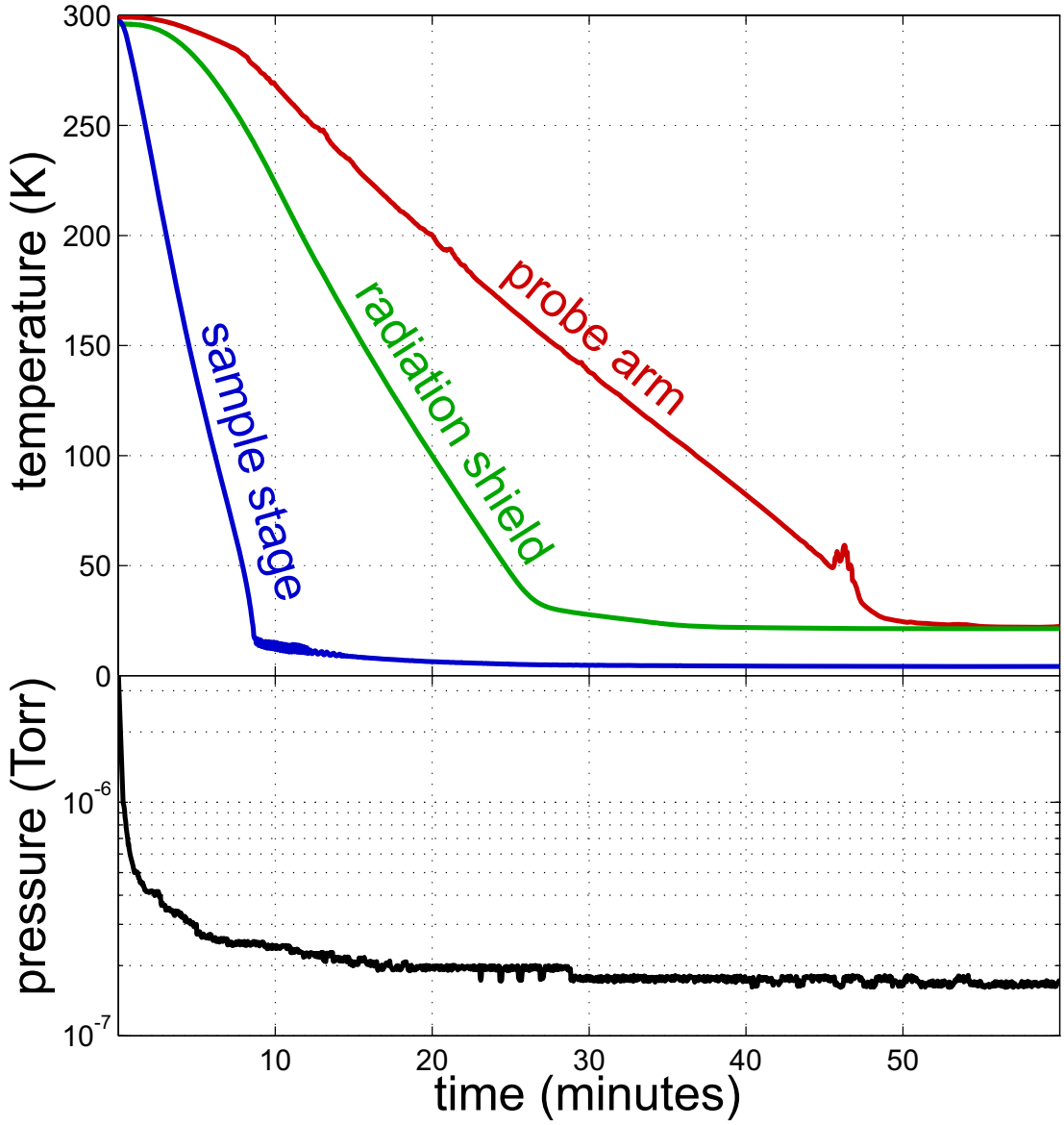

Figure 4.5: Temperatures and pressure after insertion of the precooled liquid helium transfer line into the cryostat. The sample stage cools from room temperature to near its final temperature of 4 K in less than 10 minutes. Other parts of the cryostat take longer to equilibrate.

cryostat must then be evacuated for an hour and cooled again.

Sample heatsinking

With the sample and its electrical leads in vacuum, rather than liquid or vapor, and the short distances afforded by the compact flow cryostat, heatsinking is more challenging than in a traditional dewar. Eight electrical leads run from feedthroughs in the room temperature vacuum chamber to the sample. Four of the leads are 0.13 mm diameter Manganin resistance wire with a resistance of 50 Ω each at low temperature, maintaining a high thermal resistance between room temperature and the sample. These are not suitable, however, for carrying the ampere-level currents necessary for superconducting transport studies. So the other four leads are 0.10 mm diameter copper with resistances of 0.3 Ω at low temperature.

All leads are heatsunk to the radiation shield and then to the sample stage. The Manganin leads share one pair of heatsinks; the copper leads another. Each heatsink is made by wrapping and varnishing 10 cm of wire around a copper bobbin which is bolted to the stage or radiation shield. In addition, 10 cm of wire separate each connection from vacuum feedthrough to radiation shield to sample stage. The sample end of each lead terminates in a pin-and-socket connection to 4 cm of 0.10 mm diameter copper wire which is soldered to a gold pad on a beryllium-oxide heat sink chip varnished to the sample chuck. A 25 μm diameter aluminum wirebond (or several, for leads that will carry more than 200 mA) connects each pad to a gold pad deposited on the sample. The sample substrate is also varnished to the sample chuck, and most of the sample cooling flows through the substrate rather than the wires.

As a calibration of sample temperature, I use the superconducting transition of a thin film of niobium deposited on a 400 μm thick oxidized silicon substrate. This film forms the coil used to apply field in a SQUID susceptometer. I measure its T_c to be 8.73 K (by maximum dR/dT) in a commercial cryostat (the LAM PPMS), as shown in Figure 4.6(a), where the temperature is ramped through the transition and back 13 times. (It appears the transition actually consists of two

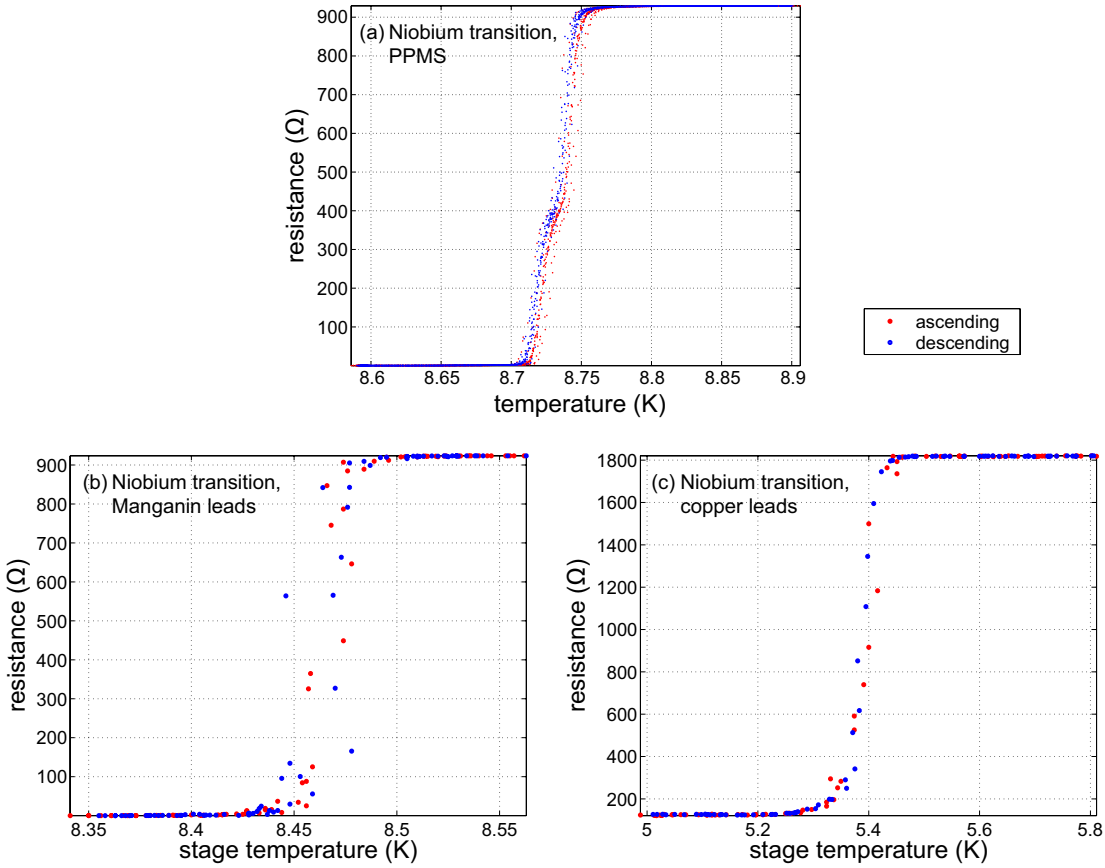

Figure 4.6: Transition temperature of a niobium film measured in several configurations to test for heat leaks: (a) In the PPMS, vapor-cooled. (b) In the scanner cryostat, in vacuum, with four Manganin leads. (c) In the scanner, with two copper leads.

transitions, i.e. two parts of the sample went superconducting at slightly different temperatures, which I average to obtain 8.73 K.) In the PPMS, the sample and leads are cooled by helium vapor, and thus more likely to be in equilibrium with the thermometer. In the scanner cryostat in vacuum, the same film shows a transition at 8.47 K, as measured with the sample stage thermometer, in a four-point resistance measurement with Manganin leads, shown in Figure 4.6(b). In a two-point configuration with copper leads, however, its transition is reduced to 5.39 K on the stage thermometer, plotted in Figure 4.6(c).

Transition temperatures for several samples of YBCO are found to be within a few degrees of their expected values even with copper leads. Thus I expect that the actual sample temperature is a fraction of a degree higher than the thermometer temperature for high resistance leads, and up to several degrees higher where it is necessary to use low resistance current leads.

Sensor heatsinking

The sensor arm is made of fiberglass and surrounded by a copper sheath that is heatsunk to the radiation shield. At the end of the arm inside the cryostat is a copper section, cooled via a 1.6 mm diameter copper braid sunk to the sample stage. For temperature control independent of the sample stage, the end of the sensor arm contains a 100 Ω platinum resistive thermometer using a standard calibration curve (i.e. not individually calibrated), and a 200 Ω, 12.5 watt max heater. Figure 4.5 shows that the copper braid couples the arm and sample stage relatively weakly; the arm cooling rate is slower and the base temperature is about 15 degrees higher. This isolation is convenient for maintaining a constant arm temperature while changing the sample temperature, but is not necessary for the measurements below.

The leads of the Hall sensor start from the room temperature cryostat feed-throughs with 15 cm of ultra miniature coaxial cable consisting of a 0.20 mm diameter copper center conductor and stainless steel braided shield insulated by Teflon. These are soldered to 10 cm of 0.13 mm diameter phosphor-bronze wire

that is varnished onto the temperature-controlled copper section of the arm. Finally, 8 cm of 0.26 mm diameter copper wire is soldered to each lead, wrapped and varnished onto the copper arm section, and terminates at a DIP socket from which the sensor assembly hangs, facing down toward sample. Cooling of the sensor occurs primarily through the leads, so the 8 cm sections of copper wires serve to reduce the time constant for equilibration, and to help remove heat generated in the sensor itself. Comparison of the sensor resistance to the arm thermometer during cooling and warming indicates that the sensor follows the thermometer with a characteristic lag of less then five minutes.

4.6 Vibration

Vibration of the sensor relative to the sample can blur or introduce artifacts into a scanned probe image. My instrument is not specifically designed to minimize vibrations. It is isolated by rubber feet from an ordinary lab bench on a basement floor. The sensor hangs from a floppy cantilever attached to a long arm. However, for high resolution images, the sensor touches the sample, coupling the two via static friction. The field is measured only when the sensor is held fixed at each pixel. I quantify vibrations in this configuration as follows.

I scan to find a position with a high magnetic field gradient* that will translate sensor movement into measurable field variation, and hold the sensor at that position, applying a DC Hall current. The Hall voltage time trace is then recorded at 20 kilosamples/second for 50 seconds. For comparison, a time trace is recorded with the sensor retracted several hundred microns from the sample, where the gradient is much smaller. I find a statistically significant increase in noise at the position of high gradient. This extra noise is consistent with 30 nm rms movement in x, 40 nm rms movement in y, or 60 nm rms movement in z. The actual

*Two positions with large gradients in the Hall voltage in different directions were examined. At the first, dV/dx was -85 μV/μm, dV/dy was -45, and dV/dz was -33. At the second, dV/dx was -39, dV/dy, 34, and dV/dz, -1.2 μV/μm. These gradients may have been due to an electrical interaction between sample and sensor, rather than magnetic vortices. They were, however, approximately constant over a 600 nm diameter and reproducible between scans before and after the vibration measurement.

movement is probably a combination of smaller movements along multiple axes. The blurring effect that such movement might cause, however, is still 20 times smaller than that caused by the Hall probe, as quantified in Chapter 5.

4.7 Possible design permutations

4.7.1 Other scanned probes including scanning SQUID

Other probes with unique advantages could be substituted for the Hall sensor. For example, studies of dissipation in superconductors would benefit from electric potential imaging, which could be achieved with a conducting tip. The tip could even be integrated into a Hall sensor for correlated electric and magnetic measurements.

A SQUID could be substituted for its superior field sensitivity, $\sim 10^{-7}$ G/$\sqrt{\text{Hz}}$, albeit at some cost in spatial resolution, 10 μm [Kirtley et al., 1995]. An important consideration for using a SQUID in my instrument is temperature control. The SQUID must be held below its critical temperature; in the present configuration, the sensor arm is cooled via the sample stage and cannot be maintained colder than the sample. Thus the sample would have to remain below about 9 K for a niobium SQUID or 90 K for a high-T_c SQUID. To circumvent this restriction, I could place the SQUID on the sample stage, and scan the sample using the arm. A niobium SQUID has been used successfully in a similar configuration with sample temperatures up to 150 K [Kirtley et al., 1999]. The SQUID could be mounted on a bracket that holds it above the sample with the sample facing up so as not to obscure optical alignment of the sensor to sample features.

4.7.2 Applied magnetic field

The system does not have a built-in magnet for applying a field to the sample. Desert Cryogenics incorporates superconducting, solenoidal magnets into similar cryostats, achieving 1 T with approximately 60 A applied current. The liquid helium flow is split to cool the magnet and sample stage separately.

For fields below about 0.1 T, nonsuperconducting coils could be placed outside the cryostat. An iron flux guide that wraps around the cryostat would enhance the coils' field by providing a high-permeability return for the flux. The flux guide also allows more flexible placement of the coils. Furthermore, the guide can terminate in pole pieces brought close to the sample and shaped to further concentrate the field while maintaining field homogeneity at the sample.*

4.7.3 Motion stage improvements

Temperature controlling the positioning stage might eliminate the 2 μm drift observed between successive images taken at nominally identical positions, mentioned in Section 7.3. It may also reduce deviations in the y axis positions between scan lines. The stage would be maintained slightly above room temperature via a thermally insulating enclosure, thermocouples, resistive heaters, and feedback electronics.

My current design, in which the positioning stage is external to the vacuum chamber, has the advantage that the motors, gears, screws, and associated lubricants need not be vacuum-compatible. Vacuum-compatible substitutes are, however, commercially available.† If the stage were inside an extension of the vacuum chamber, it would not need to overcome the forces of atmospheric pressure and bending bellows. The y range would improve, and the y axis scaling, discussed in Section 5.4, would likely be eliminated. More generally, reduced torque on the stage would mean less disparity between movements of the stage and movements of the end of the sensor arm. Adding optical linear position encoders for closed-loop positioning would likely be more effective than in the current configuration.

In vacuum but at room temperature and in the absence of large forces, piezo-based actuators could substitute for the stepper motors. Piezos can generate long

*Such a magnet was designed and built into a Desert Cryogenics probe station by Dr. Douwe Monsma in Professor Charles Marcus's lab at Harvard University.

†See, for example, vacuum-compatible stepper motors from tectra GmbH Physikalische Instrumente, http://www.tectra.de, or servo motors from Aerotech, Inc., http://www.aerotech.com

range motion through a series of short steps. Implementations include "stick-slip" (inertial) motion* and "inchworm" behavior.† Typically the step size is not repeatable enough to be used directly for scanning, but optical linear encoders allow closed-loop positioning with 20 nm accuracy, which would be suitable for SHPM.

Temperature drift of the stage in vacuum (even with some contact to a base) would be larger in the absence of temperature feedback, but once implemented, feedback would be more precise.

*For example, Physik Instrumente (PI) GmbH & Co. KG, http://www.pi.ws, makes closed-loop, stick-slip piezo actuators.

†See EXFO Burleigh Products Group Inc.'s Inchworm® motors, http://www.exfo.com, or Bookham Inc. New Focus division's Picomotors™, http://www.newfocus.com.

Chapter 5

Determining resolution with vortex images

5.1 Introduction

Ultimately, Abrikosov vortices produced the best images with which to calibrate the microscope's resolution. I could not see vortices, however, until I overcame hurdles already encountered in Chapter 3: reducing the sensor-sample separation and circumventing the sensor's low-frequency noise.

5.2 Current-carrying wire

During my initial efforts, a current-carrying loop served as an easy target. The loop is patterned out of a niobium film, and is designed to apply field to a SQUID susceptometer. As indicated in Figure 5.1(a), I apply a current to the loop that alternates between two dc values, ±15 mA (a 0.5 Hz square wave generated with a Keithley 228A current source). To obtain the scanning Hall probe image 5.1(b), I pause at each pixel and measure B_z for both currents, then plot the difference divided by two. This lock-in technique suppresses noise away from 0.5 Hz.

I obtain Figure 5.1(b) using a 3 μm Hall sensor fabricated by Clifford Hicks. This sensor did not have a microfabricated (wet etched) corner, described for other

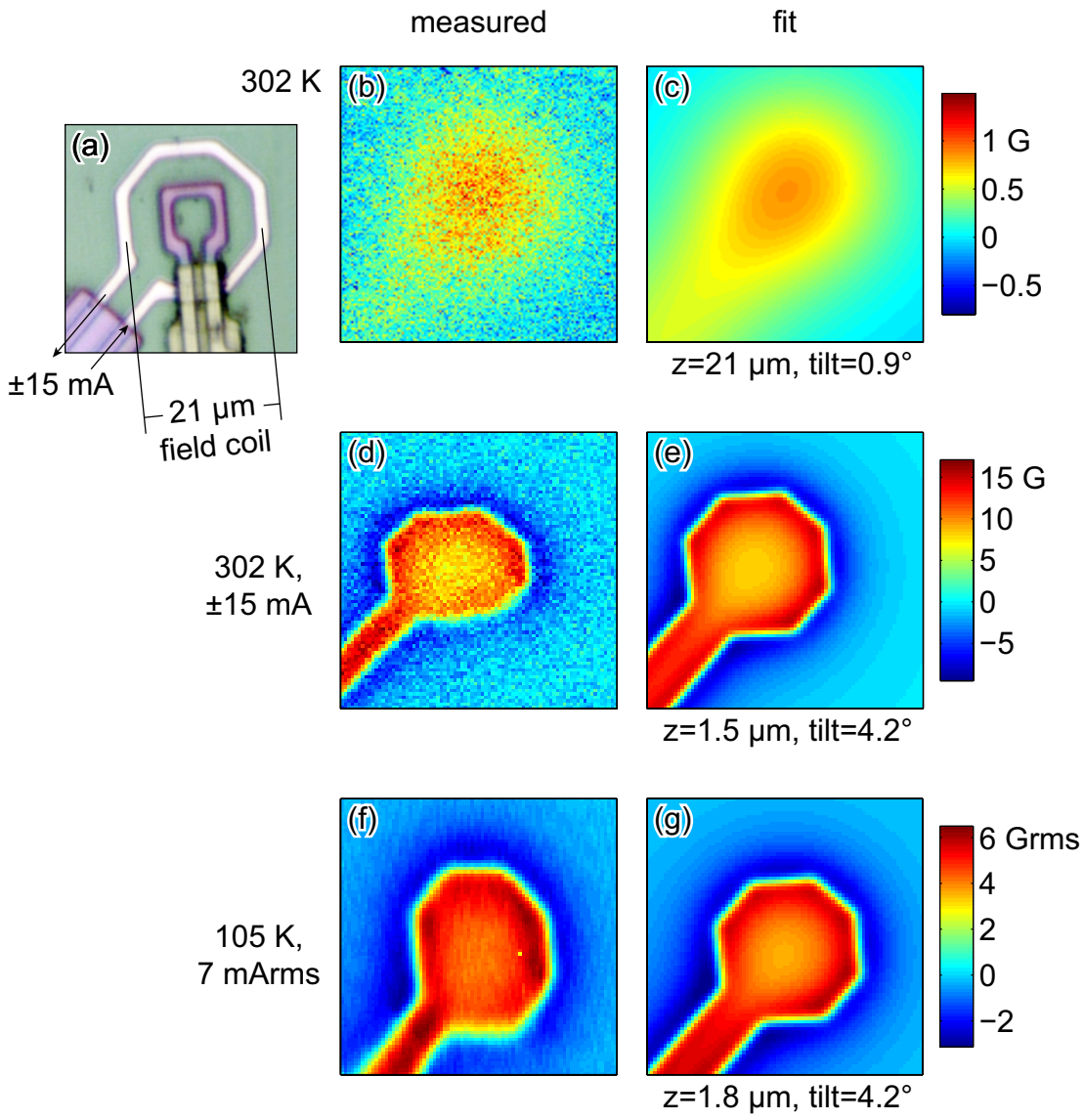

Figure 5.1: (a) Optical micrograph of the field coil (and pickup loop, not used) of a niobium SQUID susceptometer, indicating the length scale of the other images. A current is applied to the coil and B_z is measured above its surface in (b), (d), and (f). (c), (e), and (g) are corresponding calculations of the expected field, fit to the data. The temperatures listed are those of the Hall sensor.

sensors in Section 2.3, but I did mechanically polish a corner near the sensitive area. Apparently, however, it was not near enough, as the sensitive area remained 21 μm above the surface according to the fit, Figure 5.1(c). The fits calculate the field above an infinitesimally thin, octagonal loop, Gaussian-averaged over the nominal sensor area.*

By switching to a sensor with a microfabricated corner and a 500 nm sensitive area (Janice's sensor 26, described in Section 2.3), I obtain the much improved Figure 5.1(d), with a fitted height of 1.5 μm. This image does, however, show scaling along the y axis, even without the cryostat evacuated. Finally, Figure 5.1(f) shows that I can further reduce noise by going to lower temperature (the temperatures listed are those of the Hall sensor) and using a more proper lock-in technique with 146 Hz sinusoidal sample current and 20 μA dc Hall sensor current. In this instance, with the cryostat evacuated and cold, I see that the y axis is scaled up (i.e. the arm is not moving as far in y as I calculate from the motor movement), which was typical of later scans, as described in Section 5.4.

5.3 Vortex imaging

With improved height and noise, guided by the loop imaging, I could move on to imaging individual Abrikosov vortices in a YBCO film, which serve as spatially sharp magnetic objects that test the scanner's mechanical performance. The magnetic field of vortices in such a film is well modeled [Pearl, 1966; Chang et al., 1992b; Carneiro and Brandt, 2000].

For this experiment, a 5×5 mm square piece of YBCO is varnished to the sample stage as shown in Figure 5.2(a). This YBCO is a piece of the same 300 nm thick film described in Section 3.2, but is left unpatterned. The sample is cooled in the lab's ambient field of about an Oersted; the cryostat has no magnetic shielding. The sensor temperature is controlled at 30 K, and the sample temperature is uncontrolled, ranging from 11.9 to 12.3 K.

*It is easy enough, though, to model the finite width of the loop's segments, carrying a uniform current density. See my routine `Bz_of_sheet_segments.m`.

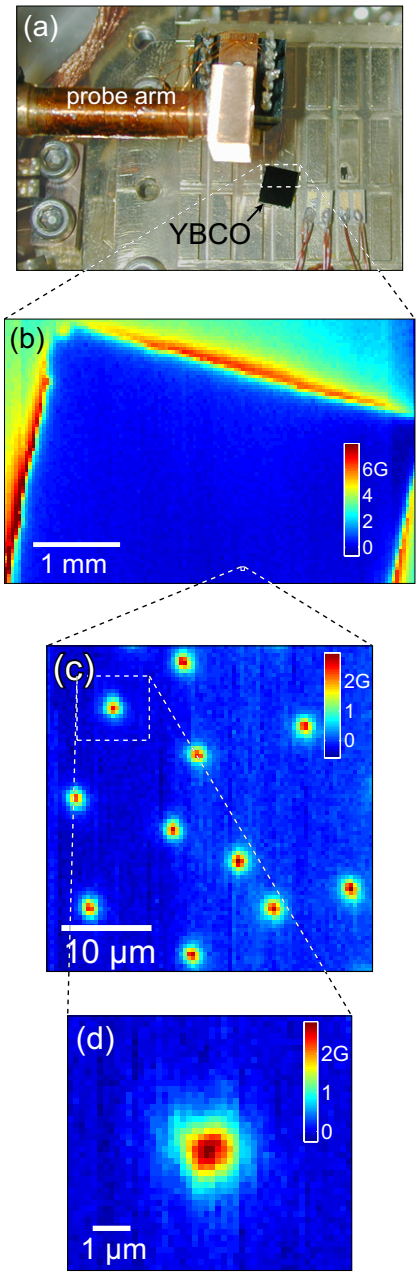

Figure 5.2: (a) Top view photograph of a square section of a thin film of YBCO varnished to the sample stage. (b–d) Magnetic images of the square at several length scales, from its full width down to submicron resolution. Each white dashed box in (a–c) indicates the area scanned in the succeeding image. The pixel spacing in (d) is 200 nm.

After cooling, a field with a positive component of several Oersted in the vertical direction is applied by placing a permanent magnet on top of the cryostat. The area indicated by the white dashed rectangle in Figure 5.2(a) is then scanned, moving the sensor in a plane 40 μm above and parallel to the sample surface. A 146 Hz, 24 μArms current is applied to the sensor and the in-phase component of Hall voltage is measured with a lock-in amplifier.

The resultant image is shown in Figure 5.2(b). The sample generates screening currents in response to the applied field, enhancing the field just outside its edges. The small white square near the bottom of this image indicates the area scanned in Figure 5.2(c), now with the corner of the sensor continuously touching the sample during measurement, retracting several microns between scan lines. With pixel spacing reduced to 500 nm and apparent field noise of 0.1 G rms, individual vortices are clearly visible. Figure 5.2(d), with 200 nm pixel spacing, resolves the apparent shape of the upper left vortex.

5.4 Limits on mechanical aberrations

On a successive cooldown, after more carefully aligning the sensor to reduce its tilt, single rows of points near a vortex are scanned first along the y, then the x directions, shown in Figure 5.3(a)–(b). Both scans are well modeled by the field of an Abrikosov vortex in a YBCO film, depicted in (c). The model uses the sample's known thickness (d=300 nm) and bulk penetration depth (λ=180 nm at 12 K [Djordjevic et al., 2002]). Because the coherence length is much smaller than the penetration depth, the vortex core is negligible and the London equations govern the field inside the superconductor. The z component of magnetic field above the film is calculated to be [Chang et al., 1992b]

$$B_z(r,z) = \frac{\Phi_0}{2\pi\lambda^2}\int_0^\infty \mathrm{d}\gamma \frac{J_0(\gamma r)e^{-\gamma z}}{\tau\cdot(\coth(\tau d/2)+\tau/\gamma)} \quad , \qquad \tau \equiv \sqrt{\gamma^2+\lambda^{-2}} \tag{5.1}$$

where $\Phi_0 = 20.7$ G$\cdot\mu$m^2 is the magnetic flux quantum and J_0 is the zeroth-order Bessel function of the first kind. $r = \sqrt{(x-x_0)^2+[(y-y_0)\cdot A]^2}$ is the

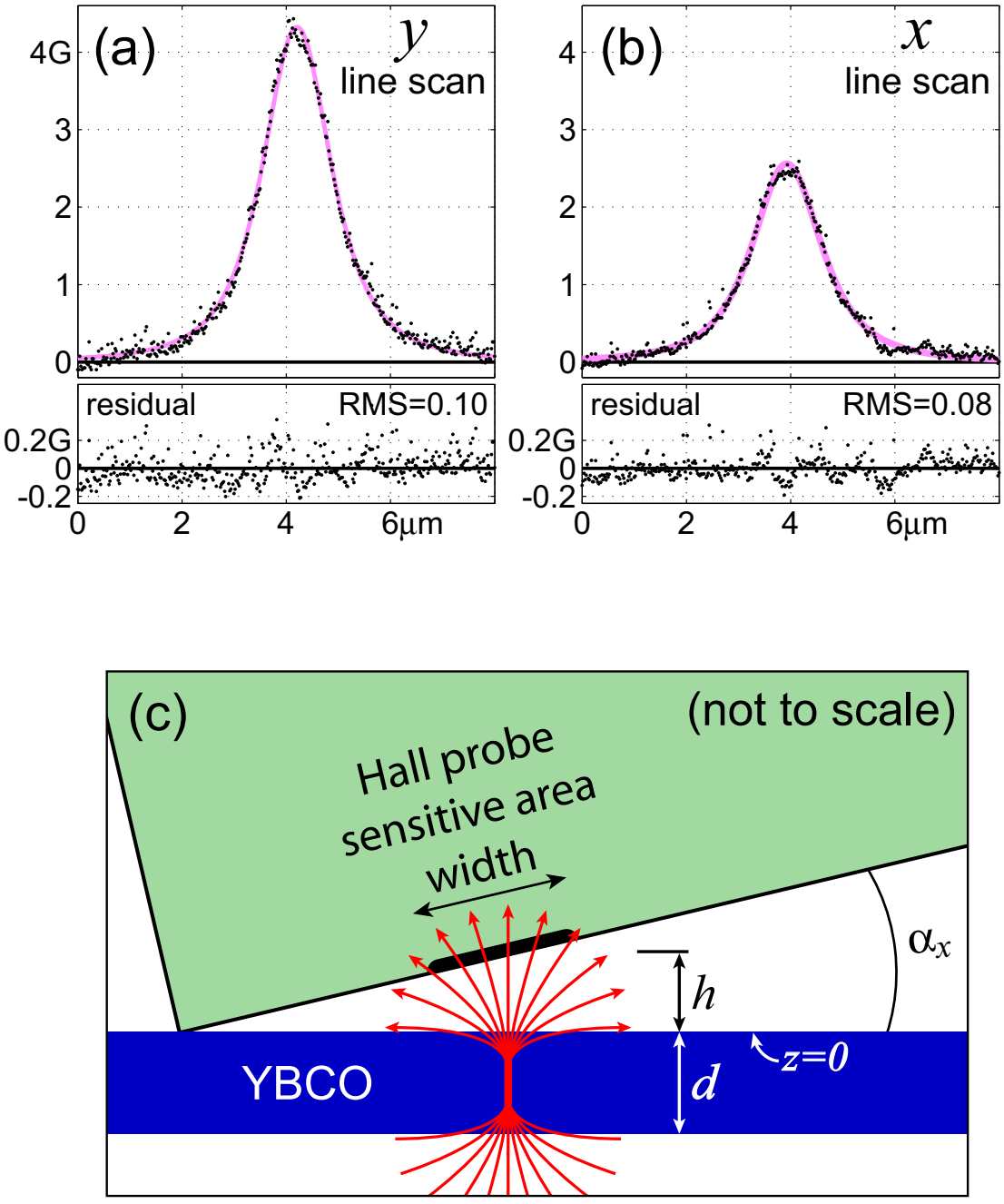

Figure 5.3: (a)–(b) Single rows of points near a vortex were scanned, along the y, then x directions. These data (black points) were fit (pink lines) with a model of the vortex field, depicted in (c). Note the the scans' amplitudes differ because they (inadvertently) pass by the vortex center at different distances.

radial distance from the center, (x_0, y_0), of the vortex; the y axis is scaled by an empirical factor A. z is the height above the top surface of the film. The fit calculates the Hall signal as B_z averaged over the Hall probe's sensitive area, estimated from nominal lithographic dimensions to be a square 500 nm on a side. The sensor also has a zero-field offset, B_{offset}, which is subtracted from the values shown.

Free parameters for the y scan are x_0 and y_0; $A = 0.87$; the height of the sensitive area, h=580 nm; and $B_{\text{offset}} = -84.0$ G. The Hall coefficient is calibrated to be 0.112 Ω/G. Thus the height and size of the sensitive area are each larger than the penetration depth, and are the most important parameters for the apparent size of the vortex.

The sensor is tilted about the x axis by α_x from horizontal so that only the corner near the sensitive area will come into contact with the flat surface of the sample. α_x is determined optically to be $1.7 \pm 1.0°$. This tilt could add to the measured signal up to 5% of the lateral component of field, which is insignificant in this model. More importantly, α_x determines h. The corner lies about 10 μm in front of the sensitive area, limited by the accuracy of photolithographic alignment across many sensors fabricated on one chip. Due to this distance and the tilt, the sensitive area is lifted above the surface when the corner rests on the surface. Because of uncertainty in the tilt, I took h as a free parameter.

The choice of allowing the y axis scaling to vary as a free parameter is motivated by other images taken with this instrument of lithographically defined structures that show that the y axis movement of the sensor is smaller than expected from the motor movement and gearing. When the scale is fixed at $A = 1$, the residual shows structure symmetric around the vortex center consistent with a scaling error. The physical origin of this disparity between calculated and actual sensor movement is likely due to position-dependent tilting of the sensor arm. The force exerted on the motion stage by the vacuum and the bellows changes direction as the stage moves along the y axis, rotating the stage and arm slightly.

To first order, this rotation moves the sensor in the y and possibly z directions on top of its intended movement; the x axis is relatively unaffected. The x scan

is fit with the same fixed parameters of Hall coefficient, sensor dimensions, tilt, and sample penetration depth, but the movement scaling is fixed at the expected value, which did not result in systematic variation in the residual. h is found to be 550 nm and B_{offset}=-85.3 G. The B peak is smaller than in the y scan because the x scan was inadvertently taken 600 nm off the vortex center.

The root-mean-square of the residuals in Figure 5.3(a)–(b) is consistent with the 0.11 G rms noise measured in the sensor when it was retracted from the sample and held in a fixed position immediately after the scan (measured with the same bandwidth as when scanning). From this I can place an upper bound of 50 nm rms on the deviation of the sensor position from its expected values within one scan line; less noise or sharper features are required to set a lower bound.

However, Figure 5.2(d) shows some evidence that the position repeatability between lines (scanned in the y direction) is not this good. Fitting successive lines separately, the center position of the vortex appears to vary by 200 nm rms, almost all of which must be explained by deviations in the sensor y position between scan lines, rather than by B noise. I also have less systematic evidence of micron-scale position drift over the course of hours when I perform repeated scans of a (presumably stationary) vortex. Such drift plausibly results from thermal expansion of the external stage or other components whose temperatures are not controlled.

These estimates—less than 50 nm rms positional error between points within a line and 200 nm rms error between lines within an image—demonstrate that microstepping and gear reduction can successfully reduce step size, which limited a previous instrument [Gregory et al., 2002]. In my case, the combination of height and size of the Hall probe's sensitive area, rather than any aspect of the stepper motor scanning stage performance, produce the most significant blurring of features.

Minimizing the sensor tilt about the x axis, α_x, minimizes the height, but is limited by two factors that can prevent the corner near the sensitive area from touching the sample. First, the wirebonds, which protrude downward from the opposite end of the sensor's lower surface, must remain lifted off the sample

surface. Second, any inaccuracy in zeroing the tilt about the y axis, α_y, together with a small α_x, can lead to one of the side corners of the sensor touching before the tip. Thus the usual alignment procedure entails zeroing α_y visually at room temperature, then imaging vortices at low temperature, modeling the images to determine the height of the sensitive area, and adjusting α_x to minimize this height.

The heights I calculate from fits to the vortex scans, 580 and 550±50 nm, are consistent with those I estimate optically, 400 ± 200 nm, from the geometry and tilt of the sensor, plus the 140 nm depth of the 2DEG. (See Section 2.2.) Thus I expect that improving the sensor fabrication in order to reduce the distance between the Hall cross and the corner, bring the 2DEG closer to the surface, and shrink the cross area, will significantly improve the instrument's resolution before limits imposed by the scanning mechanism are encountered. This effort to improve the sensors is in progress [Hicks et al., 2006].

Chapter 6

Pulsed current through YBCO on LAO: Bean fits

6.1 Experimental configuration

Having established the functionality and resolution of my scanning Hall probe microscope, I now apply it to the original problem of interest: understanding critical currents in YBCO films. I start by examining the same film used in Chapter vortex to image vortices. The sensor and data acquisition details are also the same.

The piece of the film used here is patterned into a 20 μm wide link (a bridge) using photolithography followed by argon milling to remove parts of the YBCO film. The resultant sample geometry is shown in Figure 6.1(a). I cool the film with no applied current or field, and control its temperature at 21 K; the sensor arm temperature is controlled at 28 K. The experiment consists of applying a 10 ms square current pulse to the link, then scanning one area of it afterward. I repeat this with increasing pulse amplitude, I.

By applying a pulse that returns to zero current, rather than applying a dc current while scanning, I hope to mitigate the effects of sample heating by the leads and, above the critical current, by the sample itself. As described below, it seems that I do not succeed completely. Note that I do avoid overshoots in

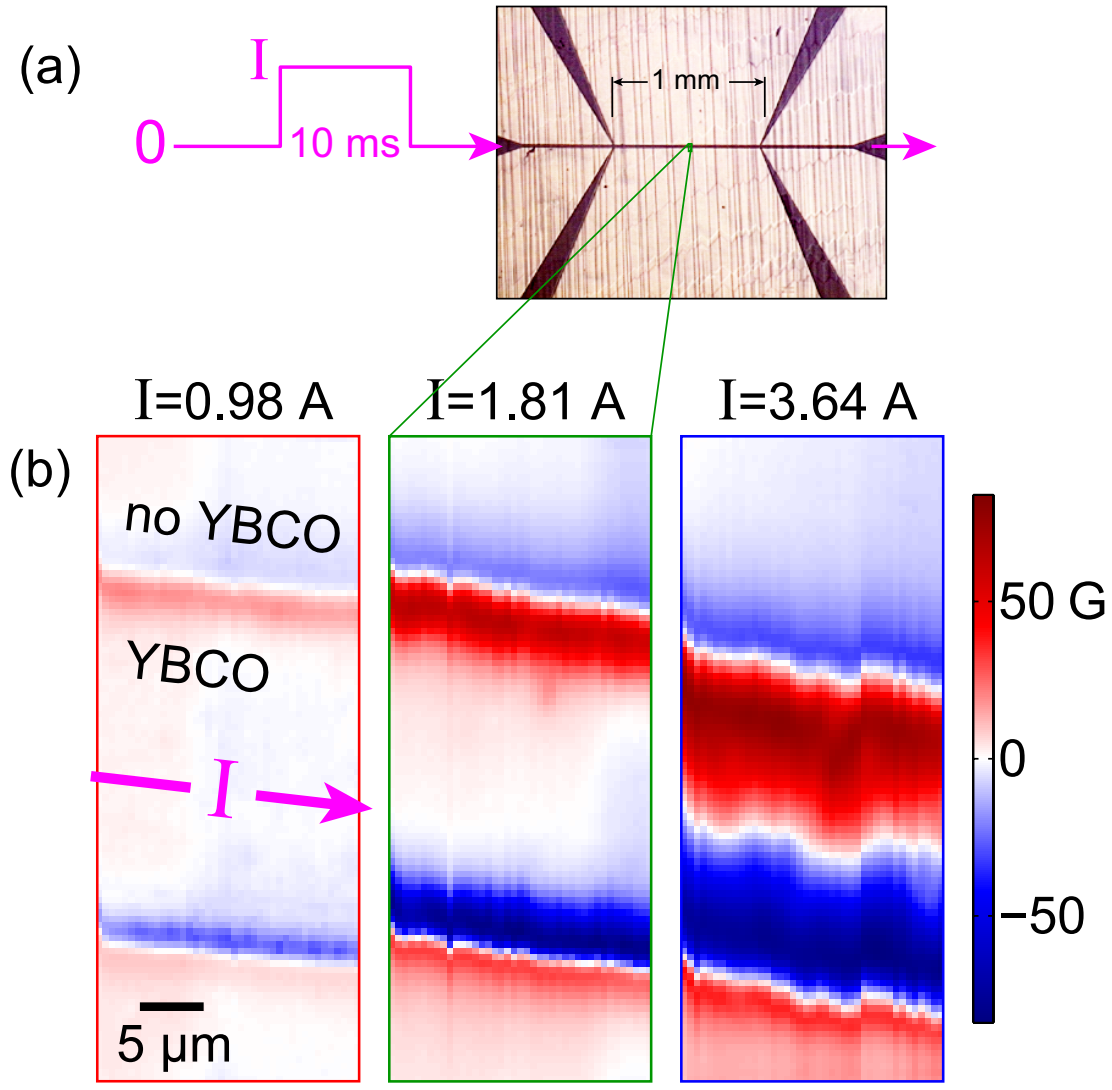

Figure 6.1: (a) A YBCO film is etched into a 20 μm by 1 mm link to which pulses of current are applied. (b) A portion of the link is imaged after applying each pulse.

the current pulse (which is important in the model used to analyze the results) by rounding the pulse edges with a tanh function of width 0.4 ms (generated digitally) and monitoring the voltage across a resistor in series with the sample on an oscilloscope.

The images are shown in Figure 6.1(b). After the lowest current, 0.98 A, is applied, vortices have already been forced into the edges of the film and remain trapped. The flux front advances with increased applied current, and has penetrated fully across the link by I=3.64 A. The flux penetration is fairly homogeneous along the length of the link, so for further analysis I consider only cuts along the y direction through the middle of each image.

6.2 Bean model for a thin strip

I model these images as the field generated by a strip, infinitely long in the x direction and infinitesimally thin in the z direction [Brandt and Indenbom, 1993]. The calculated field is compared with the data in Figure 6.2. The underlying assumption of this Bean-like, or critical state, model is that vortices depin at a current density, J_c, that is independent of position, applied field, etc. They rearrange instantly to restore the current to J_c. This is equivalent to postulating that E is zero below J_c and infinite above.

An example of the current and vortex density profiles resulting from this model is shown in Figure 6.3. After the applied current is ramped up from zero, the pink curves apply. The strip has reached J_c in regions at its edges, causing vortices to enter. The middle region remains vortex-free, but carries a Meissner current due to the demagnetization factor of this thin-film geometry. When the current is returned to zero, current and vortices of the opposite sign are superposed on the original solution, leading to the black curves.

To compare with my measurements, I calculate a current density profile, as in Figure 6.3, then use the Biot-Savart law, numerically integrating to find the resultant field in a plane above the surface of the strip. This model admits various free parameters, listed in Table 6.1, which I fit to the data. Several parameters

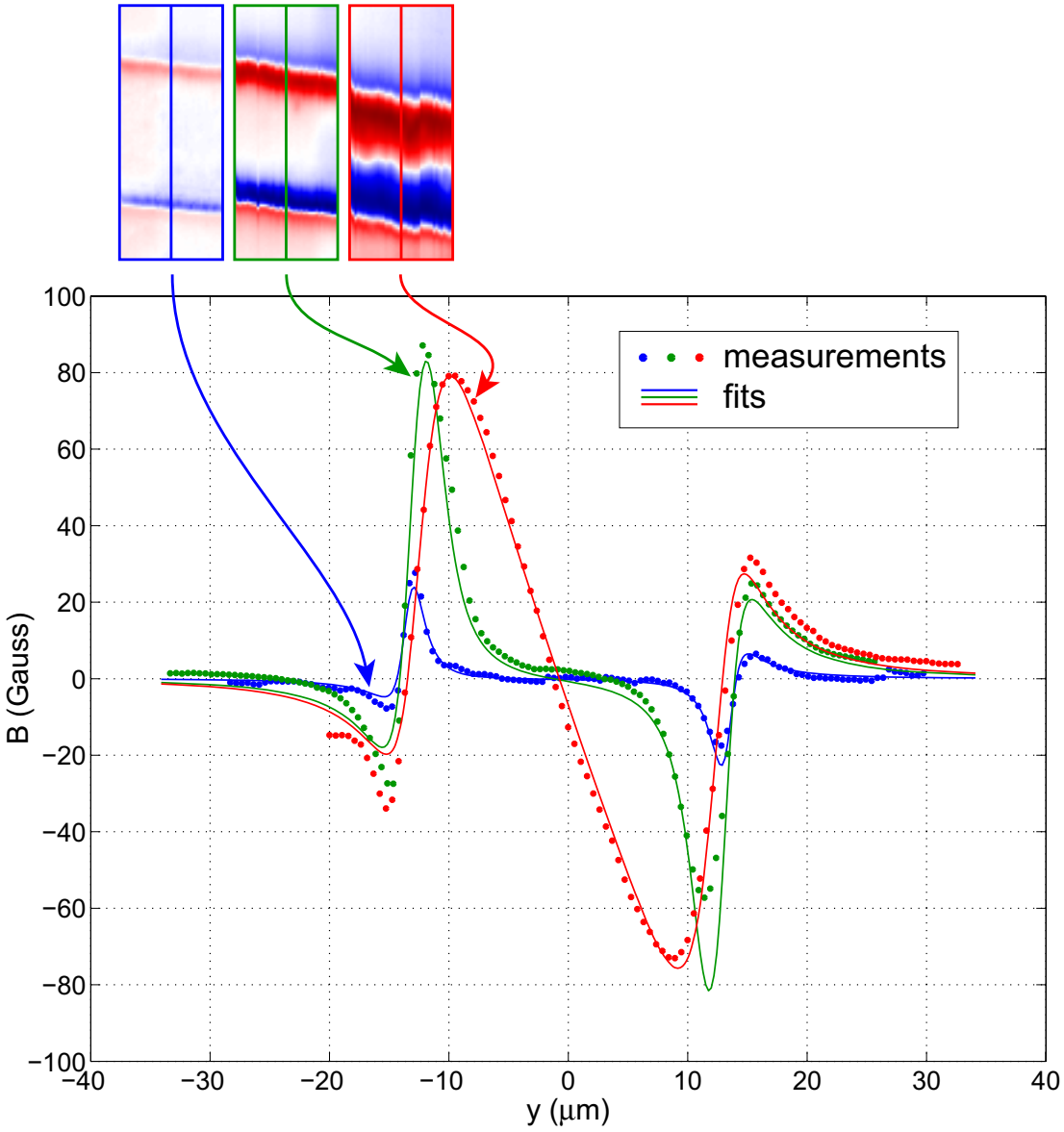

Figure 6.2: Bean model fits to y cuts through the pulsed current images from Figure 6.1.

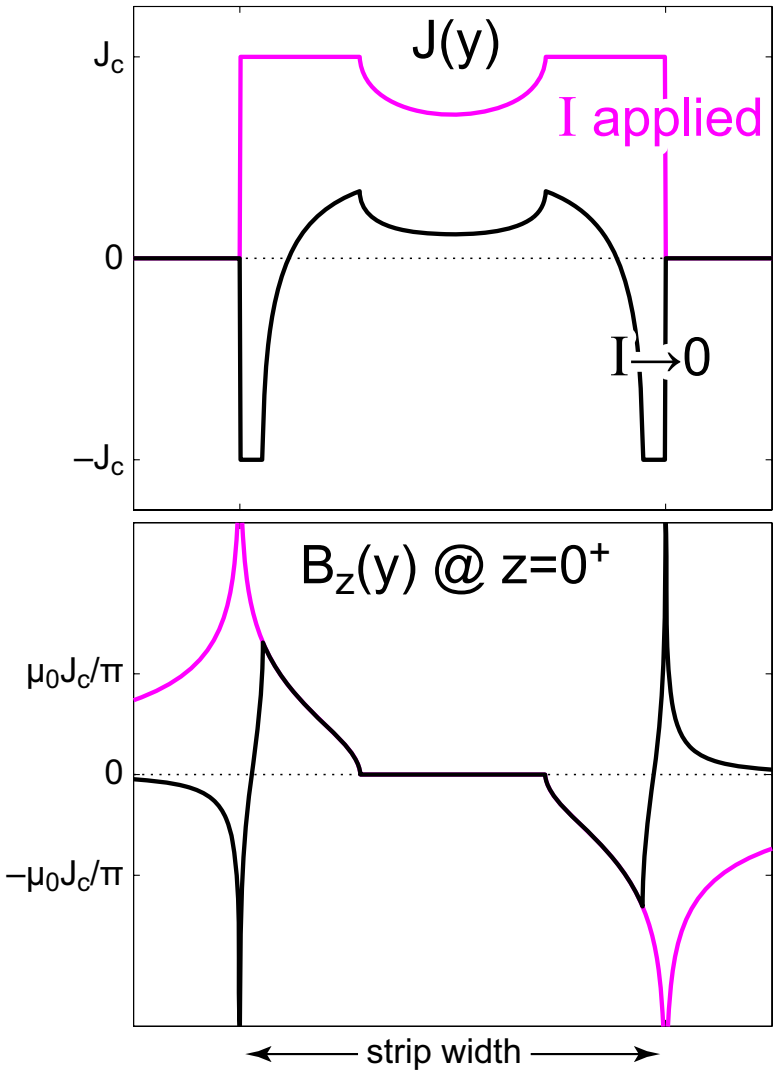

Figure 6.3: An example of the underlying current distribution calculated using the Bean model, and the calculated magnetic field at the surface of the strip, which dictates the vortex density.

I (A)	I_c (A)	h (μm)	y center (μm)	strip width (μm)	sensor tilt
0.98	2.82	1.34	−0.7	28.2	5.9°
1.81	2.89	1.84	3.9	27.7	2.6°
3.64	1.05	1.98	−6.0	25.9	6.6°

Table 6.1: Parameters used for the Bean model fits shown in Figure 6.2.

address aspects of the geometry that are not precisely known: The location of the strip in y, the height, h, of the image plane, the width of the strip (which helps allow for y scaling of the cut relative to an ideal cross section due to tilt of the sample or inaccuracy of the rate of scanner movement), and the tilt of the sensor, which determines the component of field measured (predominantly B_z with some B_y). Perhaps the most interesting free parameter, however, is the critical current of the strip, I_c, (or equivalently the critical current density, J_c). The measured applied current is a fixed parameter.

6.3 Implications of the fit values

The fits are revealing. They suggest that the model is qualitatively accurate, capturing the peaks, dips, and general shape of the data. Looking at the fit parameters, the first two critical currents are reasonably consistent and high compared to the third. Furthermore, the third applied current pulse exceeded those first two I_c values. Plausibly, then, dissipation heated the sample during the third pulse, lowering I_c (by a factor of 2.7!).

Heating may also explain the deviations, as a function of x, in the y movement of the third scan. Thermal expansion of the sample stage, followed by contraction over the course of the scan, may lead to an overall shift in the sample position followed by smaller shifts between lines.

The fits, however, do not provide a complete explanation of the data. The two systematically differ in places, suggesting that the model is oversimplified. I tried

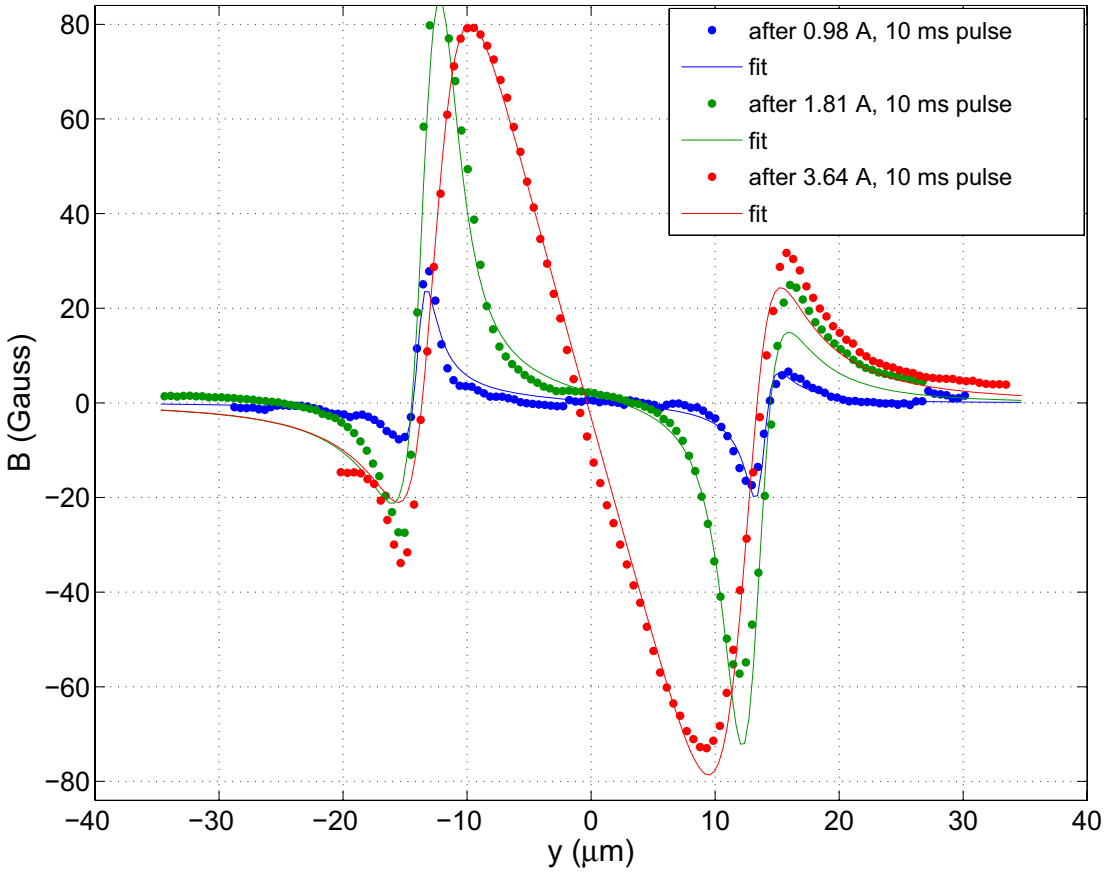

Figure 6.4: Allowing edge currents to vary as additional free parameters does not improve the fits over those of Figure 6.2.

I (A)	I_c (A)	h (μm)	y center (μm)	width (μm)	tilt	I_+	I_-
0.98	4.38	1.12	−0.7	28.3	3.3°	5.4	7.6
1.81	3.07	1.92	3.8	27.2	2.3°	4.0	16.8
3.64	1.05	2.01	−6.2	25.9	2.8°	1.1	1.0

Table 6.2: Parameters used for the Bean model fits with edge currents shown in Figure 6.4. The parameters have the same definitions as in Table 6.1, with the addition of currents I_+ at $y = +\text{width}/2$ and I_- at $y = -\text{width}/2$

adding currents at the edges of the strip (whose magnitudes vary as free parameters), which could arise from a surface barrier for vortex entry, as in Section 3.9.3. These can be thought of as a wire placed along each edge. I approximate the wires as infinitesimally thin; the current would actually be spread over a penetration depth inward from each edge ($\lambda_{\text{eff}} = \lambda_{ab}/\tanh(d/2\lambda_{ab}) = 260$ nm [Djordjevic et al., 2002; Carneiro and Brandt, 2000]). The results, shown in Figure 6.4, do not improve on the fits of Figure 6.2, though.

One can imagine a variety of explanations for the small disparities between data and fits. There may be a small applied field or field gradient inadvertently present in the experimental setup. Alternatively, the scanner movement may introduce some scaling, as in Section 5.4. In the end, these details remain uncertain, and I content myself with explaining the major features of the field profiles.

Chapter 7

Reconstructing J and E from magnetic images*

7.1 Introduction

Chapter 6 examines a strip of YBCO for which the current-induced penetration is sufficiently uniform that it can be modeled with a constant pinning force. Figure 7.2(c)–(j) illustrates that this is not always the case. These magnetic images of another strip reveal significant inhomogeneities that immediately violate that model. I therefore abandon the "bottom-up" approach—positing a model from which I derive quantities of interest such as current density in the film. Instead, I find methods of extracting these quantities directly from the magnetic images.

First, one can invert the Biot-Savart law to reconstruct a two-dimensional map of current density, $\vec{J}$, in the film from the measured B_z, as described in Section 7.5.1. This inversion has been implemented several ways and applied to magnetic images obtained by various methods including magneto-optics [Patnaik et al., 2003; Jooss et al., 2002; Koblischka and Wijngaarden, 1995a], scanning Hall probe microscopy [Grant et al., 1994], and scanning SQUID microscopy [Inoue et al., 2005; Kirtley et al., 1995].

*Parts of this Chapter are contained in Dinner et al. [2006a] and will be copyright ©2007 American Physical Society.

Other imaging techniques, such as scanning potentiometry [Perkins et al., 2001], scanning laser microscopy [Inoue et al., 2005; Abraimov et al., 2004], and scanning electron microscopy [Gross and Koelle, 1994] can map out the electric field, $\vec{E}$, that arises from vortex movement or other changes in local supercurrent density. In these techniques, to generate measurable electric fields, the superconductor is biased with a current I slightly greater than the dc critical current I_c at which vortices start to flow. In principle, such measurements could be combined with magnetic imaging of the same sample, and together, $\vec{J}$ and $\vec{E}$ would provide a complete, spatially-resolved electrical characterization of the material, including the local critical current density J_c, and the local power input, which can be calculated as $\vec{J} \cdot \vec{E}$.

In this Chapter, I demonstrate that for $I < I_c$, time-resolved magnetic imaging can simultaneously determine both $\vec{J}$ and $\vec{E}$ in a superconducting film. Figure 7.1 summarizes the operations involved. The instantaneous magnetic field $\vec{B}$ determines $\vec{J}$, while the time rate of change of $\vec{B}$ is related to $\vec{E}$ through Faraday's law,

$$\vec{\nabla} \times \vec{E} = -\partial_t \vec{B}. \tag{7.1}$$

This relation only constrains the inductive portion of electric field, $\vec{E}_i$. To reconstruct the remaining electrostatic part, $\vec{E}_p$, I must impose the additional restrictions that $I < I_c$, as discussed in Section 7.6, and that $\vec{E}$ is parallel to $\vec{J}$, discussed in Section 7.6.3. However, many important applications that are not accessible to techniques operating above I_c do lie within these restrictions, such as ac losses in superconducting films.

Faraday's law has been applied previously to derive ac loss from a critical state model of magnetic fields in a homogeneous, infinitely long superconducting strip [Norris, 1970; Brandt and Indenbom, 1993]. It has also been applied to one-dimensional magnetic measurements of strips [Giller et al., 1998]. In the present work, the electric field reconstruction is reformulated to allow for the two-dimensional inhomogeneity of a real conductor revealed by my magnetic images. This method also applies to the case of magnetization decay due to flux creep,

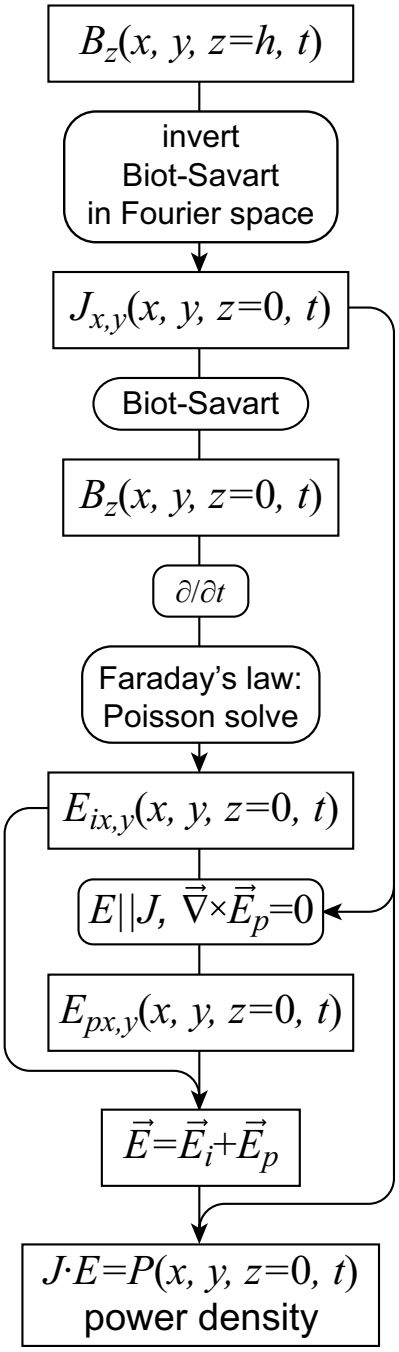

Figure 7.1: A flow chart illustrating how I use a series of magnetic field images to reconstruct sheet currents and electric fields in the sample, and finally dissipation.

which was recently analyzed using magneto-optic images [Jooss and Born, 2006].

Here, I modify the data acquisition method of my scanning Hall probe microscope to obtain a series of images of B_z as it evolves with time. To analyze ac losses, I image a strip of the high-temperature superconductor $YBa_2Cu_3O_{7-\delta}$ (YBCO), described in Section 7.2. I apply an ac current to the strip at 400 Hz, a typical operating frequency for applications [Kalsi, 2004], and must image the magnetic response faster than this. My scan speed—a few pixels per second—is slow in comparison, so instead of acquiring an entire sequence of images within one cycle of applied current, I obtain an average response over many cycles, as explained in Section 7.3, with 25 μs time resolution.

Section 7.4 presents this time series of magnetic images, which are then transformed into images of current and electric field in Sections 7.5 and 7.6. These quantities are combined in Sections 7.7 and 7.8 to yield maps of dissipation and superconducting characteristics.

7.2 Sample: YBCO strip

The YBCO film studied in this Chapter is 180 nm thick, grown epitaxially by pulsed laser deposition (PLD) on a $SrTiO_3$ [001] substrate. Photolithographic patterning followed by argon ion milling removes parts of the film, leaving a bridge as shown in Figure 7.3(a). The substrate is held in vacuum, attached to the microscope's copper coldfinger by a thin layer of low-temperature varnish. The coldfinger is cooled by a continuous flow of liquid helium. The film's T_c (defined by the maximum in dR/dT) is measured in this cryostat to be 90 K. For imaging, the film's coldfinger is held at 40 K while the Hall sensor is held at 54 K. However, the current return lead (to the right of the segment imaged) is narrower than the bridge (32 μm versus 50 μm), and a magnetic scan (not shown) indicates that the applied current of 0.75 Arms exceeds its critical current. The consequent dissipation in the return lead may heat the sample several degrees above 40 K.

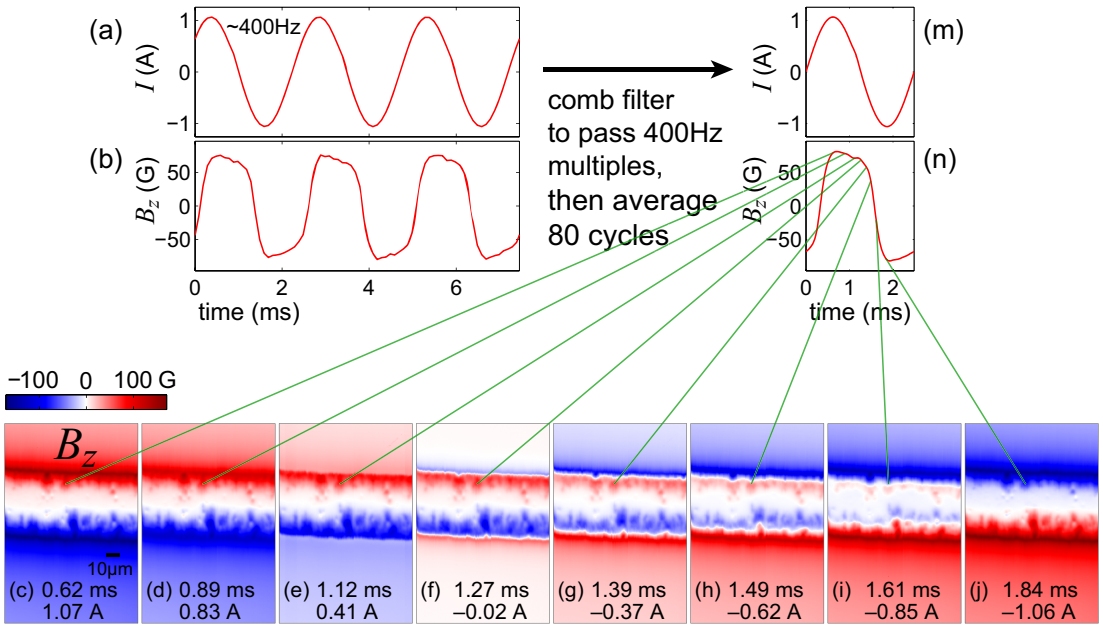

Figure 7.2: A time series of magnetic images is acquired in a single scan by pausing at each pixel and recording the magnetic response $B(t)$ for 80 cycles of applied current $I(t)$, excerpts of which are shown in (b) and (a). B and I are then broken into cycles using the zeros of $I(t)$. The cycles are averaged, and the resultant $B(t)$ determines one pixel that varies over time, shown in (n). The waveforms for all pixels are assembled into a time series of images, selected frames of which are shown in (c)–(j).

7.3 Acquiring time-resolved image series

The starting point for the flow chart in Figure 7.1 is B_z measured with both position and time resolution as in Figure 7.2(c)–(j). The frames in this time series are all derived from one scan. The sensor stops at the first pixel location, measures the AC magnetic response over many current cycles, moves to the next pixel, and repeats. I then collate the data corresponding to a particular time (or equivalently phase) relative to the beginning of the current cycle into one image, and repeat this for various times throughout the cycle. Thus the different pixels in one image are not measured simultaneously, and they represent an average magnetic response.

Specifically, I excite the Hall sensor with 24.6 μA DC, connecting its current leads to two 12.6 V lead-acid batteries in series between two 502 kΩ resistors, maintaining the sensor's potential near ground. I apply a continuous, sinusoidal current at 402.7 Hz to the bridge, whose negative contact is grounded. I then raster the sensor over the bridge, pausing at each pixel location to measure the Hall signal for 200 ms. The entire scan takes 4 hours.

To record the Hall waveforms, the sensor's voltage leads are connected to differential inputs of a preamplifier (Stanford Research Systems 560) via triaxial cable whose outer shield was grounded to the cryostat. The amplifier output as a function of time, t, is recorded with 16-bit resolution at 10 kilosamples/second by an ADC card (National Instruments AT-MIO-16XE-50) in a PC. A separate waveform is taken for each pixel, measured only while the sensor is stationary. The voltages are scaled to magnetic fields, $B(t)$, using known sensor and amplifier calibrations. An excerpt of $B(t)$ from one pixel is shown in Figure 7.2(b).

While recording $B(t)$, the ADC card simultaneously records a relatively noiseless waveform proportional to the sample current, $I(t)$, as shown in Figure 7.2(a), for each pixel.* The positive-slope zero-crossing times in $I(t)$ are used to break both I and B into individual current cycles, which are then overlaid and scaled slightly as necessary to make each cycle start and end at the same time.† Finally, I average these data to obtain the local magnetic response over the cycle as shown in Figure 7.2(c)–(j). The averaging uses a Gaussian window with a FWHM of 25 μs evaluated every 25 μs over the 2.5 ms period.

The choice of a 25 μs time step is based on the settling time of the ADC.‡ A given sample actually represents an average of the signal over a fraction of

*The ADC card actually acquires the two waveforms by scanning its ADC between the two inputs, thus the samples are interleaved in time rather than simultaneous. The resultant 50 μs time shift is corrected before averaging the Hall or sample voltage waveforms.

†Instead of finding zero-crossings, one could fit a sinusoid to $I(t)$ to determine its frequency and phase, which could be used to break $B(t)$ into cycles. I found, however, that $I(t)$ showed slight, but statistically significant, variations in frequency within each waveform, causing the sinusoid to misrepresent some cycles.

‡The ADC card is rated to settle from full range to 1 least-significant-bit within 50 μs. In the 25 μs interval used here, it would settle to 4 mV, which translates to a magnetic field of 0.1 G, from the maximum value of 1 V.

this time interval, limiting the rate at which any feature will appear to change. With improved electronics, however, the technique described here could be used to image much faster periodic phenomena.

The averaging constitutes a software lock-in technique that suppresses components of the signal that are not periodic in the frequency of the applied current. For instance, the field of a single vortex moving by a pixel would be largely averaged out, unless its position is reproducible from cycle to cycle. I further suppress such non-periodic components by applying a comb filter. I Fourier transform the B waveform from the time to the frequency domain, zero components not within 45 Hz of a 400 Hz harmonic, then transform back to the time domain.

After averaging over the cycles, I discard the mean of $B(t)$ at each pixel, isolating the response to the sample current from any static ambient field or slowly varying Hall voltage offset. Finally, the data from all pixels are assembled into 100 images corresponding to 25 μs time slices. Figure 7.2(c)–(j) are selected from this larger set of frames.

A standard lock-in measurement—multiplying $B(t)$ by $I(t)$ and measuring the DC component of the result—would yield the strength of the first harmonic in the B waveform, which would correctly represent the data if $B(I)$ were always linear. This is approximately true in the Meissner regime, i.e. when the applied current is too small for vortices to penetrate. In contrast, vortex movement causes a non-linear, hysteretic $B(I)$—higher harmonics of the driving frequency make up a significant part of the signal. In this case, the data is better visualized as the series of images in Figure 7.2(c)–(j), where each frame is a compilation of B from all pixels at the same time in the current cycle, assembled from the interpolated waveforms $B(t')$.

7.4 Magnetic image results

This Chapter is primarily concerned with deriving quantities of interest from time-resolved magnetic images, but it is worth first examining the images directly. From them, I extract a great deal of qualitative information that shapes the

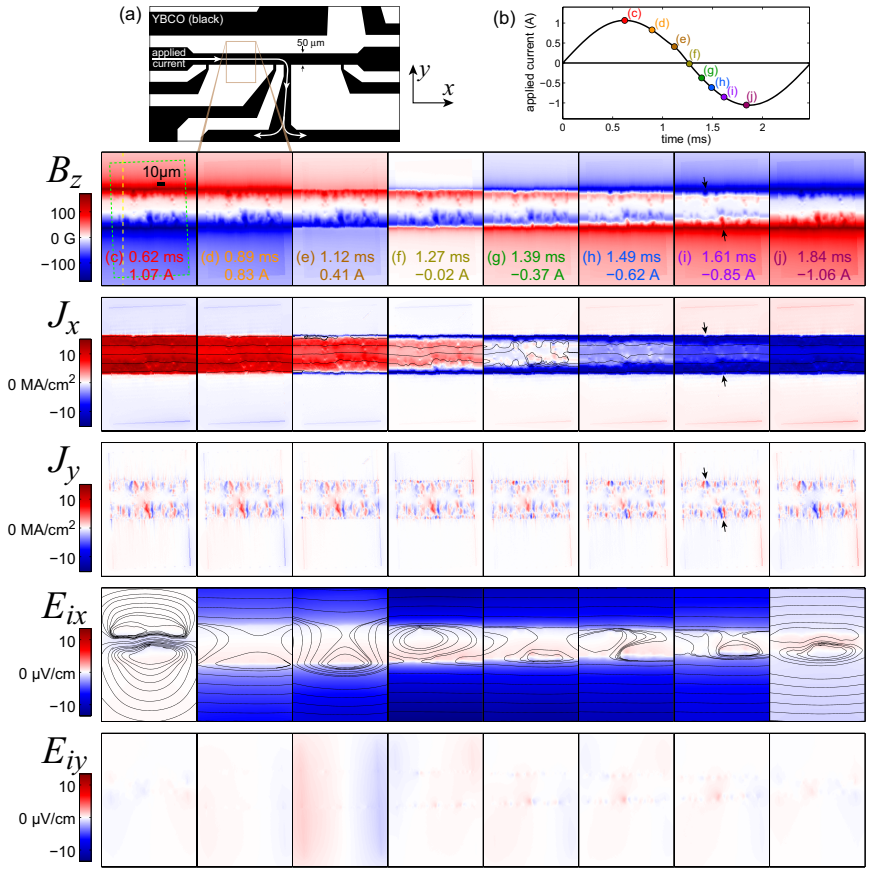

Figure 7.3: Imaging current-induced flux penetration into a YBCO film: (a) Illustration of the sample geometry. The approximate area of the magnetic images is outlined by the brown box. Current is injected at the left and extracted from the downward-facing lead; the right-facing current lead and smaller voltage leads are not used (floating). (b) Applied current during a 0.75 Arms, 400 Hz cycle. Select times are marked, and the corresponding magnetic images are shown in (c)–(j). Image (c) indicates the scale and boundary of the experimental data (dashed green box); the background outside of the data is filled by a fit to a critical state model. The vertical dashed yellow line indicates the location of the cross sections shown in Figure 7.4. In image (i), the black arrows point out two spots where vortices enter the film more easily. Below (c)–(j) are reconstructions from the magnetic data: components J_x and J_y of the current density flowing in the sample, and components E_{ix} and E_{iy} of the inductive portion of the electric field. Color scales for x and y components are the same. Black streamlines of $\vec{J}$ and $\vec{E}_i$ overlay their x components. The complete set of frames is presented as the movie `BJE.avi`.

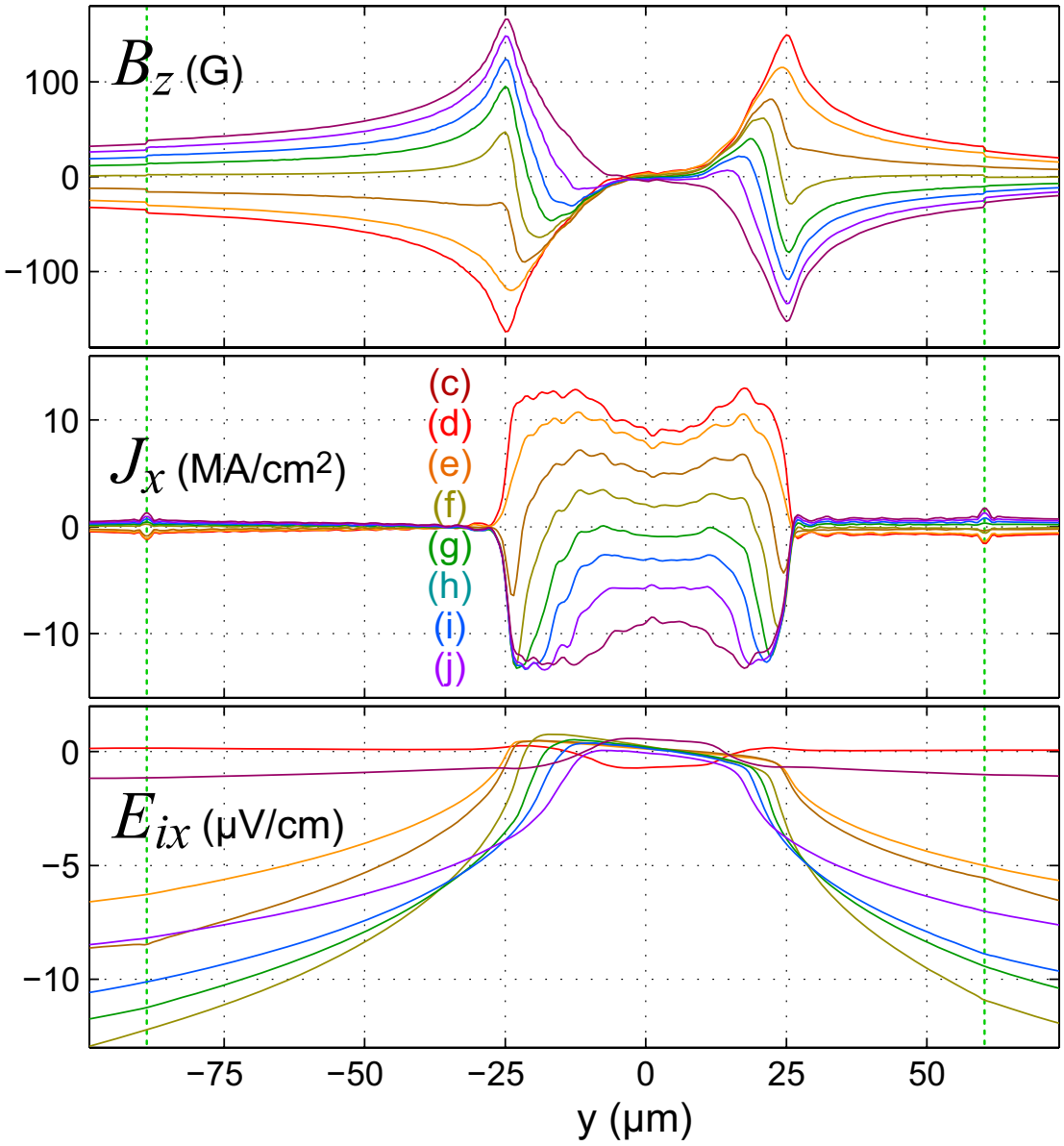

Figure 7.4: Cross sections of the data in Figure 7.3. The sections are taken along the y axis at the location of the dashed yellow line in Figure 7.3(c). The vertical dashed green lines mark the boundary between data and background fit. Successive frames in the current cycle are overlaid; their colors and labels match the frame labels in Figure 7.3.

assumptions under which further quantities are derived.

Selected frames are plotted in Figure 7.3(c)–(j), and represent one half-cycle of ac applied current. Initially, the maximum current I=1.07 A is applied and flux has penetrated, somewhat inhomogeneously, into both edges of the strip. I is apparently below the critical current, I_c, as a central flux-free region separates the two flux fronts. This condition is necessary for my calculation of electric field, as explained in Section 7.6.

By (f), the applied current is reduced to zero, and vortices remain trapped in the edge regions. Flux of the opposite sign starts to enter at the edges. This opposite flux then erases and replaces the trapped flux as negative current is applied. The succeeding half of the cycle approximately repeats the B, J, and E configurations shown, but with opposite signs.

The boundary of the data is shown as a dashed green box in (c). The surrounding background is calculated with a critical state model for a thin superconducting strip [Brandt and Indenbom, 1993; Zeldov et al., 1994]. The main purpose of this background is to better match the boundaries of the image for the Fourier transformations described in Section 7.5.1. The good agreement between the model and the data also shows that much of the strip's response can be ascribed to critical state behavior, though deviations, such as spatial inhomogeneity in pinning strength, are evident.

The model is fit to the entire set of frames at once. The free parameters are the height of the sensor above the sample plane, 1.2 μm, the sensor tilt, 3° about the x axis, the strip's critical current, 1.13 A, the Hall coefficient, 0.10 Ω/G, and the amplitude, 7.2 Oe rms, of an applied field proportional to the applied current, explained below. The Hall coefficient's fit value is consistent with the calibrated value of 0.11 Ω/G. The y position and tilt of the strip about the z axis are also allowed to vary, and the tilt is zeroed by rotating the image. These parameters are constrained to be constant over time; the only change in the calculation from frame to frame is the (known) applied current.

Adding the small, uniform applied field that varies with the applied current improves the fit, and is suggested by the sample geometry in Figure 7.3(a), where

the current returns to the right and below the bridge. Positive returning current generates a negative field at the section of bridge imaged, which accords with the sign of the field added to the calculation. Furthermore, the vertical segment of the return lead should add a negative dB/dx, which is not accounted for by the calculation, and which does explain why the disparity between the data and the calculation is largest toward the lower right corner of the boundary.

7.5 Current reconstruction

7.5.1 Magnetic inversion with regularization

The Biot-Savart law describes the magnetic field $\vec{B}$ generated by a current distribution $\vec{J}$,

$$\vec{B}(\vec{r}) = \frac{\mu_0}{4\pi} \int d^3\vec{r'} \frac{\vec{J}(\vec{r'}) \times (\vec{r} - \vec{r'})}{\left|\vec{r} - \vec{r'}\right|^3}. \tag{7.2}$$

Several authors have tackled the problem of inverting this relation to obtain a planar current distribution $\vec{J}(x, y)$ from a planar magnetic measurement $B_z(x, y)$ [Roth et al., 1989; Wijngaarden et al., 1998; Feldmann, 2004]. I tried two of these existing methods: regularization [Feldmann, 2004] and conjugate-gradient [Wijngaarden et al., 1998]. The conjugate-gradient method produces current distributions dominated by unphysical artifacts. Further testing with simulated data suggests that this occurs when the current distribution extends outside the image boundaries, as in my images, which encompass only a section of the superconducting strip.

I met with greater success using the regularization method with generalized cross-validation (GCV), described in detail in Feldmann [2004] and summarized here. Taking the z component of Equation 7.2 and Fourier transforming in x and y, I find an algebraic relation between the Fourier transformed quantities $\tilde{B}_z$, $\tilde{J}_x$, and $\tilde{J}_y$:

$$\tilde{B}_z(k_x, k_y, z) = \frac{\mu_0}{2} e^{-kz} \frac{i}{k} \left(k_y \tilde{J}_x - k_x \tilde{J}_y \right). \tag{7.3}$$

I assume that J_z, current flowing perpendicular to the plane of the film, is insignificant. I also ignore any z dependence of the in-plane components of current, approximately solving for the current density averaged over the film thickness. These are reasonable approximations in my film's geometry; its thickness, 180 nm, is smaller than its effective London penetration depth, $\lambda_{\text{eff}} = \lambda_{ab}/\tanh(d/2\lambda_{ab}) =$ 400 nm [Djordjevic et al., 2002; Carneiro and Brandt, 2000]. The specific kernel that I use to relate J_x and J_y to B_z is that of a film of 180 nm thickness [Feldmann, 2004].

I now reduce J_x and J_y to a single unknown by noting that $\vec{J}$ must be nearly divergence-free at the operating frequency of 400 Hz (the resonant frequency, $1/\sqrt{LC}$, of a piece of strip like that imaged would be $\sim$ 100 GHz). This allows us to derive both J_x and J_y from the local magnetization $g(x, y)$ [Brandt, 1995], where

$$\vec{J}(x, y) = -\hat{z} \times \vec{\nabla} g(x, y) \Rightarrow J_x = \partial_y g,\ J_y = -\partial_x g. \tag{7.4}$$

In Fourier space,

$$\tilde{g}(k_x, k_y) = \frac{i}{k^2}\left(k_y \tilde{J}_x - k_x \tilde{J}_y\right). \tag{7.5}$$

Equations 7.3 and 7.5 yield

$$\tilde{g} = \frac{2}{\mu_0} e^{kz} \frac{1}{k} \tilde{B}_z. \tag{7.6}$$

Thus my basic procedure is to Fourier transform B_z, solve for $\tilde{g}$, Fourier transform back to the real space $g(x, y)$, and use Equation 7.4 to obtain J_x and J_y.

The first difficulty arises from the factor e^{kz} in Equation 7.6. Spurious high spatial frequencies (with wavelength greater than z, the measurement height) in the magnetic data are exponentially amplified in the inverted current. While scanning Hall probe microscopy enjoys lower noise and smaller z than magneto-optical imaging [Bending, 1999], noise in my images can still dominate the reconstructed J. The method of regularization compensates by suppressing high frequencies (smoothing), and GCV determines an optimal amount of regularization from the data itself. In practice, I used GCV as a guide to choose a regularization parameter ($\lambda = 100$ as described in Feldmann [2004]) that I held fixed across the set of frames.

Similarly, differentiating g to find the components of J amplifies high-frequency noise, so I use Savitsky-Golay smoothing to extract the derivatives. The smoothing is quadratic with a frame size of 2.5 μm (5 pixels).

The second difficulty is that the Fourier transform of B assumes periodicity in the vertical and horizontal directions, and mismatches between the left and right, and top and bottom boundaries of the B image lead to artifacts dominating the image once it has been transformed, manipulated, and transformed back. A common solution is to window the data, bringing its boundaries smoothly to zero. This discards a large portion of each image, however.

Instead, I rotate the original data (2.3° about the z axis) so that the bridge runs horizontally, then center it on a larger area (a square 256 μm on a side) in order to move the edge effects away from the data. I fill in the background with a calculated B as described in Section 7.4. Only after calculating $\vec{J}$ and $\vec{E}_i$ (described in Section 7.6.1) do I crop the images back to the original dimensions (plus the margin seen in Figure 7.3(c)). Finally, before Fourier transforming, I mirror the images top-to-bottom in order to better match the top and bottom edges without going to the much larger area necessary to allow the field to die off, which would be more computationally cumbersome.

While these preparations remove artifacts associated with edge mismatch, I do observe a spurious bump in the reconstructed current at the boundary between data and fit, seen clearly in the cross section of J_x in Figure 7.4. However, this artifact is about ten times smaller than my signal, and appears to be confined to the boundary.

7.5.2 Discussion of current density images

The results largely agree with my expectations for a superconducting strip. The reconstructed current flows within the strip approximately in the x direction. At the maximum applied current (Figure 7.3(c)), the current density, $|\vec{J}|$, in the edge regions of flux penetration should equal the critical current density, according to the critical state model. J then dips down (but is not zero) in the vortex-free

central region, as expected from the demagnetization effect of the strip geometry [Brandt and Indenbom, 1993; Zeldov et al., 1994]. This separation into edge and central regions is clearest in the cross section of J_x, Figure 7.4(c). J averaged over the edge regions is 12 MA/cm^2, which accords with macroscopic transport measurements of J_c on a similar film (9 MA/cm^2 at 44 K) [Daniels et al., 2000]. One expects transport, which is sensitive to the weakest point in a superconductor, to yield a lower value than the spatially averaged J_c.

The cross section of J_x also shows more current on the $-y$ side, indicative of the applied field (described in Section 7.4) modifying the symmetric distribution one would expect for an applied current. While the cross sections vary along the length of the strip, this asymmetry is typical.

J_y, plotted on the same color scale as J_x, is smaller, but highlights where the current reroutes around apparent weak spots in the film. Spots producing the largest J_y are marked with arrows in Figure 7.3(i). These features in J_y correspond to bumps in the streamlines overlaid on J_x where the current spreads around these defects. In the following Sections, I show that these are also spots of high electric field and dissipation.

7.6 Electric field reconstruction

Faraday's law relates electric field to the time derivative of magnetic field,

$$\vec{\nabla} \times \vec{E} = -\partial_t \vec{B}. \tag{7.7}$$

Taking the z component,

$$\partial_x E_y - \partial_y E_x = -\partial_t B_z. \tag{7.8}$$

This only defines $\vec{E}$ up to the gradient of a scalar. I therefore use the Helmholtz decomposition to separate the electric field into a divergence-free inductive portion, $\vec{E}_i$, and a curl-free electrostatic portion, $\vec{E}_p$ (following the notation of Jooss

and Born [2006]),

$$\vec{E} = \vec{E}_i + \vec{E}_p. \tag{7.9}$$

$\vec{E}_p = -\vec{\nabla}\phi$ where ϕ is a scalar potential and $\vec{\nabla} \cdot \vec{E}_p = \rho/\epsilon_0$, the charge density. My measurements determine $\vec{E}_i$ through Equation 7.8, but do not determine $\vec{E}_p$ without further constraints, as described in Section 7.6.3.

To illustrate: If I apply a dc current $I > I_c$ to my strip, flux flow or other resistive behavior generates an $\vec{E}_p$, but I would see little time variation of the magnetic field when averaging over length scales greater than the intervortex spacing. In contrast, for $I < I_c$, the voltage and electric field (both $\vec{E}_i$ and $\vec{E}_p$) are zero in the steady state. I therefore remain below I_c of my superconducting strip in order to minimize unmeasurable portions of $\vec{E}_p$.

Furthermore, below I_c, even in a dynamic state, $\vec{E}_p$ remains zero for a strip that is uniform in x with no Hall effect. In this case, symmetry dictates that $E_y = 0$, $E_z = 0$, and $\partial_x E_x = 0$, thus $\vec{\nabla} \cdot \vec{E} = 0$. Then $\vec{E}_p$ is uniform, and zero below I_c. Thus all of the behavior I expect from a model strip will be contained in $\vec{E}_i$.

7.6.1 Inductive electric field $\vec{E}_i$

To reconstruct the divergence-free $\vec{E}_i$, I proceed as for $\vec{J}$, solving for a potential function h where

$$\vec{E}_i(x,y) = -z \times \vec{\nabla} h(x,y) \Rightarrow E_{ix} = \partial_y h,\ E_{iy} = -\partial_x h \tag{7.10}$$

in which case Equation 7.8 becomes a Poisson equation for h:

$$-\partial_x^2 h - \partial_y^2 h = -\partial_t B_z \tag{7.11}$$

$$\nabla_{2D}^2 h = \partial_t B_z \tag{7.12}$$

I am interested in the electric field in the sample plane ($z = 0$) rather than the measurement plane. I therefore need $B_z(z = 0)$, which I obtain from the current distribution via the Biot-Savart law. B_z at any height is easily computed by

rearranging Equation 7.6 to obtain $\tilde{B}_z$ in terms of $\tilde{g}$, the magnetization function from which $\vec{J}$ is derived:

$$\tilde{B}_z = \frac{\mu_0}{2} e^{-kz} k \tilde{g}. \tag{7.13}$$

It is also easiest to solve the Poisson equation in Fourier space, where Equation 7.12 becomes

$$(ik)^2 \tilde{h} = \partial_t \tilde{B}_z (z = 0) \tag{7.14}$$

and, combining Equations 7.13 and 7.14,

$$\tilde{h} = -\frac{\mu_0}{2k} \partial_t \tilde{g} \tag{7.15}$$

To approximate the time derivative of $\tilde{g}$, I compute twice the final number of frames (200 frames spaced by 12.5 μs, but each still averages a 25 μs interval) and take the differences between successive even frames. I can then calculate simultaneous electric field and current at the times of the odd frames.

Once I have solved for $\tilde{h}$ and transformed back to real space, I use Savitsky-Golay smoothing, as with J, to extract the partial derivatives corresponding to E_{ix} and E_{iy}.

Finally, Equation 7.8 only defines E_{ix} and E_{iy} up to constants. Setting the constants is equivalent to finding a field-free point, to which Norris devoted much care [Norris, 1970]. I set the zeros based on the edges of the uncropped images, as far from inhomogeneities in the data as possible. For the E_{ix} zero I use the mean of the two pixels at the vertical center of the strip (where I expect no E, as Norris pointed out) on the left and right edges. I set the E_{iy} zero to the mean of the four corners. This mean is zero for an ideal strip, and minimally affected by fields originating toward the center of the image.

7.6.2 Discussion of $\vec{E}_i$ images

As the applied current decreases over the half cycle shown, E_{ix} remains approximately zero (white) in a central region of the strip. Outside of this region it becomes negative (blue), continuing past the strip edges. This is also visible in

the cross sections of E_{ix} in Figure 7.4. This behavior accords with my expectations for vortices moving into the edges of the film. The central region shrinks, tracking the flux front as vortices enter. Although vortices and current from the previous half cycle are present inside the central region, the vortices remain pinned and therefore do not generate an electric field.

The central region is not completely field-free, however. Interestingly, the field it does display—about 10 times smaller than the edge fields—is maximal and opposite to the current when $dI/dt = 0$, a point where my critical state model would dictate $E = 0$. Such a field would arise, though, from a relaxation of J_c, i.e. flux creep in which the vortices continue to move into the strip even as the current momentarily stops ramping. It leads to a (temporary) negative power input to the film, discussed in Section 7.7.

Such movement while $dI/dt = 0$ is also visible in the full set of magnetic images. While the magnetic field evidence alone is subject to errors in phase relative to the applied current, the electric field confirms that the relaxation is real. Such relaxation is the focus of Jooss and Born [2006].

Finally, the cross sections of E_{ix} reveal an unexpected negative tilt, dE/dy, both in the central and outer regions, which is an error that arises from the tilt of the Hall sensor, as shown in Section 7.9.

7.6.3 Electrostatic electric field $\vec{E}_p$

I established in Section 7.6 that for a uniform superconducting strip with no Hall effect below I_c, $\vec{E}_p = 0 \Rightarrow \vec{E} = \vec{E}_i$, even with an ac current. Indeed, the $\vec{E}_i$ that I observe contains all the features I expect from a uniform strip, as discussed in Section 7.6.2. My images, however, also reveal inhomogeneity, which could produce a non-zero $\vec{E}_p$.

Here I show that in spite of this inhomogeneity, I expect the total electric field $\vec{E}$ to remain approximately parallel to $\vec{J}$ locally, which proves sufficient to reconstruct $\vec{E}_p$ as the field that compensates for any component of $\vec{E}_i$ perpendicular to $\vec{J}$. My method is inspired by Jooss and Born [2006], but I do not make the

additional and incorrect assumption that the component of $\vec{E}_p$ parallel to $\vec{J}$ is zero.* I also describe a rather different route to $\vec{E}$ and $\vec{E}_p$ in Section 7.9.1.

Validity of the constraint $\vec{E}\|\vec{J}$

First I must justify that in my experiment, $\vec{E}$ is parallel to $\vec{J}$, emphasizing that this will not be true for all materials. For example, a material can have an intrinsic Hall effect. However, macroscopic transport measurements indicate that for YBCO in the superconducting state, the Hall effect is insignificant; the component of $\vec{E}$ perpendicular to $\vec{J}$ is at most 1000 times smaller than the parallel component [Kunchur et al., 1994].

Another violation of $\vec{E}\|\vec{J}$ could arise from a feature such as a grain boundary, whose orientation prevents vortices from moving perpendicular to $\vec{J}$. More generally, any gradient in superfluid condensate energy density will exert a force on vortices. I show here, however, that at least on lengths scales greater than the image resolution of 1 μm, I can rule out the presence of gradients strong enough to compete with the pinning forces that occur on the scale of the coherence length, $\xi \approx 2$ nm. I put an upper bound on such a gradient in my material by assuming that the gradients in pinning strength that I observe stem entirely from changes in condensate energy density. I take J (the magnitude of the current density) at maximum applied current as a map of J_c near the edges of the strip (as discussed in Section 7.5.2). The magnitude of the pinning force per length for a single vortex is

$$F_p = \Phi_0 J_c \tag{7.16}$$

from which I estimate the depth of the vortex pinning potential as $V_p = F_p \xi$. The line energy of the vortex will be $\sim V_p \cdot 10$, from the ratio of the calculated depairing current to the measured J_c [Gurevich, 2006]. Thus the gradient of F_p yields a gradient of line energy, i.e. a force F_{grad}, whose magnitude I compare to F_p. I find that F_p/F_{grad} averages 2000 over the edge regions of the strip with a

*Jooss and Born [2006] makes a physically motivated argument that $E_{p\|}$ is approximately zero for the case of magnetization decay. This argument is incorrect and leads to a significant curl in $\vec{E}_p$, visible in Figure 12 of Jooss and Born [2006] as $-\partial_y E_{px} + \partial_x E_{py} \neq 0$.

minimum of 200.

This analysis suggests that in my material, the Lorentz force from the current at J_c, along with pinning forces, dominate other forces felt by vortices, so that vortices move perpendicular to $\vec{J}$ and generate $\vec{E}$ parallel to $\vec{J}$. However, I do not claim to rule out every possible materials effect, e.g. effects that average out below my resolution of 1 μm.

Method of reconstructing $\vec{E}_p$

Starting with $\vec{E}_i$ and $\vec{J}$, reconstructed in Sections 7.6.1 and 7.5, and the constraint that $\vec{E} = \vec{E}_i + \vec{E}_p$ is parallel to $\vec{J}$, I can solve for $\vec{E}_p$. The component of $\vec{E}_p$ perpendicular to $\vec{J}$ must cancel that of $\vec{E}_i$:

$$E_{p\perp} = -E_{i\perp} \tag{7.17}$$

where $E_{i\perp}$ is calculated by subtracting from $\vec{E}_i$ its projection onto $\vec{J}$. Having obtained $E_{p\perp}$, I construct $E_{p\parallel}$, the component of $\vec{E}_p$ parallel to $\vec{J}$, to satisfy

$$\vec{\nabla} \times \vec{E}_p = \vec{0} \tag{7.18}$$

which follows from the definition of $\vec{E}_p$. The z component of Equation 7.18 tells us that at each point,

$$\partial_\perp E_{p\parallel} = \partial_\parallel E_{p\perp} \tag{7.19}$$

or more explicitly,

$$-\frac{J_y}{J}\partial_x E_{p\parallel} + \frac{J_x}{J}\partial_y E_{p\parallel} = \frac{J_x}{J}\partial_x E_{p\perp} + \frac{J_y}{J}\partial_y E_{p\perp}, \tag{7.20}$$

which is a linear, first-order partial differential equation for $E_{p\parallel}(x, y)$.

I tried two approaches to solving this equation for $E_{p\parallel}$. In the first, I start with a trial solution, $\vec{E}_{p1}$, composed of the known $E_{p\perp}$ and $E_{p\parallel} = 0$. I calculate its curl $(\vec{\nabla} \times \vec{E}_p)_z$, which will be zero for the true $\vec{E}_p$. From the curl, I reconstruct a divergence-free field $\vec{F}$ following the same procedure I used to reconstruct $\vec{E}_i$ from

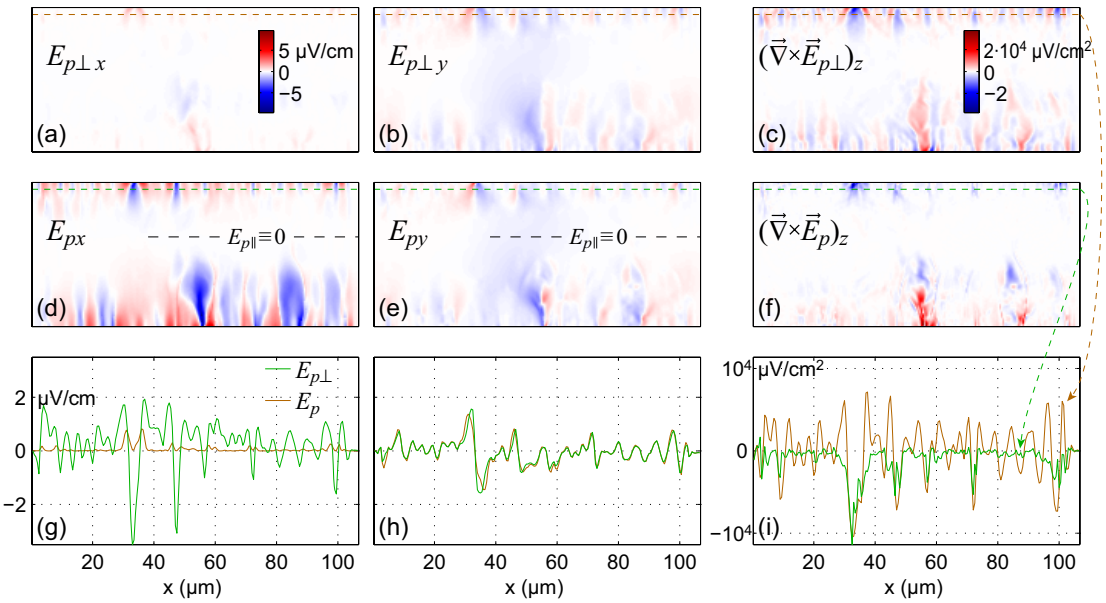

Figure 7.5: Reconstructing the electrostatic portion of electric field, $\vec{E}_p$: All images are cropped to the area of the strip. The electric fields are on the same color scale, shown in (a), and the curls are on the scale shown in (c). (g)–(i) are x cross sections from the images above them, with locations indicated by the dashed lines of matching color. The cross sections also indicate the spatial scale of the images. The component of E_p perpendicular to the current, (a)–(b), is obtained from E_i under the assumption $\vec{E}\|\vec{J}$. However, (c) shows that this component alone does not satisfy $\vec{\nabla}\times\vec{E}_p = 0$. I calculate and add a parallel component, yielding the complete $\vec{E}_p$ in (d)–(e). My $E_{p\|}$ calculation requires an integration constant, defined by assuming $E_{p\|} = 0$ along the lines shown in (d) and (e). Adding $E_{p\|}$ suppresses, but does not perfectly cancel, $\vec{\nabla}\times\vec{E}_p$, as seen in (f) compared to (c), and from the cross sections in (i).

B_z, described in Section 7.6.1. The reconstruction preserves $\vec{\nabla} \times \vec{F} = \vec{\nabla} \times \vec{E}_{p1}$, so $\vec{G} \equiv \vec{E}_{p1} - \vec{F}$ is curl-free, as desired. However, $\vec{G}$ does not preserve $E_{p\perp}$. So I construct a new trial $\vec{E}_{p1}$ consisting of the components $G_\parallel$ and $E_{p\perp}$, and iterate. The true $\vec{E}_p$ would remain unchanged by such a procedure. In practice, however, I found that the procedure misconverged to an $\vec{E}_{p1}$ with larger curl than the initial trial.

I therefore attempted a more direct integration of Equation 7.19:

$$E_{p\parallel} = \oint \partial_\parallel E_{p\perp} ds \tag{7.21}$$

where the integral is taken along a path $\vec{s}$ that remains perpendicular to $\vec{J}$ at each point along its length, and starts at some (x, y) such that $E_{p\parallel}(x, y) = 0$.

The result, constructed from many such paths, is shown in Figure 7.5. The initial data ($\vec{J}$ and $\vec{E}_i$) is taken from frame h in Figure 7.3, then cropped to the area of the strip. For starting points, I set $E_{p\parallel}(x, y) = 0$ along the horizontal line shown in Figure 7.5(d). In practice, to ensure coverage of every pixel, I start a path at each pixel and work back to the zero line. For efficiency, I skip pixels that have been covered by previous paths.

$E_{p\perp}$, shown in Figure 7.5(a)–(b), represents the starting data from which I calculate $\partial_\parallel E_{p\perp}$. Integration gives us $E_{p\parallel}$, which I add (as vector components) to $E_{p\perp}$ to obtain (d)–(e). The method is far from perfect, as evinced by the non-zero $\vec{\nabla} \times \vec{E}_p$ in (f). However, in comparison to (c), the curl is suppressed at all but the highest points. This is clear in the cross sections through (c) and (f) shown in (i). So the result of the procedure, (d)–(e), is closer to, but still short of, the true, curl-free $\vec{E}_p$.

Finally, I note that this method gives us no information about $\vec{E}_p$ outside the sample, where $J = 0$. However, outside the strip the charge density $\rho/\epsilon_0 = \vec{\nabla} \cdot \vec{E}_p = 0$. Then $\vec{E}_p = -\vec{\nabla}\phi$ where ϕ obeys Laplace's equation, $\nabla^2\phi = 0$, with a Neumann boundary condition given by $\vec{E}_p$ in the strip.

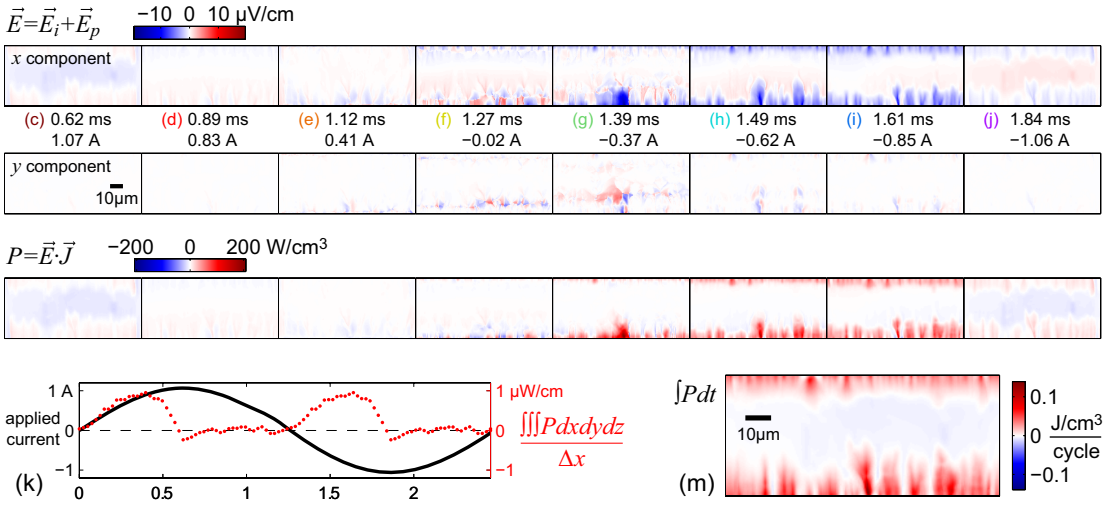

Figure 7.6: (c)–(j) The total electric field, $\vec{E}$, and power, P, for the same set of frames shown in Figure 7.3. The images are cropped to the area of the strip. (k) Integrating P over the area of each image and the thickness of the film, and normalizing by the length of strip imaged, I obtain the total power input as a function of time over a cycle of applied current. (m) Integrating P over time yields the spatial distribution of energy input over a cycle. Any reactive component of P integrates to zero, leaving only the dissipated energy.

7.6.4 Discussion of $\vec{E}_p$ images

Figure 7.6(c)–(j) shows the total electric field, $\vec{E} = \vec{E}_i + \vec{E}_p$, for the set of frames from Figure 7.3. The complete set of frames is assembled into the movie `EP.avi`. My sample clearly deviates from a uniform strip, in which $\vec{E}_p = \vec{0}$. $\vec{E}_p$ is comparable in magnitude to $\vec{E}_i$, but much more inhomogeneous, contributing most at the spots identified by arrows in Figure 7.3(i) as weak points of the superconductor.

Thus I demonstrate reconstruction of the total electric field from my time-resolved magnetic images. I reiterate that this analysis is restricted to materials in which $\vec{E}$ is parallel to $\vec{J}$, and in which I can identify a field-free kernel.

7.7 Reconstructed power input

Armed with $\vec{J}$ and $\vec{E}$, I calculate $P = \vec{J} \cdot \vec{E}$, the local power input to the film, resolved in time and space. The results are shown in the third row of Figure 7.6. The largest features are the positive edge regions where vortices move in as the current sweeps. I note that the instantaneous power shown arises from both dissipation and reactance. These are not easily separated (e.g. by the relative phase of J and E) because of the nonlinear relationship between J and E.

I can relate my local measurements to macroscopic transport measurements by integrating over space, shown in Figure 7.6(k). Each frame of the 50-frame set covering the central portion of the current cycle is summed and normalized by the length of strip imaged to obtain power per unit length, then plotted at its time within the cycle of applied current. These points are repeated in the first and fourth quarters of the cycle (in which J and E repeat with opposite signs). I note that when integrating over the entire sample (which I only do imperfectly by integrating over the image area), I expect no contribution to the power from the electrostatic field, $\vec{E}_p$, which, exerting a conservative force, cannot do work. Indeed, dropping $\vec{E}_p$ from the calculation shown in (k) does not change the result significantly.

The power input rises as the magnitude of current increases, but then falls back to become negative as the current reaches its peak. An inductive response with zero resistance would be zero at the peak. Instead, as discussed in Section 7.6.2, this negative contribution (E opposite J) arises from relaxation of J_c. As the applied current decreases back to zero, I do not recover much power, as I would in a dissipation-free inductor, because the vortex movement is irreversible—the vortices remain pinned.

When integrating over time, any inductive contributions to the instantaneous power input cancel, leaving the sum of dissipation over one cycle, shown in Figure 7.6(m). As in the instantaneous power, the edge contributions dominate. Integrating this image over space, or equivalently integrating the power in (k) over time, I obtain the energy dissipation per length of conductor, $6.6 \cdot$

10^{-10} J/cm/cycle. For comparison, a calculation from the critical state model using the applied I (1.07 A peak) and fit value of I_c (1.13 A) yields $1.2 \cdot 10^{-9}$ J/cm/cycle [Brandt and Indenbom, 1993]. Factors in the lower measured value may include suppression of high spatial frequencies in the reconstructed quantities due to regularization (see Section 7.5.1) and cropping of the image, which may exclude some pixels near the edges of the strip.

This energy dissipation translates to an average power of $2.7 \cdot 10^{-7}$ W/cm, which, given the applied current of 0.75 Arms, implies a voltage of 6.9 nVrms between the voltage taps, which are spaced by 260 μm. I have not attempted to verify the presence of this small but perhaps measurable voltage.

7.8 Local E–J relations

Over the cycle of applied current, each location in the film experiences a range of current densities and electric field strengths. By plotting E against J for each pixel, I obtain a local characterization of the material. For example, the E–J curve has often been used to test models of the flux pinning mechanism [Gurevich, 1990; Yeshurun et al., 1996; Blatter et al., 1994; Beasley et al., 1969; Anderson and Kim, 1964].

Figure 7.7 shows E–J curves for one column of pixels at the locations indicated in the inset. One curve is highlighted, illustrating a plausible E–J relation for a superconducting film. While the points at low J display several μV/cm of scatter, there is a clear upturn at $J_c \approx 10$ MA/cm^2. This value is consistent with the 12 MA/cm^2 I observe in the edge regions of the strip at maximum applied current, and with 9 MA/cm^2 from transport measurements of a similar film at 44 K, as discussed in Section 7.5.2 [Daniels et al., 2000]. However, as in Section 7.7, I caution that the electric field I measure arises from both dissipation and reactance, and in comparing my data with a purely dissipative dc E–J curve, I ignore reactance.

Although many of the curves seem reasonable, they deviate significantly between pixels, with upturns at current densities ranging from 14 to 2 MA/cm^2.

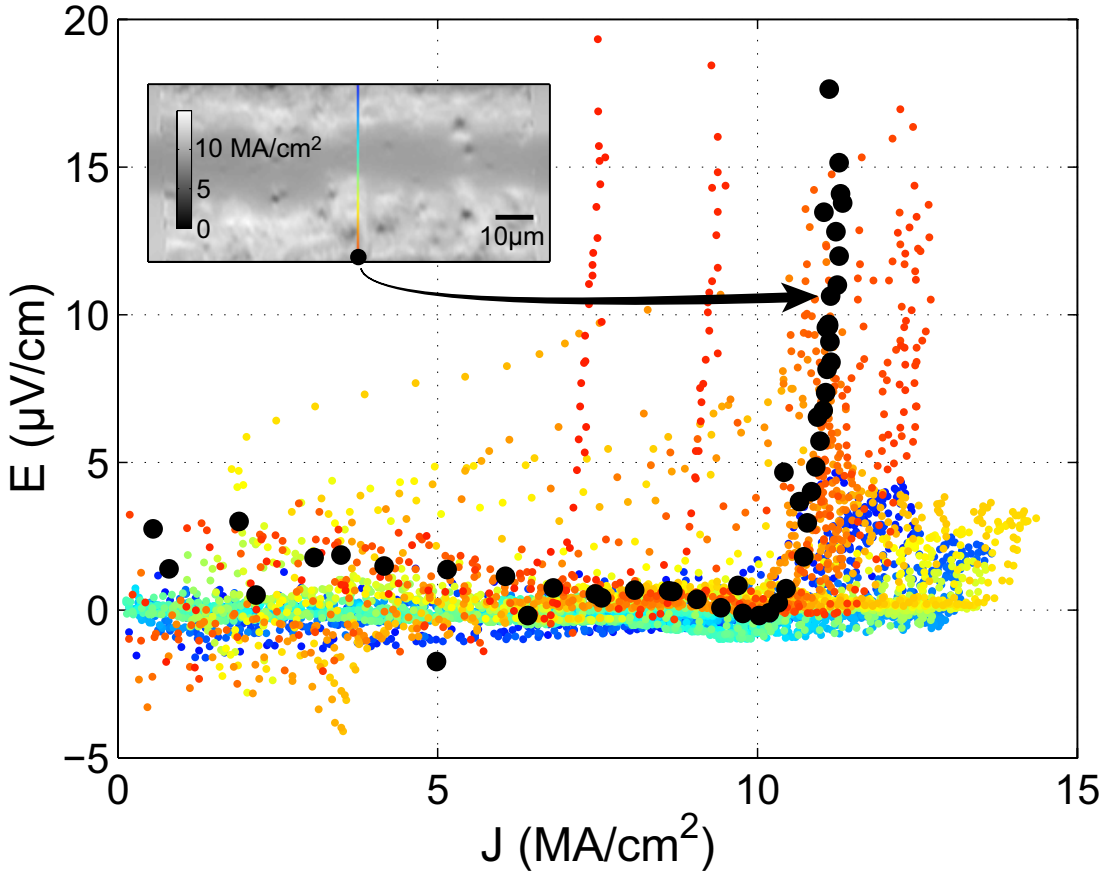

Figure 7.7: E, the magnitude of the projection of the total electric field onto $\vec{J}$, is plotted against the magnitude of $\vec{J}$. Values for one column of pixels are overlaid. The color of a set of points indicates its position on the bridge within the column of colored pixels in the inset, which is an image of the magnitude of J at maximum applied current. The values for one pixel are highlighted in black and the pixel location is marked in the inset.

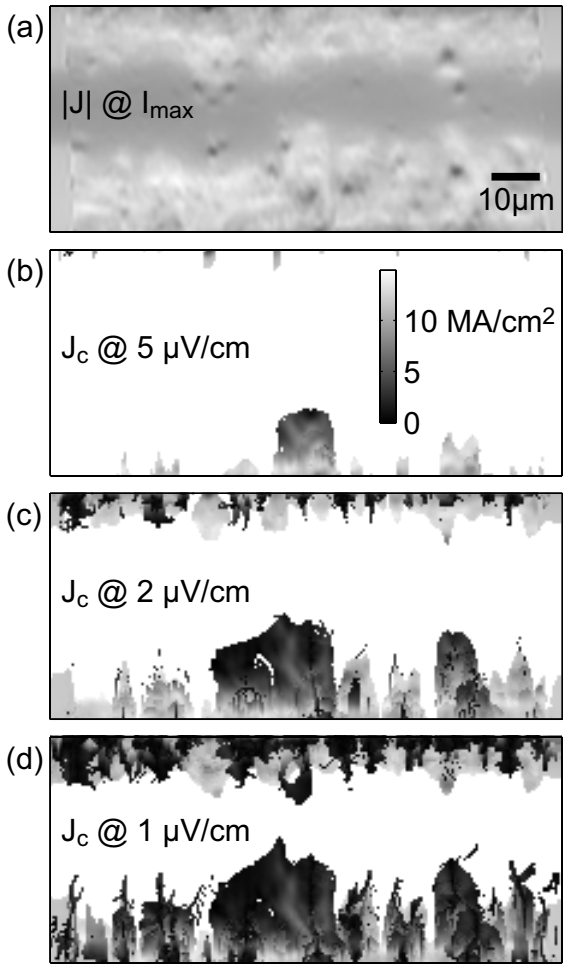

Figure 7.8: (a) The magnitude of J at maximum applied current compared to J_c extracted from E–J curves for various electric field criteria E_c, shown in (b)–(d). All are on the same color scale, shown in (b). Pixels that did not reach E_c are white. Though (b)–(d) show more scatter, areas of low J_c generally match those of low J in (a).

These deviations are mapped out in Figure 7.8 for various electric field criteria, E_c. The value of each pixel is the lowest J for which E_c is exceeded. If E_c is not exceeded, the pixel is plotted as white. If I use Figure 7.8(a), which shows J at maximum applied current, as an estimate of J_c, it seems that many of the curves hit E_c at erroneously low J. However, the spatial variation at least partially reflects genuine inhomogeneity of the material, because the points of low J_c along the edges of (b)–(d) correlate with low points in (a).

7.9 Reconstruction errors

Throughout this Chapter I have tried to point out physical assumptions and where they may break down. Even if my assumptions hold, however, the reconstruction procedure can introduce errors and amplify uncertainties. The magnitudes of these effects are difficult to predict analytically because of the many complex numerical transformations involved. Instead, I estimate the errors by executing the procedure on simulated data, for which I know exact solutions to compare to the reconstructed quantities. Figure 7.9 compares cross sections from the resultant exact and reconstructed images.

I generate the data with the same critical state model used for the background of the magnetic images, as described in Section 7.4 [Brandt and Indenbom, 1993; Zeldov et al., 1994]. The parameters are the same, with the applied current (-0.02 A) corresponding to Figure 7.3(f). I choose this frame because it includes regions of zero current, which present a worst case for reconstructing $\vec{E}_p$, as described below.

As the input to the reconstruction procedure, I calculate an image of the magnetic field in the measurement plane (z=1.2 μm). This is identical to the background of Figure 7.3(f), but extends over the entire image area. As in the background, I account for the sensor's tilt (3° about the x axis), which adds a small portion of $-B_y$ to the measured "B_z." I then add normally distributed noise within the measurement region (the subset of the image defined by the dashed green box in Figure 7.3(c)). The amplitude of the noise matches that observed in

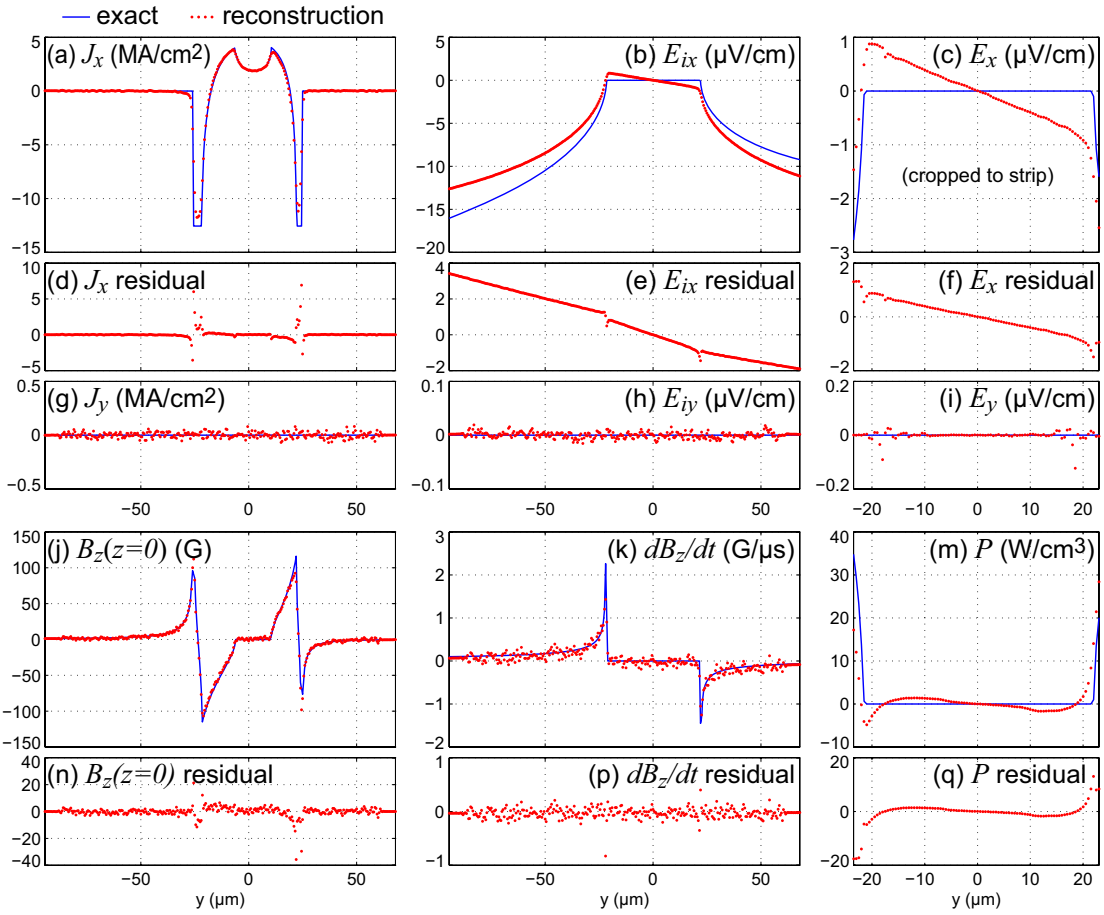

Figure 7.9: Errors introduced by the reconstruction procedure are analyzed by executing the procedure on model data. The exact quantities, known from the model, are plotted as blue lines. From them, the magnetic field in the measurement plane and its time derivative are calculated, noise is added, and the quantities are reconstructed. The red dots are y cross sections through the centers of the reconstructed images. The residuals are the reconstructed values minus the exact values. The only variation as a function of x comes from the noise, so the exact values of the y components are zero.

the real data outside the strip.

Using the reconstruction procedure, I obtain J_x, J_y, and $B_z(z = 0)$, shown in the first column of Figure 7.9. The reconstructed J_x smooths the sharp corners of the true J_x. It also displays 0.03 MA/cm^2 rms of noise, as does the reconstructed J_y. The only variation as a function of x comes from the noise added to B; the exact values of all y components (and E_{px}) are zero.

To reconstruct $\vec{E}$, I similarly calculate B for applied currents corresponding to 12.5 μs before and after Figure 7.3(f). From each B image I reconstruct $B_z(z = 0)$, and subtract to approximate $dB_z(z = 0)/dt$, shown in Figure 7.9(k). I then follow the reconstruction procedure for $\vec{E}_i$ (as in Section 7.6.1) and $\vec{E}_p$ (Section 7.6.3).

I see in Figure 7.9(e) that an erroneous negative slope is present in the residual of the reconstructed E_{ix}. This error can be traced to the small portion of $-B_y$ in B, which is not accounted for by the reconstruction procedure. In principle, the procedure could be adapted to assume a specified linear combination of B_y and B_z, though relations such as Equation 7.6 would become more complicated. One could also calculate an approximate B_y from the reconstructed J_x, subtract it from the measured B, then iterate, reconstructing a more accurate J_x and B_z each iteration. This procedure has been successfully applied to removing in-plane field components from magneto-optic images [Laviano et al., 2003]. Both procedures require precise knowledge of the sensor tilt.

Although small compared to the error in E_{ix}, other errors are worth noting. For one, I compare the y components of the inductive electric field and total electric field (Figure 7.9(h) versus (i)). The addition of E_{py} suppresses E_y (from about $6 \cdot 10^{-3}$ to $2 \cdot 10^{-3}$ μV/cm) everywhere except near $y = \pm 18$ μm, where E_y fluctuates with x by 0.1 μV/cm rms over the image. At these locations, J is approximately zero, making the direction of $\vec{J}$ completely uncertain, which renders Equations 7.17–7.21 inaccurate. Furthermore, such errors may scale up with the larger E_p present in the real data. Thus I must admit $\sim 100\%$ uncertainty in E_p near regions in which J drops below its noise level, 0.03 MA/cm^2. More generally, I point out that this error analysis is performed for a homogeneous model, which may not account for some features of real, inhomogeneous systems.

7.9.1 Alternate reconstruction of E from E_i

Where there are large uncertainties in $\vec{E}_p$, one can use an alternative route to reconstructing $\vec{E}$ that bypasses $\vec{E}_p$. This method starts with $\vec{\nabla} \times \vec{E}$, to which $\vec{E}_p$ (which is curl free by definition) does not contribute. As in Section 7.6.3, I assume $\vec{E}$ is parallel to $\vec{J}$, in which case I can write

$$\vec{E} = \rho(x, y, J)\vec{J} \tag{7.22}$$

and describe $\vec{E}$ via the scalar ρ (the local resistivity). Swapping sides and taking the curl, I have

$$(\vec{\nabla}\rho) \times \vec{J} + \rho(\vec{\nabla} \times \vec{J}) = \vec{\nabla} \times \vec{E} \tag{7.23}$$

Taking the z component and applying Faraday's law (Equation 7.8) to the right-hand side,

$$(\partial_x \rho)J_y - (\partial_y \rho)J_x + \rho(\partial_x J_y - \partial_y Jx) = -\partial_t B_z \tag{7.24}$$

To proceed, I assume that the spatial dependence of ρ arises solely from its dependence on J, i.e. that the E–J relation is constant over the single-pixel scale at which I solve this equation. Then,

$$\frac{d\rho}{dJ}\left[(\partial_x J)J_y - (\partial_y J)J_x\right] + \rho(\partial_x J_y - \partial_y Jx) = -\partial_t B_z \tag{7.25}$$

which I can write in a standard form

$$\frac{d\rho}{dJ} + \rho p(J) = q(J) \tag{7.26}$$

where

$$p(J) \equiv \frac{\partial_x J_y - \partial_y Jx}{(\partial_x J)J_y - (\partial_y J)J_x} \text{ and } q(J) \equiv \frac{-\partial_t B_z}{(\partial_x J)J_y - (\partial_y J)J_x} \tag{7.27}$$

are known. The solution to this differential equation is [Rainville and Bedient, 1969]

$$\rho(J) = \frac{\int_0^J u(J)q(J)dJ}{u(J)} \tag{7.28}$$

where $u \equiv \exp\left(\int_0^J p(J)dJ\right)$. I use the boundary condition $\rho(0) = 0$.

So the ingredients are the reconstructed $\partial_t B_z(z = 0)$ and $\vec{J}$, along with its spatial derivatives. These quantities are arranged by time; I re-sort them by J. Then the integrals with respect to J are calculated by the trapezoid method. Applying Equation 7.28 at each pixel, I obtain $\rho(J)$ and therefore $\vec{E}(J)$ at each point. I could then reconstruct $\vec{E}_p = \vec{E} - \vec{E}_i$ if desired.

In practice, my results are dominated by noise. In my images, the spatial derivatives of J are of order 10^{-3} MA/cm^3 while their uncertainties (based on the 0.03 MA/cm^2 uncertainty in J) are several orders of magnitude larger. This method may be effective, however, for other samples or measurement techniques.

7.10 Conclusion

I have shown that time-resolved magnetic imaging of a superconducting thin film yields a complete characterization of its electromagnetic properties, including distributions of current flow, electric field, power, and local E–J relations. I also point out the physical assumptions and requirements behind the mathematical transformations. The technique is compatible with various methods of magnetic imaging. It requires time resolution commensurate with the sample conditions being studied, but this capability is not limited to scanning Hall probe microscopes. Magneto-optics can use high-speed frame grabbing or a phase-locked short pulse technique to acquire similar data sets (albeit in a different pixel sequence) [Lucarelli et al., 2006]. Alternatively, the average response can be acquired from each pixel in succession, as is done here, at the expense of longer total acquisition time.

An applied field, $B_z(t)$, can be substituted for my applied current, and its time dependence need not be sinusoidal. For example, the analysis is applicable to the transient response following a change in applied current or field, as in Jooss

and Born [2006]. However, by demonstrating the technique on a superconducting strip carrying an applied current at 400 Hz, a realistic operating frequency for power applications [Kalsi, 2004], I wish to point out that an important use of this work is the characterization of material inhomogeneity and its effect on ac losses. Such imaging may also provide an efficient method for measuring the effects of complex sample geometries [Goldacker et al., 2006].

As mentioned in Section 7.8, E–J curves give insight into the flux pinning mechanism [Gurevich, 1990; Yeshurun et al., 1996; Blatter et al., 1994; Beasley et al., 1969; Anderson and Kim, 1964]. By resolving the variation in E versus J with position and time, this analysis may allow one to dissect the behavior of a heterogeneous sample, correlating pinning dynamics with materials properties. One may also examine correlations with quantities, such as magnetic field strength, that vary with space or time, fully accounting for the heterogeneous self-field experienced by different parts of the sample.

Chapter 8

Imaging coated conductors*

8.1 Introduction

I now apply my scanning Hall probe microscope and analysis techniques from Chapter 7 to the characterization of high-temperature superconducting wires. Such wires are being developed for high-current applications, including motors, generators, and power lines [Kalsi, 2004]. Present efforts center around the coated conductor architecture, in which a $YBa_2Cu_3O_{7-\delta}$ (YBCO) film is grown on a flexible metal tape [Larbalestier et al., 2001]. Here I image two tapes with different substrate architectures, ion beam assisted deposition (IBAD) [Groves et al., 2003; Kreiskott et al., 2004] and rolling assisted biaxially textured substrate (RABiTS) [Goyal et al., 1996], and find rather different behavior.

The two architectures are illustrated in Figure 8.1. In both structures, the metal tape is polycrystalline, consisting of a patchwork of grains separated by grain boundaries (GBs). However, GBs in YBCO are known to decrease J_c exponentially with the mismatch in orientation of the grains [Dimos et al., 1990; Hilgenkamp and Mannhart, 2002; Feldmann et al., 2000]. To ameliorate current blockage due to high-angle GBs in the YBCO, the two take different approaches. IBAD attempts to erase the grain orientation, or texture, of the tape, enforcing

*Parts of this Chapter are contained in Dinner et al. [2006b] and will be copyright ©2007 American Institute of Physics.

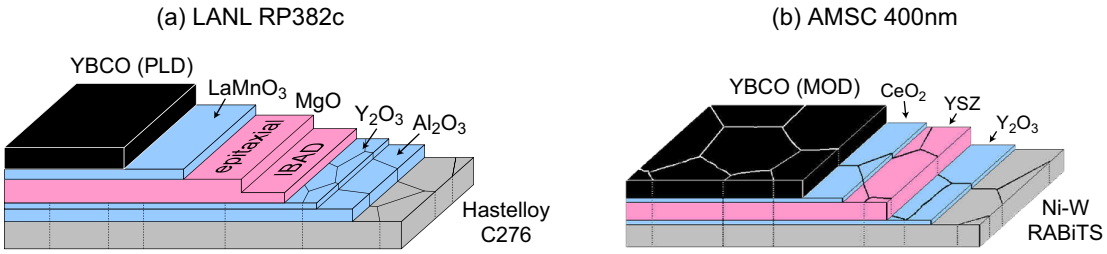

Figure 8.1: Structures of the two coated conductor samples studied. The first was grown at Los Alamos National Laboratory by Brady Gibbons and Vladimir Matias using pulsed laser deposition (PLD) to deposit YBCO on IBAD (ion beam assisted deposition) MgO. The second was grown by American Superconductor using metalorganic deposition (MOD) on rolling assisted biaxially textured substrate (RABiTS). RABiTS graphic by Matt Feldmann.

MgO texture with the ion beam direction. RABiTS works to improve texture in the tape itself. Both achieve highly oriented YBCO, as described below, but yield different YBCO grain size, 0.1–1 μm in IBAD [Iijima et al., 2004] and 25 μm in RABiTS [Feldmann et al., 2006], which plays out in my magnetic images.

8.2 PLD on IBAD MgO

The coated conductor depicted by Figure 8.1(a) was grown at Los Alamos National Laboratory (LANL) by Brady Gibbons and Vladimir Matias. They used pulsed laser deposition (PLD) to deposit 1.2 μm of YBCO on IBAD MgO. The in-plane spread in grain orientation is 2.3° FWHM, as determined by x-ray diffraction (ϕ scan). The film's T_c is 89 K, and it is imaged at 40 K.

The 1 cm wide tape was cut with shears into a 1 cm long section. I deposited contact pads* as seen in Figure 8.2(a) along the cut sides. These pads are designed to allow the sample to be patterned into several bridges, but for this experiment, I left the film unpatterned, using the lowest two pads to apply a current from

*I deposited the contact pads in the Moore 087 electron-beam evaporator/RIBE (reactive ion beam etcher) through a shadow mask. I cleaned the YBCO surface by etching (argon ion milling) it for 30 seconds, then deposited 10 nm of titanium followed by 200 nm of gold.

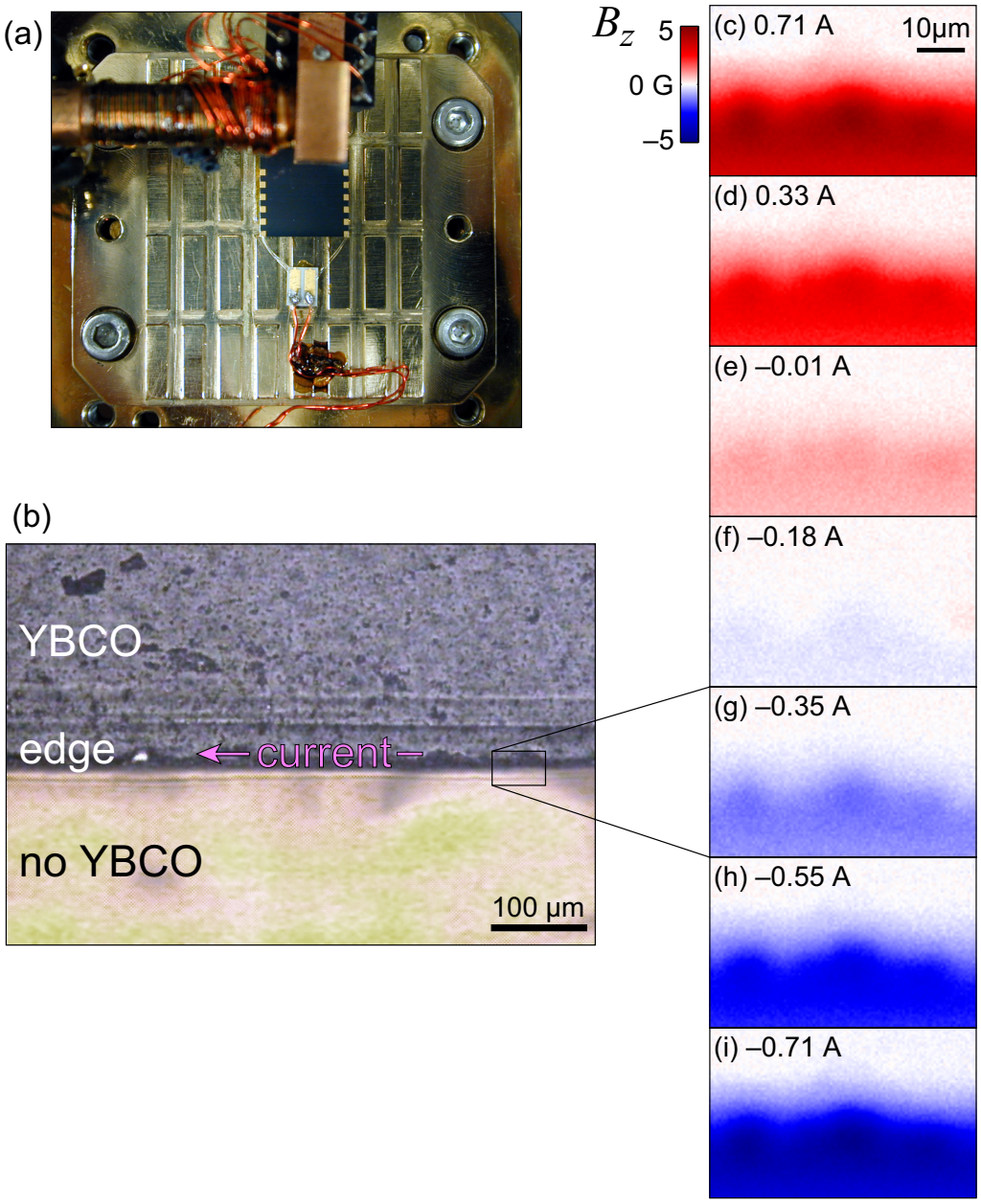

Figure 8.2: (a)An unpatterned piece of coated conductor grown by PLD on IBAD MgO is attached to the sample stage of the scanning Hall probe microscope. (b) An optical micrograph of the sample's $-y$ edge (bottom edge, in (a)). Texture in the direction of rolling of the tape is evident, as well as variations along the edge. (c)–(i) Scanning Hall probe images of a section of the edge with an applied current of 0.5 Arms. The full set of images is shown in the movie `LANL.avi`.

right to left.

Applying 0.5 Arms at 402.7 Hz, I image flux penetration into the edge of the sample, using the time-resolved data acquisition method of Section 7.3. The only inhomogeneity in the images occurs on ∼20 μm length scales, plausibly arising from the irregular shape of the edge visible in the optical micrograph, Figure 8.2(b). I see no evidence of grain boundaries, but this is probably because the 0.1–1 μm grains are smeared out by my resolution of 1 μm.

8.3 MOD on RABiTS: meandering grain boundaries

In contrast to the LANL sample, my second coated conductor shows more dramatic inhomogeneity. Its 400 nm thick YBCO film is grown by American Superconductor Corp. using metalorganic deposition (MOD) on RABiTS, as illustrated in Figure 8.1(b). Figure 8.3(a) shows the sample geometry, defined by lines cut through the film with a Nd-YAG laser. The cuts direct the applied current to flow through a 200 μm wide by 450 μm long link. As depicted by the pink arrows near the upper right corner of the link, current flows along the link at the bottom edge of the laser cut (the top edge of the link), and shielding current flows in the isolated section of YBCO above the link, in response to the field generated by the link. These currents force flux into the film from the cuts, though the penetration is rather inhomogeneous.

I see this inhomogeneity first in Figure 8.3(b), a magneto-optic image* taken by Matt Feldmann at 60 K as the link carries 3.8 A of current. The boxed corner shows the downward penetration of several yellow fingers of flux. A scanning Hall probe image of this corner from the series in Figure 8.3(c)–(h) is overlaid

*In the magneto-optic technique, an indicator film is placed on the surface of the sample and imaged (through a window in the cryostat) with a polarization-sensitive optical microscope, configured so that the intensity in Figure 8.3(b) is approximately proportional to the square of B_z, i.e. black areas represent $B_z = 0$ [Feldmann, 2001; Koblischka and Wijngaarden, 1995b]. The change in sign of B_z from the top to the bottom edge of the link produces a slight change in color—yellow versus green.

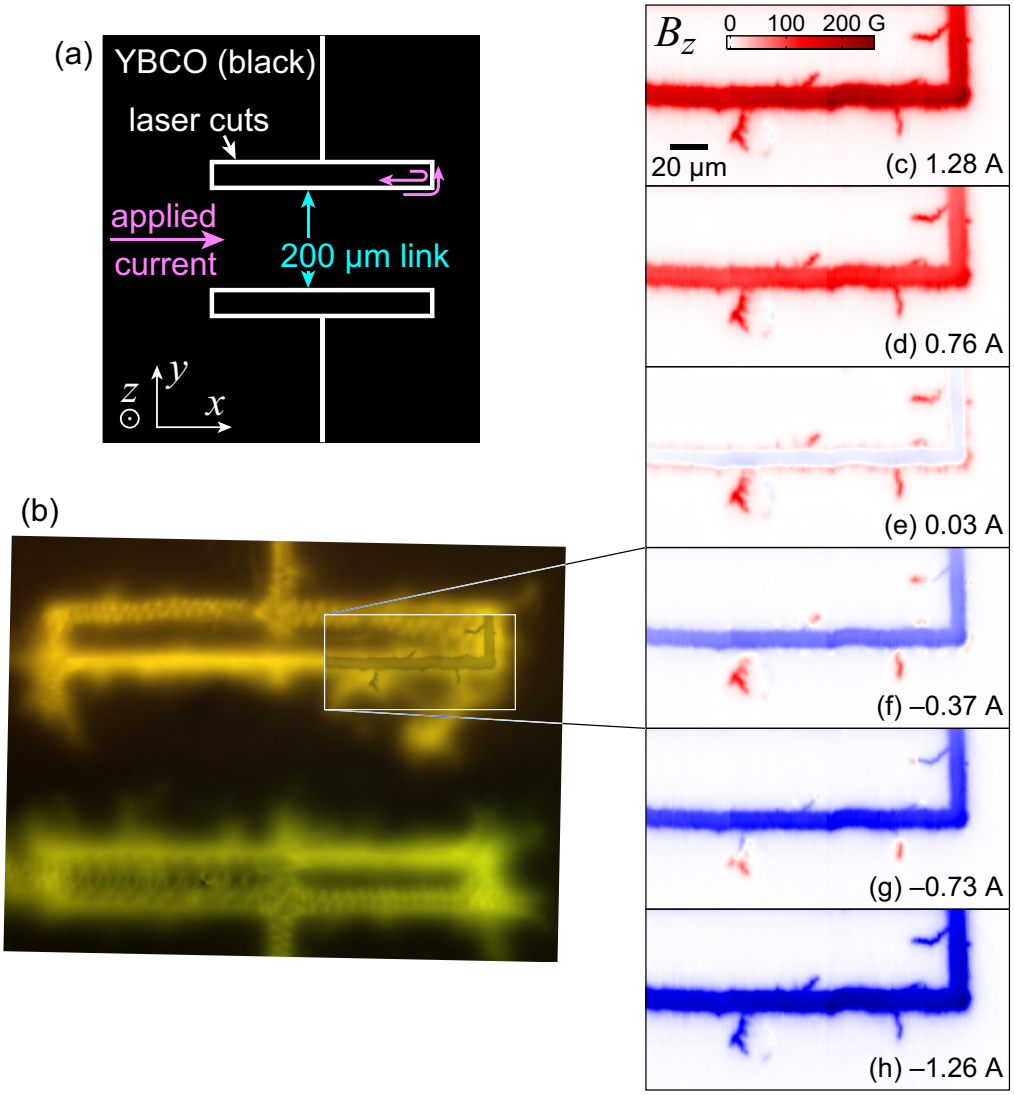

Figure 8.3: (a) Sketch of a coated conductor grown by MOD on RABiTS with a 200 μm wide by 450 μm long link defined via laser cuts through the film. In the upper right corner of the link, current flows as depicted by the pink arrows, along the link edges and also in the isolated rectangular section of YBCO above the link, in response to the field generated by the link. (b) A magneto-optic image by Matt Feldmann of the link at 60 K carrying 3.8 A of current. Flux penetrates inhomogeneously from the cut edges. (c)–(h) Scanning Hall probe images of the area indicated by the box and overlay in (b), resolving the flux penetration in greater detail. These images are taken at 40 K with 0.9 Arms of applied current. The full set of images is shown in the movie `AMSC.avi`.

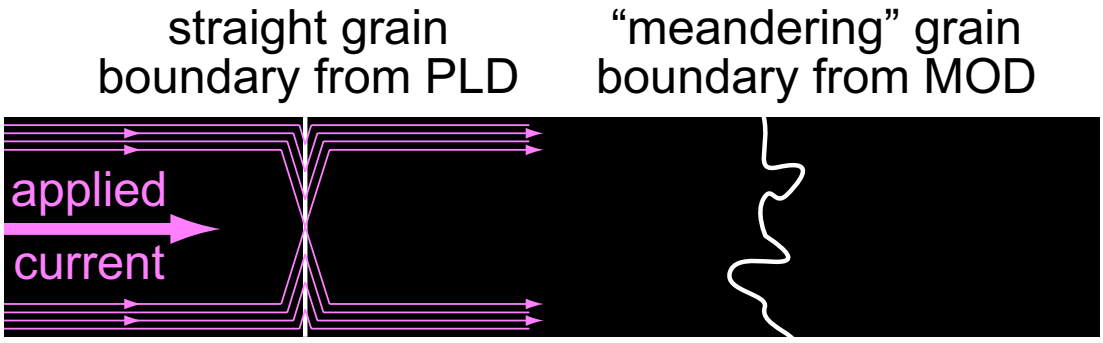

Figure 8.4: Compared to a straight grain boundary perpendicular to current flow, a meandering boundary is longer, potentially admitting more current at the same local current density.

on the magneto-optic image, resolving the structure of these fingers with higher resolution.

The scanning Hall probe images (c)–(h) are taken at 40 K with an applied current of 1.3 A, thus the flux does not penetrate as far as in the magneto-optic image. The penetration I do see is primarily along narrow, crack-like features. Combined magneto-optic and x-ray grain mapping studies of similar samples (grain mapping has not been done on this sample) have shown that such narrow features are GBs arising from the spread in grain orientations of about 6° [Feldmann et al., 2000, 2006].

My images reveal a further detail: The GBs are not straight. In previous work [Feldmann et al., 2006], films grown on RABiTS by MOD and PLD were found to have a similar *intragrain* J_c (4.5 versus 5.1 MA/cm^2 at 0 T, 77 K), but rather different *intergrain* J_c (0.9 versus 3.4 MA/cm^2), i.e. the MOD film's GBs were more transparent to current flow. Grain mapping of the MOD film's substrate compared to layers in the YBCO found two possible contributions to its enhanced intergrain J_c. First, the grain alignment improved from the substrate to the YBCO. Second, the YBCO GBs meander relative to the straight substrate GBs, as depicted in Figure 8.4. In contrast, PLD films replicate the substrate grains' orientations and straight GBs. Meandering increases the length (and area)

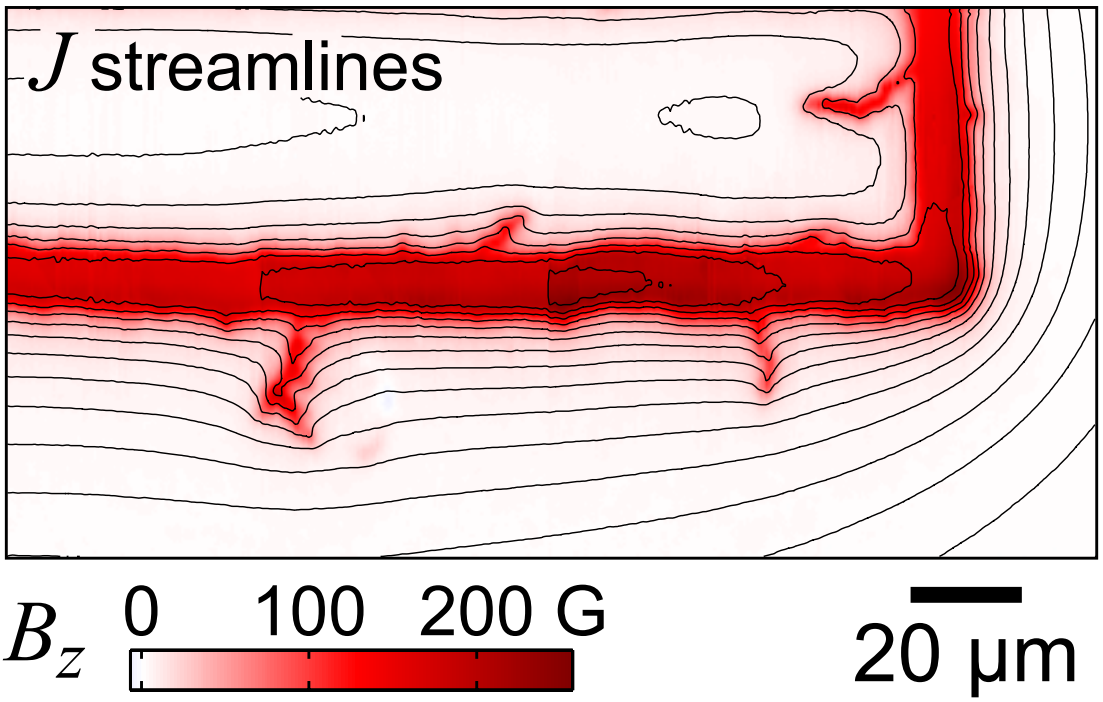

Figure 8.5: Streamlines of current, $\vec{J}$, reconstructed from Figure 8.3, frame (c). The current redirects to accommodate the meandering structure of several grain boundaries.

of the GB connecting two grains of a given width, and may thereby lead to a proportional increase in I_c.

My images show that the MOD film's meandering boundary geometry is reflected in its electromagnetic response. By reconstructing the current density, $\vec{J}$, from one of the scanning Hall probe images using the methods of Chapter 7,* I show in Figure 8.5 that $\vec{J}$ does change direction to accommodate the shape of the meandering GBs, at least down to the length scales of the instrument resolution of about 1 μm.

Thus in the MOD film on RABiTS, my images indicate that grain boundaries

*While it is unlikely to affect the qualitative conclusions I draw from the reconstructed $\vec{J}$, I note that in this 400 nm thick film, the current may not be highly two-dimensional, as in the thinner film of Chapter 7. This may affect the fidelity of the reconstruction, which assumes two-dimensionality, as discussed in Section 7.5.1.

indeed limit J_c. Furthermore, I find that these boundaries meander, and the current crossing them redirects accordingly. The connection between increased boundary length and I_c is explored further in Chapter 9.

Chapter 9

Tilted grain boundaries: model for in-plane meandering*

9.1 Introduction

Chapter 8 revealed in-plane meandering of the grain boundaries of an MOD film on RABiTS. Here I examine the consequences of such meandering for current flow, but in the more controlled geometry of a single, straight boundary placed at various in-plane angles across a link of a fixed width. As with a locally straight portion of a meandering grain boundary, tilting the boundary toward the direction of current flow between the grains presents a longer boundary. This is illustrated in Figure 9.1, along with streamlines of current flow calculated from the Bean model [Bean, 1964; Polyanskii et al., 1996].

The streamlines are calculated for the portion of the film that has been penetrated by vortices and reached the critical current density; they do not include the demagnetization currents that would flow in the sub-critical central regions of the film. These currents would cause an additional portion of the grain boundary to reach its critical current. The streamlines shown do, however, illustrate valid behavior for the edges of the film, and indicate how the current redirects to take

*Parts of this Chapter are contained in Dinner et al. [2006b] and will be copyright ©2007 American Institute of Physics.

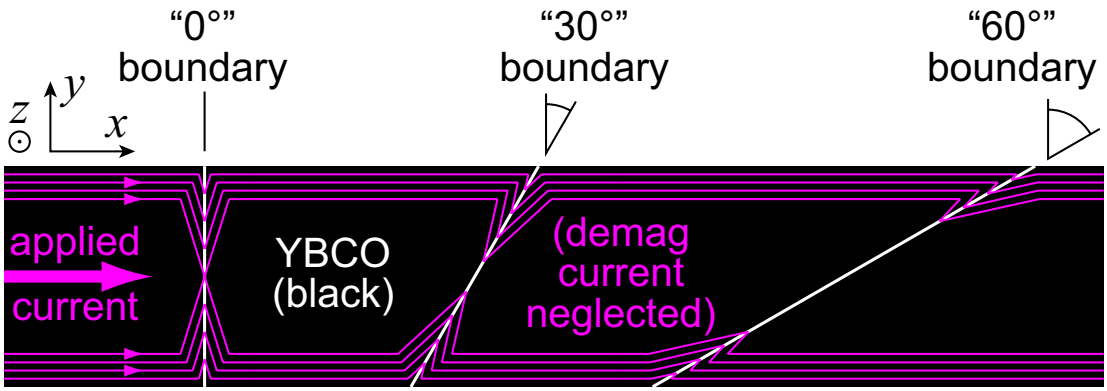

Figure 9.1: Three grain boundaries representative of those studied in this work cross a YBCO link. Streamlines calculated from the Bean model indicate the path taken by an applied current. Because the current redirects to cross perpendicular to each boundary, the critical current scales with the length of the boundary.

advantage of the additional length of the tilted grain boundaries.

The ratio of the grain boundary critical current density, J_b, to the intragrain J_c, is chosen to be 0.30, corresponding to the value measured for the 0° sample via transport as described in Section 9.3. The innermost streamlines shown fully penetrate the 0° boundary, but the tilted boundaries remain subcritical at this current level. Both I–V measurements and magnetic imaging confirm this picture, in which tilting increases the critical current of the boundary, I_b.

9.2 Samples: YBCO links on bicrystals

To isolate single grain boundaries at controlled tilts, a 180 nm thick YBCO film is grown epitaxially by pulsed laser deposition on a 5° miscut $SrTiO_3$ [001] bicrystal substrate with a straight boundary. Photolithographic patterning followed by argon ion milling removes parts of the film, leaving links that direct an applied current at 0°, 30°, and 60° relative to the boundary normal, as shown in Figure 9.2. The 30° and 60° links are patterned from the same film on different segments of the same grain boundary. The 0° link is another film with the same growth

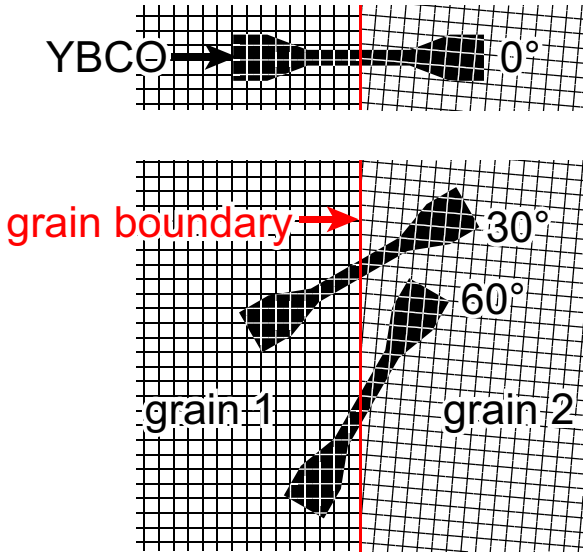

Figure 9.2: Three YBCO links (not to scale) are patterned at various angles relative to grain boundaries in a $SrTiO_3$ bicrystal substrate. The 30° and 60° links share one boundary.

parameters. Another section of the 0° link that does not cross the grain boundary is used in Chapter 7. The films' T_c (defined by the maximum in dR/dT) is 90 K.

9.3 Transport measurements

I first measure current-voltage characteristics of the links at 77 K in liquid nitrogen with a critical voltage criterion of 50 nV. The zero-field results are shown in Table 9.1. In my simple picture of I_c increasing in proportion to GB area, the fourth column should be constant. Instead, I find it increases with GB tilt, exceeding the expected proportionality. In fact, at 60° tilt, J_c is equal to the measured intragrain value, as if the GB were completely transparent to the current. This strong dependence of J_c on tilt angle motivates my more detailed study of these samples via magnetic imaging.

Noise characteristics of the Hall sensor force us to image at 40 K rather than 77 K, as described in the next Section. I therefore also measure current-voltage

sample	J_c (MA/cm^2) by strip area		... by GB area	
	77 K	40 K	77 K	40 K
0° GB	1.4	5.6	1.4	5.6
30° GB	1.8	4.9	1.6	4.3
60° GB	4.7	>11.8	2.4	>5.9
no GB	4.7	12.6		

Table 9.1: Zero-field transport measurements of critical current I_c across three grain boundaries (GBs) normalized (to obtain J_c) by the cross sectional area of the strip or the GB. The 77 K measurements are done in nitrogen while the 40 K measurements are in vacuum in the scanning Hall probe cryostat.

characteristics in the scanning Hall probe cryostat (at 40 K in vacuum) and include the results in Table 9.1.

The I–V curves are obtained via the same time-resolved technique as the magnetic response, explained in Section 7.3. After magnetic scanning, the sample current and voltage waveforms are recorded for 100 seconds. These waveforms are broken into cycles of applied current and averaged. The averaged waveforms are plotted in Figures 9.3(b), 9.4(b), and 9.5(b). I_c is then found by plotting the sample voltage against applied current, and determining where it rises above a 50 nV threshold.

I was not able to exceed the 50 nV criterion for the 60° GB, so I can only place a lower bound on J_c. I also note that at 40 K, the 30° J_c values, compared to the 0° and 60°, are unexpectedly low. These values held for lower amplitudes of ac applied current, so they likely do not arise from sample heating.

9.4 Magnetic imaging and current reconstruction

Scanning Hall probe images, presented in Figures 9.3–9.5, yield a more complete picture of how the grain boundaries break down with current. Each of the image series tracks changes in B_z as the sinusoidal applied current decreases from maximum to minimum. The series are acquired with the method introduced in

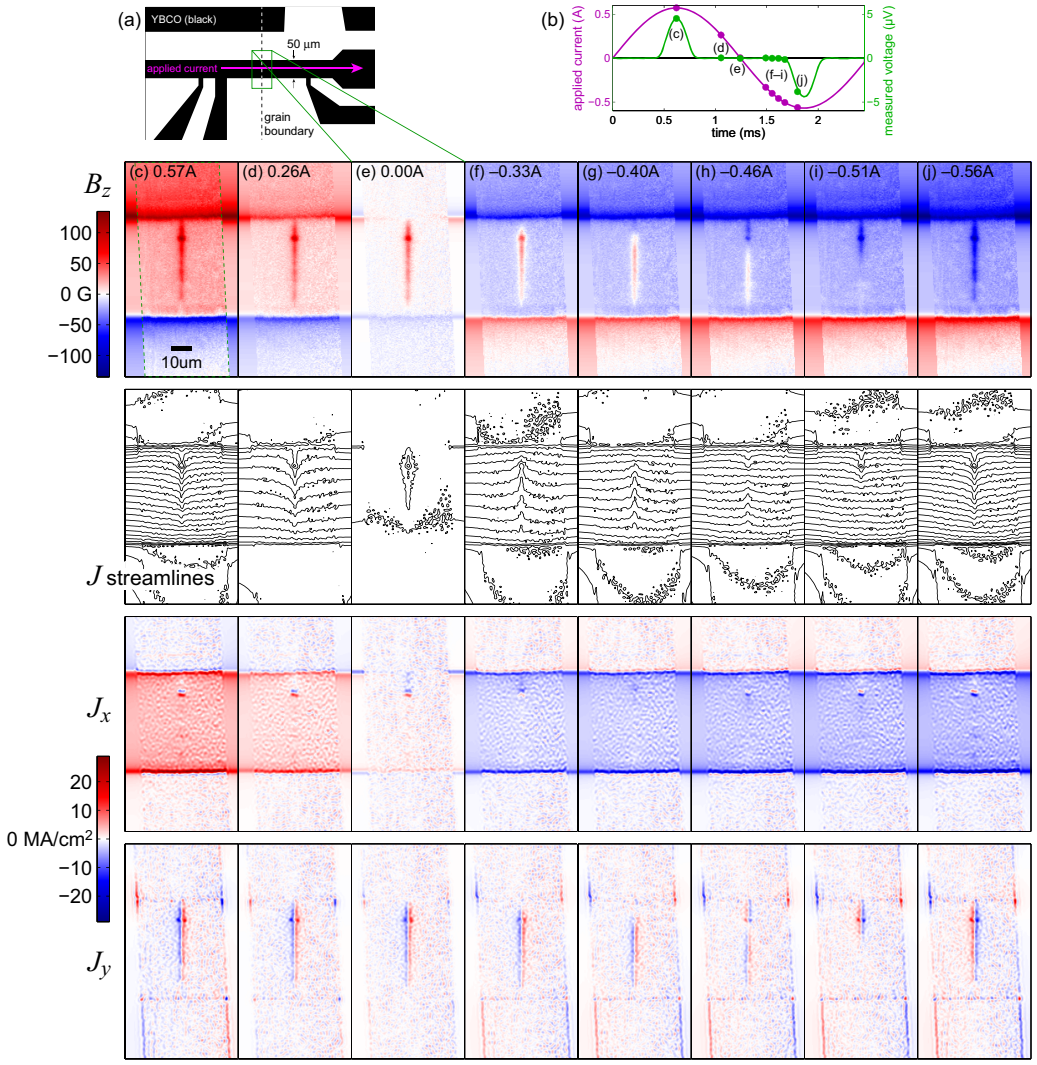

Figure 9.3: Scanning Hall probe imaging of transport through the 0° grain boundary at 40 K. (a) Illustration of the sample geometry. The approximate area of the magnetic images is outlined by the green box. The pink arrow indicates where the current is applied; the other leads are not used (floating). (b) Current during a 0.40 Arms, 400 Hz cycle. Select times are marked with labeled dots, and the corresponding magnetic images are shown in (c–h). The dashed green box in image (c) indicates the boundary of the data; the background outside of the data is filled by a fit to a critical state model. Below (c–j) are reconstructions from the magnetic data: streamlines and components of the current, J, flowing in the sample. 20 mA flows between neighboring streamlines. The complete set of frames is shown in the movie `BJ0.avi`.

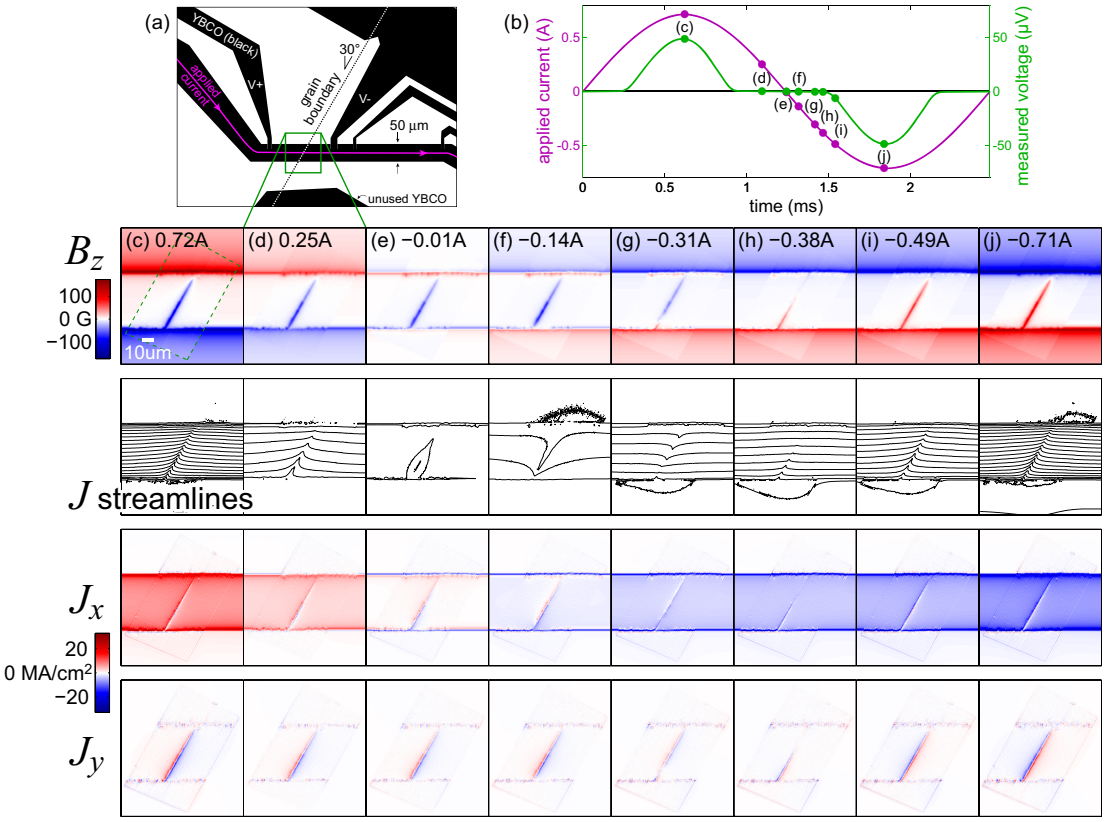

Figure 9.4: Scanning Hall probe imaging of transport through the 30° grain boundary, as in Figure 9.3. 40 mA flows between neighboring streamlines. The complete set of frames is shown in the movie `BJ30.avi`.

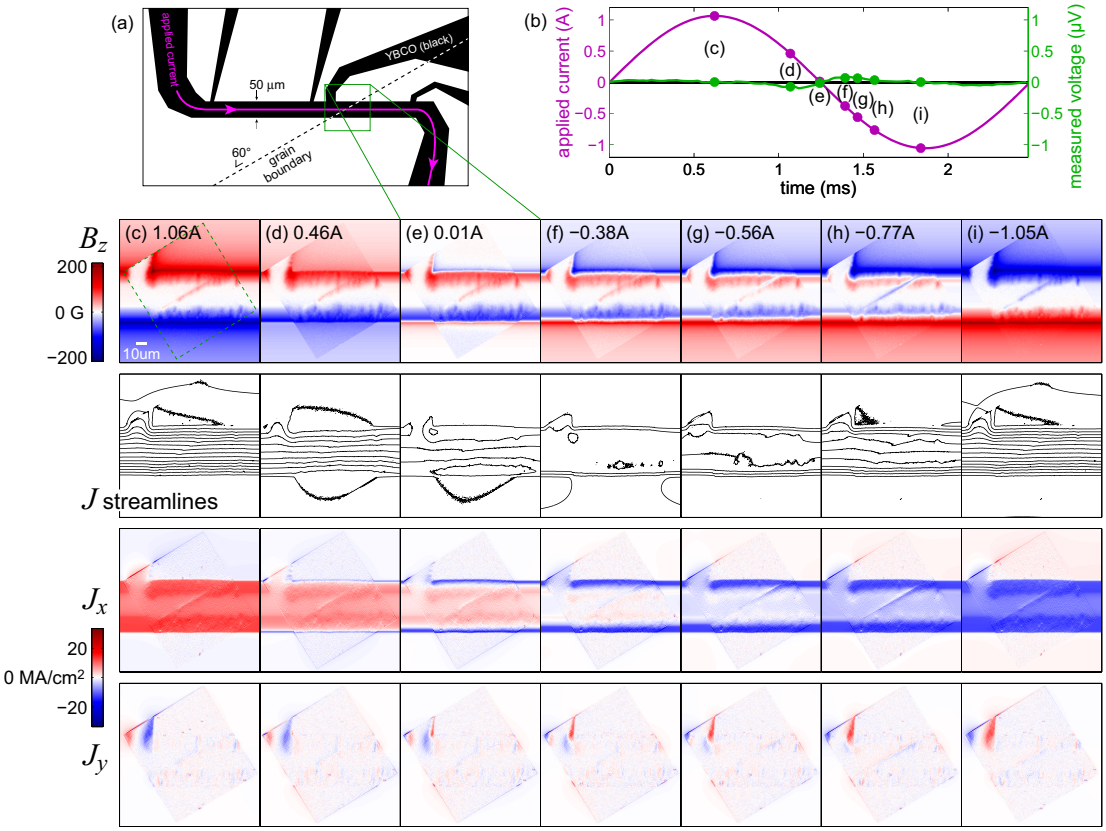

Figure 9.5: Scanning Hall probe imaging of transport through the 60° grain boundary, as in Figure 9.3. 40 mA flows between neighboring streamlines. The complete set of frames is shown in the movie `BJ60.avi`.

Section 7.3. From each B_z image, I reconstruct a map of $\vec{J}$ in the film, following Section 7.5.1.

For Hall probe imaging, the film substrates are varnished to a coldfinger in vacuum. The coldfinger is temperature controlled at 40 K while the Hall sensor is controlled at 54 K. Although it would be useful to image with the sample at 77 K for quantitative comparison with transport measurements, the Hall sensor under this condition equilibrates at 115 K and its noise increases dramatically, making the resultant images unsuitable for the detailed current reconstruction shown in Figures 9.3–9.5.

As discussed in Section 7.5.1, current reconstruction using the method of regularization [Feldmann, 2004] requires that I match opposite boundaries of the images for Fourier transforming. This is particularly problematic with these images, in which the links run at various angles to the image axes. I therefore follow the procedures of Section 7.4, rotating the images and filling in their backgrounds with a critical state calculation [Brandt and Indenbom, 1993], then mirroring the images top-to-bottom. After processing, I crop the frames back to the data boundaries, leaving some margin to illustrate the calculated background.

It was actually these images, not those of Chapter 7, for which I first developed this method. For the tilted grain boundary scans, matching the boundaries by windowing the edges to zero (instead of expanding each image with a calculated background) would discard most of the available data.

GB tilt	Hall coeff. (Ω/G)	J_c (MA/cm^2)	H (Oe) at peak J	sensor height above sample (μm)	sensor tilt
0°	0.006	16.7	6.8	1.5	20°
30°	0.030	20.0	0	1.0	5°
60°	0.029	13.3	-7.6	0.9	3°

Table 9.2: Parameters used in a critical state calculation of the magnetic field from a current-carrying strip that fills in the background of the B_z images. The tilt and applied J are known parameters, and the others are varied to fit each series of images.

The background field calculation has several free parameters, which are adjusted to fit each image series, as summarized in Table 9.2. These parameters are held constant within a series, though; the only input to the calculation that changes from frame to frame is the known applied current. For the 0° and 60° samples, the calculation includes a small, uniform applied field that varies in proportion to the applied current, which improves the fits. Its physical origin is likely stray field from the current in the sample leads.

The Hall coefficient for sensor 53, used for all three samples, was measured beforehand as described in Chapter 2. However, it evidently changed over the course of many scans, as the data cannot be fit with the precalibrated coefficient. I therefore allow the coefficient (an overall scaling factor in B) to vary as a free parameter, and apply the fitted coefficients to generate the magnetic images shown. It is at least reassuring that the 30° and 60° scans, taken in succession, show consistent values. The 0° scan was taken in a later cooldown. So my quantitative comparisons between samples depend, unfortunately, on the accuracy of the critical state fits to the data.

The grain boundaries' limiting effect on transport is immediately evident in the magnetic images, where flux penetrates along the boundaries, redirecting current with it. Flux enters asymmetrically, however: predominantly from the top of the 0° boundary, the bottom of the 30°, and the top of the 60°. I emphasize that these images represent the magnetic response of the films averaged over many cycles of applied current; the asymmetries do not vary from cycle to cycle. Thus I believe that this effect stems from real, though not necessarily large, asymmetries in the samples.

9.4.1 J_c from flux penetration

I now use two different methods to extract critical currents from the magnetic images and reconstructed current. The results, alongside the transport data of Section 9.3, are shown in Table 9.3.

In the first method, I identify the image, for each sample, at which the flux

GB tilt	J_b/J_c from transport	...from flux penetration	$J_\perp$ (MA/cm^2) from current reconstruction
0°	5.6	6.0	4.6
30°	4.3	4.0	3.5
60°	>5.9	3.8	4.5

Table 9.3: Several methods of measuring grain boundary critical current at 40 K. The middle three columns list J_b/J_c calculated from voltage measurements taken in the scanning Hall probe setup, and from the magnetic images by two methods. The critical current densities in the last column, not normalized by the intragrain J_c and boundary tilt, are expected to be constant in a simple model.

front moves fully across the boundary. The corresponding applied current is identified as I_c, and normalized by the grain boundary area to obtain J_c, listed in the third column of Table 9.3. The main disparity with the transport measurements is that the 60° sample shows full flux penetration over a significant portion of the applied current cycle, yet it did not produce a measurable voltage.

9.4.2 J_c from reconstructed current

As a second method, I extract $J_\perp$, the component of $\vec{J}$ perpendicular to the grain boundary direction. Throughout a region of critical current flow near the boundary, this component will be constant and equal to the actual current density crossing the boundary, as can be seen for the calculated streamlines in Figure 9.1. For each sample, I choose the frame in which the grain boundary is just subcritical, then define such a critical current region around the grain boundary near the edge of the strip from which the flux penetrates, where the magnitude of current is near its maximum. Each pixel within the region yields a value of $J_\perp$. Averages over the pixels are listed in the last column of Table 9.3. I then multiply this current density by the length of the boundary to estimate the total critical current of each link. This is divided by the measured intragrain critical current; the ratios are listed in the fourth column of Table 9.3.

$J_\perp$ is consistent across the samples, supporting the idea of critical current as proportional to grain boundary length. Even the 60° boundary, in contrast with

the transport results, adheres to this relation, its critical current still below that of the intragrain material. As with the J_c values calculated by the other two methods, the 30° boundary has a somewhat lower J_b, for which I again offer the sample heating hypothesis.

9.4.3 Angle of flow across boundary

As stated in the Introduction, my prediction that a grain boundary's critical current will scale with its length implies a constant critical current density perpendicular to the boundary. Coupling this assumption with the Bean requirement that the magnitude of the current on either side of the boundary equal a constant intragrain J_c in regions penetrated by vortices, I am led to draw streamlines that reflect over the boundary, as in Figure 9.1. However, streamlines that pass through the boundary without changing direction also satisfy these assumptions, given that $J_\perp$ does not exceed J_b. Note that only $J_\perp$, not J, determines the component of force on the vortex parallel to the boundary. The other component is countered by strong pinning that prevents vortices from moving off the boundary.

Thus when $I_b \geq I_c$, the current streamlines can flow straight without redirecting to cross perpendicular to the boundary. The magnetic images of the 60° boundary appear to be near this regime. Just as I measure $J_\perp$ in a region around the boundary, I can measure the component of $\vec{J}$ parallel to the boundary in order to calculate the average angle at which current flows in the region. This is calculated separately for the portion of the region on each side of the boundary, then the two sides are averaged with equal weight, to allow for differences in the numbers of pixels on the two sides. Expressed as tilt of the current from the boundary normals toward the applied current direction, these angles are 5°, 10°, and 64° for the 0°, 30°, and 60° boundaries. So the 30° boundary shows some deviation from the perpendicular current flow predicted by the Bean streamlines, and in the 60° boundary, flow is completely parallel to the link.

9.5 Reconciling transport and magnetic measurements

The magnetic images offer some insight into why transport yields higher J_c values, particularly for the 60° GB. First, I estimate the voltage accompanying $J_\perp$ from the rate at which the flux front moves along the GB and the density of vortices along the GB. This yields ∼10 nV, which is less than the transport J_c criterion of 50 nV, so I expect $J_\perp$, from current reconstruction, to be lower than J_c, from transport. Second, the density of vortices along the 60° GB is lowest—6 vortices/μm compared to 11 and 10 for the 0° and 30° GBs. Thus to achieve a fixed voltage criterion, the vortices must flow faster along the 60° GB, requiring a higher $J_\perp$.

9.6 Conclusion

With both transport and magnetic measurements, I have demonstrated that grain boundaries admit higher currents as they tilt toward the direction of current flow, in general agreement with a simple picture of constant current density multiplied by increasing length. My results suggest that the increased transparency of grain boundaries in MOD coated conductors on RABiTS, compared to their PLD counterparts, can arise from meandering boundary geometry.

Though transport indicates that I_c increases faster than expected with tilt to the point that the 60° boundary is completely transparent, magnetic imaging shows that this is not the case at lower voltage criteria—vortices do penetrate all of the boundaries before the grain critical currents are reached. At 60° tilt, however, disruption to the current is negligible, as confirmed by the angle of flow across the boundary being approximately parallel to the link.

Finer control of grain boundary geometry may continue to improve these conductors. By tilting grain boundaries even farther toward the current direction, one can imagine increasing J_c beyond that of the grains. Vortices would no longer slide along a GB (because the critical current of the boundary exceeds that of

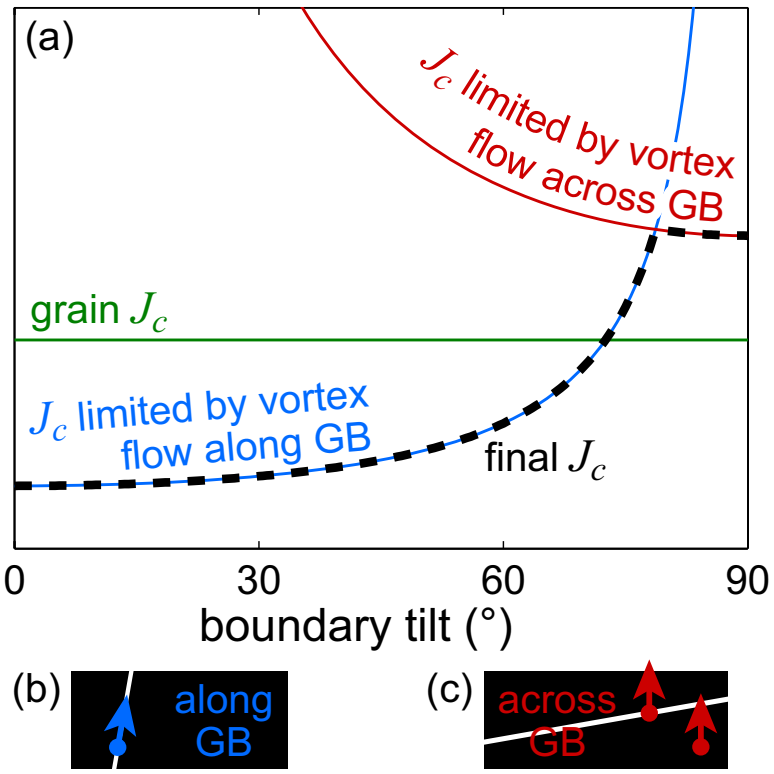

Figure 9.6: (a) Predicted limits on critical current density, J_c, as a function of grain boundary tilt. When the boundaries in a sample are close to perpendicular to the applied current (0° tilt), J_c is limited by vortices sliding along the boundaries, as depicted in (b). As the boundaries rotate toward 90°, vortices will no longer be forced along them, but rather across them, hopping on and off as they traverse the sample, depicted in (c). The J_c resulting from these two processes is marked as a dashed black line in (a).

the grains), and would in fact have to cross the boundary to produce steady-state dissipation. The crossover between different limitations on J_c—vortices moving along versus across a GB—is shown in Figure 9.6.

In the right hand regime, close to 90° tilt, the boundary acts as a planar pinning site, producing an enhanced local current density similar to the surface barrier in the YBCO ring of Chapter 3. This enhanced J_c would extend out to a distance of a penetration depth from the GB (or over the area of a vortex glass region formed along the boundary, in an interacting vortex picture). The grains would remain at their normal J_c. The region of enhanced current might be a small portion of the link width, and therefore difficult to detect in a transport measurement. By measuring locally, magnetic imaging followed by current reconstruction could provide better sensitivity to this enhanced J_c, as well as confirmation that it occurs along the grain boundary.

Chapter 10

Conclusion

This work demonstrates that scanning Hall probe microscopy offers quantitative characterization of current flow through superconducting films. My progress toward that conclusion was monotonic, but gradual. Chapter 3 hinted at the power of micron-scale characterization, deriving bulk and edge currents in a YBCO ring. It became clear, though, that detecting individual vortices requires reducing the separation of sample and sensor to below a few microns, and circumventing the sensor's low-frequency noise.

I met both of these requirements by building a scanning Hall probe microscope. Somewhat incredibly, macroscopic motors and micrometers proved capable of 50 nm step size or better, and 200 nm reproducibility, while maintaining centimeters of scan range. I did notice nonlinearities in the sensor movement on larger length scales (associated with the rotational periods of the gears), but these were correctable for small images via minor scaling.

Armed with a working microscope, I focused on extracting quantitative information from my images (often a challenge for imaging experiments). Two-dimensional reconstruction of current density from magnetic images has been addressed by others, but for reconstruction of electric fields, I had to chart new territory. An essential starting ingredient was time-resolved image acquisition, explained in Section 7.3.

Finally, in Chapters 8–9, I addressed a real-world interest: the development

of YBCO for power applications. Here, however, I only scratched the surface of a problem with many subtleties. The primary value of my work, then, lies in the potential of this microscope and accompanying techniques rather than the characterization of specific samples.

Many other physics problems are accessible to the instrument, but remain untouched. An example is current flow in semiconductor devices. The instrument has the ability to measure many such devices in a single cooldown, with micron-scale resolution. Reconstruction of current density could provide important insight into planar devices. The methods of Section 7.6 would not allow electric field reconstruction from magnetic imaging in a non-superconducting material, thus it may be worthwhile to add the capability of potentiometry to the Hall sensor using a conducting tip. Hopefully such variations will lead the instrument to new experiments, making this work just an introduction to its capabilities.

Bibliography

D. Abraimov, D. M. Feldmann, A. A. Polyanskii, A. Gurevich, G. Daniels, D. C. Larbalestier, A. P. Zhuravel, and A. V. Ustinov. Scanning laser imaging of dissipation in $YBa_2Cu_3O_{7-\delta}$-coated conductors. *Applied Physics Letters*, 85 (13):2568 – 70, 2004.

P. W. Anderson and Y. B. Kim. Hard superconductivity: Theory of the motion of Abrikosov flux lines. *Rev. Mod. Phys.*, 36(1):39–43, 1964.

C. P. Bean. Magnetization of high-field superconductors. *Rev. Mod. Phys.*, 36(1): 31 – 39, 1964.

C. P. Bean and J. D. Livingston. Surface barrier in type-II superconductors. *Phys. Rev. Lett.*, 12(1):14 – 16, 1964.

M. R. Beasley, R. Labusch, and W. W. Webb. Flux creep in type-II superconductors. *Phys. Rev.*, 181(2):682–700, 1969.

S. J. Bending. Local magnetic probes of superconductors. *Adv. Phys.*, 48:449, 1999.

G. Blatter, M. V. Feigel'man, V. B. Geshkenbein, A. I. Larkin, and V. M. Vinokur. Vortices in high-temperature superconductors. *Rev. Mod. Phys.*, 66(4):1125–1388, 1994.

E. H. Brandt. Square and rectangular thin superconductors in a transverse magnetic field. *Phys. Rev. Lett.*, 74(15):3025 – 8, 1995.

E. H. Brandt and J. R. Clem. Superconducting thin rings with finite penetration depth. *Physical Review B (Condensed Matter and Materials Physics)*, 69(18): 184509, 2004.

E. H. Brandt and M. Indenbom. Type-II-superconductor strip with current in a perpendicular magnetic field. *Phys. Rev. B*, 48(17):12893 – 906, 1993.

G. Carneiro and E. H. Brandt. Vortex lines in films: Fields and interactions. *Phys. Rev. B*, 61(9):6370 – 6, 2000.

A. M. Chang, H. D. Hallen, L. Harriott, H. F. Hess, H. L. Kao, J. Kwo, R. E. Miller, R. Wolfe, J. Vanderziel, and T. Y. Chang. Scanning Hall probe microscopy. *Appl. Phys. Lett.*, 61:1974, 1992a.

A. M. Chang, H. D. Hallen, H. F. Hess, H. L. Kao, J. Kwo, A. Sudbo, and T. Y. Chang. Scanning Hall-probe microscopy of a vortex and field fluctuations in lasub 1.85srsub 0.15cuosub 4 films. *Europhys. Lett.*, 20(7):645 – 50, 1992b.

G. A. Daniels, A. Gurevich, and D. C. Larbalestier. Improved strong magnetic field performance of low angle grain boundaries of calcium and oxygen overdoped $YBa_2Cu_3O_x$. *Appl. Phys. Lett.*, 77(20):3251 – 3, 2000.

D. Dimos, P. Chaudhari, and J. Mannhart. Superconducting transport properties of grain boundaries in $YBa_2Cu_3O_7$ bicrystals. *Phys. Rev. B*, 41(7):4038–4049, 1990.

R. B. Dinner, M. R. Beasley, and K. A. Moler. Cryogenic scanning Hall-probe microscope with centimeter scan range and submicron resolution. *Rev. Sci. Instrum.*, 76(10):103702 – 1, 2005.

R. B. Dinner, K. A. Moler, D. M. Feldmann, and M. R. Beasley. Imaging ac losses in superconducting films via scanning Hall probe microscopy. 2006a.

R. B. Dinner, K. A. Moler, D. M. Feldmann, and M. R. Beasley. Enhanced current flow through meandering grain boundaries in $yba_2cu_3o_{7-\delta}$ films. 2006b.

S. Djordjevic, E. Farber, G. Deutscher, N. Bontemps, O. Durand, and J.P. Contour. Low temperature dependence of the penetration depth in YBCO thin films revisited by mm wave transmission and surface impedance measurements. *Eur. Phys. J. B*, 25:407, 2002.

D. M. Feldmann. *Current flow in $YBa_2Cu_3O_{7-x}$ Deformation Textured Coated Conductors*. PhD thesis, University of Wisconsin–Madison, 2001.

D. M. Feldmann. Resolution of two-dimensional currents in superconductors from a two-dimensional magnetic field measurement by the method of regularization. *Phys. Rev. B*, 69:144515, 2004.

D. M. Feldmann, J. L. Reeves, A. A. Polyanskii, G. Kozlowski, R. R. Biggers, R. M. Nekkanti, I. Maartense, M. Tomsic, P. Barnes, C. E. Oberly, T. L. Peterson, S. E. Babcock, and D. C. Larbalestier. Influence of nickel substrate grain structure on $YBa_2Cu_3O_{7-x}$ supercurrent connectivity in deformation-textured coated conductors. *Appl. Phys. Lett.*, 77(18):2906 – 8, 2000.

D. M. Feldmann, T. G. Holesinger, C. Cantoni, R. Feenstra, N. A. Nelson, D. C. Larbalestier, D. T. Verebelyi, X. Li, and M. Rupich. Grain orientations and grain boundary networks of $YBa_2Cu_3O_{7-\delta}$ films deposited by metalorganic and pulsed laser deposition on biaxially textured Ni-W substrates. *J. Mater. Res.*, 21(4):923 – 34, 2006.

B. W. Gardner. *SQUID measurements of magnetic vortices in very underdoped Yttrium-Barium-Copper-Oxide*. PhD thesis, Stanford University, October 2004.

A. K. Geim, S. V. Dubonos, J. G. S. Lok, I. V. Grigorieva, J. C. Maan, L. T. Hansen, and P. E. Lindelof. Ballistic Hall micromagnetometry. *Appl. Phys. Lett.*, 71:2379, 1997.

D. Giller, Y. Abulafia, R. Prozorov, Y. Wolfus, A. Shaulov, and Y. Yeshurun. Local voltage-current characteristics in high-T_c superconductors. *Phys. Rev. B*, 57(22):R14080–R14083, 1998.

W. Goldacker, R. Nast, G. Kotzyba, S. I. Schlachter, A. Frank, B. Ringsdorf, C. Schmidt, and P. Komarek. High current DyBCO-ROEBEL assembled coated conductor (RACC). *J. Phys.: Conf. Ser.*, 43(1):901 – 4, 2006.

A. Goyal, D. P. Norton, J. D. Budai, M. Paranthaman, E. D. Specht, D. M. Kroeger, D. K. Christen, Q. He, B. Saffian, F. A. List, D. F. Lee, P. M. Martin, C. E. Klabunde, E. Hartfield, and V. K. Sikka. High critical current density superconducting tapes by epitaxial deposition of $YBa_2Cu_3O_x$ thick films on biaxially textured metals. *Appl. Phys. Lett.*, 69(12):1795–1797, 1996.

P. D. Grant, M. W. Denhoff, W. Xing, P. Brown, S. Govorkov, J. C. Irwin, B. Heinrich, H. Zhou, A. A. Fife, and A. R. Cragg. Determination of current and flux distribution in squares of thin-film high-temperature superconductors. *Physica C*, 229(3/4):289 – 300, 1994.

J. K. Gregory, S. J. Bending, and A. Sandhu. A scanning Hall probe microscope for large area magnetic imaging down to cryogenic temperatures. *Rev. Sci. Instrum.*, 73:3515, 2002.

R. Gross and D. Koelle. Low temperature scanning electron microscopy of superconducting thin films and Josephson junctions. *Rep. Prog. Phys.*, 57(7):651 – 741, 1994.

J. R. Groves, P. N. Arendt, S. R. Foltyn, Q. X. Jia, T. G. Holesinger, L. A. Emmert, R. F. DePaula, P. C. Dowden, and L. Stan. Improvement of IBAD MgO template layers on metallic substrates for YBCO HTS deposition. *IEEE Trans. Appl. Supercon.*, 13(2):2651 – 2654, 2003.

J. W. Guikema. *Scanning Hall probe microscopy of magnetic vortices in very underdoped yttrium-barium-copper-oxide*. PhD thesis, Stanford University, March 2004.

A. Gurevich. Distribution of pinning energies and the resistive transition in superconducting films. *Phys. Rev. B*, 42(7):4857–4860, 1990.

A. Gurevich. Current-limiting mechanisms in high-performance YBCO coated conductors: How much higher can J_c go? Talk at the Stanford-Wisconsin Coated Conductor Workshop, April 24 2006.

C. W. Hicks, L. Luan, K. A. Moler, E. Zeldov, and H. Shtrikman. Noise characteristics of 100nm-scale gaas/al$_x$ga$_{1-x}$as scanning hall probes. Submitted to Appl. Phys. Lett., 2006.

H. Hilgenkamp and J. Mannhart. Grain boundaries in high-T_c superconductors. *Rev. Mod. Phys.*, 74(2):485–549, 2002.

Yasuhiro Iijima, Kazuomi Kakimoto, Yasunori Sutoh, Shoji Ajimura, and Takashi Saitoh. Development of long Y-123 coated conductors by ion-beam-assisted-deposition and the pulsed-laser-deposition method. *Supercon. Sci. Technol.*, 17 (5):S264–S268, 2004.

M. Inoue, T. Kiss, S. Koyanagi, K. Imamura, M. Takeo, Y. Iijima, K. Kakimoto, T. Saitoh, J. Matsuda, Y. Tokunaga, T. Izumi, and Y. Shiohara. Imaging of trapped vortices in YBCO coated conductor by scanning SQUID microscope. *Physica C*, 426:1068 – 1072, 2005.

C. Jooss, J. Albrecht, H. Kuhn, S. Leonhardt, and H. Kronmuller. Magneto-optical studies of current distributions in high-T_c superconductors. *Rep. Prog. Phys.*, 65(5):651 – 788, 2002.

Ch. Jooss and V. Born. Determination of electric field distributions in superconductors via magneto-optical imaging and the Faraday law. *Phys. Rev. B*, 73 (9):94508 – 1, 2006.

S. Kalsi. Development status of rotating machines employing superconducting field windings. *Proc. IEEE*, 92:1688, 2004.

J. R. Kirtley, M. B. Ketchen, K. G. Stawiasz, J. Z. Sun, W. J. Gallagher, S. H. Blanton, and S. J. Wind. High-resolution scanning SQUID microscope. *Appl. Phys. Lett.*, 66:1138, 1995.

J. R. Kirtley, C. C. Tsuei, and K. A. Moler. Temperature dependence of the half-integer magnetic flux quantum. *Science*, 285:1373, 1999.

M. R. Koblischka and R. J. Wijngaarden. Magneto-optical investigations of superconductors. *Supercon. Sci. Technol.*, 8(4):199 – 213, 1995a.

M. R. Koblischka and R. L. Wijngaarden. Magneto-optical investigations of superconductors. *Supercond. Sci. Technol.*, 8:199, 1995b.

S. Kreiskott, P. N. Arendt, J. Y. Coulter, P. C. Dowden, S. R. Foltyn, B. J. Gibbons, V. Matias, and C. J. Sheehan. Reel-to-reel preparation of ion-beam assisted deposition (IBAD)-MgO based coated conductors. *Supercon. Sci. Technol.*, 17(5):S132 – 4, 2004.

M. N. Kunchur, D. K. Christen, C. E. Klabunde, and J. M. Phillips. Hall effect in $YBa_2Cu_3O_{7-\delta}$ in the limit of free flux flow. *Phys. Rev. Lett.*, 72(14):2259 – 62, 1994.

D. Larbalestier, A. Gurevich, D. M. Feldmann, and A. Polyanskii. High-T_c superconducting materials for electric power applications. *Nature*, 414(6861):368, 2001.

F. Laviano, D. Botta, A. Chiodoni, R. Gerbaldo, G. Ghigo, L. Gozzelino, S. Zannella, and E. Mezzetti. An improved method for quantitative magneto-optical analysis of superconductors. *Supercon. Sci. Technol.*, 16(1):71 – 9, 2003.

A. Lucarelli, G. Lupke, T. J. Haugan, G. A. Levin, and P. N. Barnes. Time-resolved magneto-optical imaging of $Y_1Ba_2Cu_3O_{7-\delta}$ thin films in high-frequency AC current regime. *Supercon. Sci. Technol.*, 19(6):667 – 70, 2006.

Y. Martin and H. Wickramasinghe. Magnetic imaging by "force microscopy" with 1000 Å resolution. *Appl. Phys. Lett.*, 50:1455, 1987.

W. T. Norris. Calculation of hysteresis losses in hard super-conductors carrying ac: isolated conductors and edges of thin sheets. *J. Phys. D*, 3(4):489 – 507, 1970.

S. Patnaik, D. M. Feldmann, A. A. Polyanskii, Y. Yuan, J. Jiang, X. Y. Cai, E. E. Hellstrom, D. C. Larbalestier, and Y. Huang. Local measurement of current density by magneto-optical current reconstruction in normally and overpressure processed Bi-2223 tapes. *IEEE T. Appl. Supercon.*, 13(2):2930 – 2933, 2003.

J. Pearl. Structure of superconductive vortices near a metal-air interface. *J. Appl. Phys.*, 37:4139, 1966.

G. K. Perkins, Y. V. Bugoslavsky, and A. D. Caplin. Scanning potentiometry and magnetic imaging of current transport in high-temperature superconductor coated conductors. *Supercon. Sci. Technol.*, 14(9):685 – 9, 2001.

A. A. Polyanskii, A. Gurevich, A. E. Pashitski, N. F. Heinig, R. D. Redwing, J. E. Nordman, and D. C. Larbalestier. Magneto-optical study of flux penetration and critical current densities in [001] tilt $YBa_2Cu_3O_{7-\delta}$ thin-film bicrystals. *Phys. Rev. B*, 53(13):8687 – 97, 1996.

C. P. Poole. *Handbook of superconductivity.* Academic Press, San Diego, CA, 2000.

E. D. Rainville and P. E. Bedient. *Elementary Differential Equations*, page 38. Macmillan, fourth edition, 1969.

B. J. Roth, N. G. Sepulveda, and J. P. Wikswo. Using a magnetometer to image a two-dimensional current distribution. *J. Appl. Phys.*, 65(1):361 – 72, 1989.

A. Sandhu, H. Masuda, H. Senoguchi, and K. Togawa. A novel variable temperature scanning nano-Hall probe microscope system for large area magnetic imaging incorporating piezoelectric actuators maintained at room temperature. *Nanotechnology*, 15:S410, 2004.

J. Siegel, J. Witt, N. Venturi, and S. Field. Compact large-range cryogenic scanner. *Rev. Sci. Instrum.*, 66:2520, 1995.

J. A. Stratton. *Electromagnetic theory*, page 214. McGraw-Hill, New York, NY, 1941.

M. Tinkham. *Introduction to Superconductivity*, page 179. McGraw-Hill, New York, NY, second edition, 1996a.

M. Tinkham. *Introduction to Superconductivity*, page 155. McGraw-Hill, New York, NY, second edition, 1996b.

A. Tonomura, T. Matsuda, H. Tanabe, N. Osakabe, J. Endo, A. Fukuhara, K. Shinagawa, and H. Fujiwara. Electron holography technique for investigating thin ferromagnetic films. *Phys. Rev. B*, 25:6799, 1982.

R. J. Wijngaarden, K. Heeck, H. J. W. Spoelder, R. Surdeanu, and R. Griessen. Fast determination of 2D current patterns in flat conductors from measurement of their magnetic field. *Physica C*, 295(3/4):177 – 85, 1998.

Y. Yeshurun, A. P. Malozemoff, and A. Shaulov. Magnetic relaxation in high-temperature superconductors. *Rev. Mod. Phys.*, 68(3):911–949, 1996.

E. Zeldov, J. R. Clem, M. McElfresh, and M. Darwin. Magnetization and transport currents in thin superconducting films. *Phys. Rev. B*, 49:9802, 1994.